Spring 2012

Dual active bridge converters in solid state transformers

Hengsi Qin

Department: Electrical and Computer Engineering

DUAL ACTIVE BRIDGE CONVERTERS IN SOLID STATE TRANSFORMERS

by

HENGSI QIN

A DISSERTATION

Presented to the Faculty of the Graduate School of the

MISSOURI UNIVERSITY OF SCIENCE AND TECHNOLOGY

In Partial Fulfillment of the Requirements for the Degree

DOCTOR OF PHILOSOPHY

in

ELECTRICAL ENGINEERING

2012

Approved
Dr. Jonathan W. Kimball, Advisor
Dr. Mariesa L. Crow
Dr. Mehdi Ferdowsi
Dr. Badrul Chowdhury
Dr. Bruce M. McMillin

ABSTRACT

This dissertation presents a comprehensive study of Dual Active Bridge (DAB) converters for Solid State Transformers (SSTs).

The first contribution is to propose an ac-ac DAB converter as a single stage SST. The proposed converter topology consists of two active H-bridges and one high-frequency transformer. Output voltage can be regulated when input voltage changes by phase shift modulation. Power is transferred from the leading bridge to the lagging bridge. It analyzes the steady-state operation and the range of zero-voltage switching. It develops a switch commutation scheme for the ac-ac DAB converters. Simulation and experiment results of a scaled down prototype are provided to verify the theoretical analysis.

The second contribution is to develop a full-order continuous-time average model for dc-dc DAB converters. The transformer current in DAB converter is purely ac, making continuous-time modeling difficult. Instead, the proposed approach uses the dc terms and 1st order terms of transformer current and capacitor voltage as state variables. Singular perturbation analysis is performed to find the sufficient conditions to separate the dynamics of transformer current and capacitor voltage. Experimental results confirm that the proposed model predicts the small-signal frequency response more accurately.

The third contribution addresses the controller design of a dc-dc DAB converter when driving a single-phase dc-ac inverter. It studies the effect of 120 Hz current generated by the single-phase inverter. The limitation of PI-controller is investigated. Two methods are proposed to reduce the voltage ripple at the output voltage of DAB converter. The first method helps the feedback loop with feedforward from inverter, while the second one adds an additional resonance controller to the feedback loop. Theoretical analysis, simulation and experiment results are provided to verify the effectiveness of the proposed methods.

ACKNOWLEDGMENT

I would like to thank Dr. Jonathan W. Kimball, my adviser and the chairman of my doctoral committee. The present work would not have been complete without his help. His insights and advice were instrumental in the formation of this dissertation.

I would also like to thank the remainder of my doctoral committee. Dr. Mariesa L. Crow and Dr. Badrul Chowdhury provided useful power systems background and perspective for the present work. Dr. Mehdi Ferdowsi has provided insightful help on modeling of power converters. Dr. Bruce M. McMillin provided a useful outside perspective.

Most of my doctoral research was supported by the ERC Program of the National Science Foundation under Award Number EEC-08212121. I would also like to thank the faculties and colleagues at the FREEDM Center.

I thank my family for all of their support and encouragement. My mother has always been a source of help, support, and encouragement. My father, for a short 16 years, was my role model, mentor, and friend.

Finally, I would like to thank my wife, Jun, for her constant love and support.

TABLE OF CONTENTS

LIST OF ILLUSTRATIONS

LIST OF TABLES

1. INTRODUCTION

In order to reduce the dependence on non-renewable fossil fuel and the amount of greenhouse gas emission, the demand for higher penetration of renewable energy has been growing rapidly during the last two decades. The major sources of renewable energy include wind energy, photovoltaic energy, hydrogen fuel cell energy, tidal energy, and geothermal energy. Most of these energy resources are utilized in the form of electric energy. Because of the unpredictable, and distributed nature of most renewable energy resources, the higher penetration of renewable energy will bring some challenges to the existing electric power system.

The existing electric power distribution system needs to change in order to incorporate more renewable energy resources. The conventional power system includes large, centralized power generators (by burning gas, oil, or coal or by hydra-power), where power generation is usually predictable and schedulable. Electric power is provided to consumers by passive transformers, transmission lines, and substations. The flow of electric power is uni-directional, from generators to consumers. However, this situation is about to change. Firstly, renewable power sources are distributed and might be located near the end consumers (such as roof-mounted solar panels or a fuel cell station near a residential community). Furthermore, the direction of power flow is not always in one direction any more. Consumers are able to sell electric energy back to the grid. Secondly, renewable power sources are usually not as schedulable and predictable as centralized power generators are. Therefore, it is necessary and preferable to install electric energy storage at the distribution level. Energy storage devices can be in the forms of battery stations or the on-board batteries of plug-in hybrid vehicles.

The trends of power generation at the distribution level, bi-directional power flow, and energy storage are analogous to the transition from TV broadcasting to the computer network. In computer networks users are able to create, store, and exchange information. Similarly, the next generation of power grid is sometimes referred as the "Energy Internet" [1], which includes energy router, intelligent fault interrupting device, energy storage device, and the related control and communication equipment.

The Future Renewable Electric Energy Delivery and Management (FREEDM) System is a prototype of the next generation of power systems with high penetration of energy storage and generation at the distribution level. In the FREEDM system, with the rapid development of power electronic devices, it is becoming possible to apply high frequency pulse-width modulation (PWM) converters as solid state transformers (SSTs) at the distribution level [2, 3, 4, 5, 6, 7]. An SST is able to control power flow, which is the "energy router", one of the key enabling components, in the FREEDM system [1].

Subsection 1.1 provides an overview of the FREEDM system, SSTs, and Dual Active Bridge (DAB) converters, which are used in certain stages of some SST configurations. Subsection 1.2 presents a comprehensive literature review on the state-of-the-art on the topology, modeling, control, and applications of DAB converters. Finally, the contributions of this dissertation are summarized in Subection 1.3.

1.1. BACKGROUND

1.1.1. Smart Grid and the FREEDM System. The term "smart grid" is a relatively broad concept with a number of definitions [8]. Some define smart grid as "electric grid using digital technologies". This definition includes smart meters that enable two-way communications between the utility and consumers (bi-directional smart metering), and variable electricity prices based on the demands during a day. Another definition of smart grid includes self-healing capability of power grids, in which distributed sensors and automatic controllers help power grid recover from faults of transmission lines and substations. The FREEDM System presents a broader concept of smart grid, which includes deeper penetration of distributed renewable electric power generation and more interaction between utility and consumers [1].

The FREEDM System identifies three key technologies: plug-and-play interfaces at both 400 V dc and 120/240 V ac split phase, electric energy router, and a distributed communication and control protocol [1]. The interfaces at 400 V dc and 120/240 V ac allow the installation of distributed power generation, such as small wind-turbines or solar arrays, at the distribution level. Similarly, energy storage device can also be connected to these standardized buses. The energy router enables direct control to power flows. It allows bi-directional power flow and selling electric

energy back to utility. The energy router also provides more features to the distribution power system, such as power factor correction, fault current limiting, and sag/swell ride-through capability. All these characteristics will improve the power quality at the distribution level. A distributed communication and control protocol provides more functionalities beyond two-way communications between utility and consumers by smart meters. It serves as an upper level supervisor and controller for the distribution system, enabling management and optimal operation of power generation and distribution.

Currently there is no device available to realize all of the functions of an energy router discussed above. Conventional passive transformers have no control on power flows. Switched capacitor banks and Static Var Compensators (SVCs) provide no more than reactive power compensation. A Unified Power Quality Conditioner (UPQC) is able to provide power factor correction and harmonics compensation. However, none of these devices has all the functionalities of an energy router. The concept of a Solid state transformer (SST) is introduced to fill this void.

1.1.2. Solid State Transformers. SSTs are essentially high switching frequency power electronic converters that have the following functionalities:

- They provide galvanic isolation between the input and the output of the converter.
- They provide active control of power flow in both directions.
- They provide compensation to disturbances in the power grid, such as variations of input voltage, short-term sag or swell.
- They provide ports or interfaces to connect distributed power generators or energy storage devices.

The main role of SSTs in the FREEDM System is that they acts as buffers among power grid, loads, distributed energy sources, and energy storage devices. By decoupling the load from the source, the consumers would not see the disturbance at the grid side because the disturbance is compensated by the SSTs. This is the advantage of SSTs for consumers. At the same time, the power grid would not see the reactive power generated by loads, which is compensated by SSTs. Therefore, the

distribution system becomes more efficient and stable. This is the advantage of SSTs for the power grid. Additionally, SSTs are buffers for renewable power sources, which help reduce the impact of unpredictable and unschedulable fluctuations of renewable electric power sources on both power grids and loads. This the advantage of SSTs for renewable power generation.

There are a number of candidate circuit configurations for SSTs. Four of them are briefly described as follows, all of which are single-phase, 60 Hz, 7.2 kV/120 V distribution transformers.

1. SST1 is the cascaded connection of a 60 Hz passive transformer and a low-voltage back-to-back ac-dc-ac converter (Figure 1.1). Because only low voltage power converters are used, this SST configuration uses off-the-shelf switching devices that are widely available. Although the configuration of SST1 looks trivial, it does have the power flow controllability required for SSTs. Therefore, it is considered as an SST configuration. However, it lacks a high frequency transformer and the 60 Hz transformer can be bulky. This configuration sets a base line for the analysis and evaluation of other SST configurations.

2. SST2 consists of three converter stages. Its first rectifier stage uses input-series-output-parallel configuration because available silicon-based devices are unable to block the peak voltage at the 7.2 kV side. Each two-level rectifier converts one-third of the input voltage to a 4 kV dc bus (Figure 1.2) [1]. Three dc-dc Dual Active Bridge (DAB) converters, whose outputs are parallel-connected, provide galvanically isolated power conversion to a 400 V dc bus in the second stage. A single-phase low-voltage dc-ac inverter converts 400 V dc to utility ac voltage in the third stage. SST2 is the most complex configuration. However, it has the full features of an SST: compact high frequency transformer, power flow control, power factor correction, and a low voltage dc bus for energy storage devices.

3. SST3 is similar to SST2 at the DAB and inverter stages. The difference is at the rectifier stage (Figure 1.3). SST3 uses a flying-capacitor multilevel ac-dc converter to provide a 12 kV dc bus for three paralleled-connected dc-dc DAB converters [9].

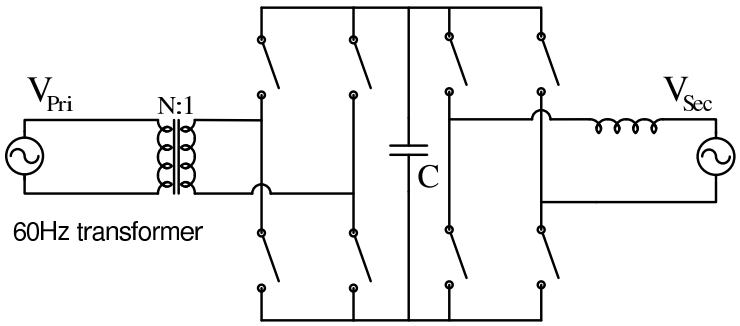

Figure 1.1. Configuration of SST1

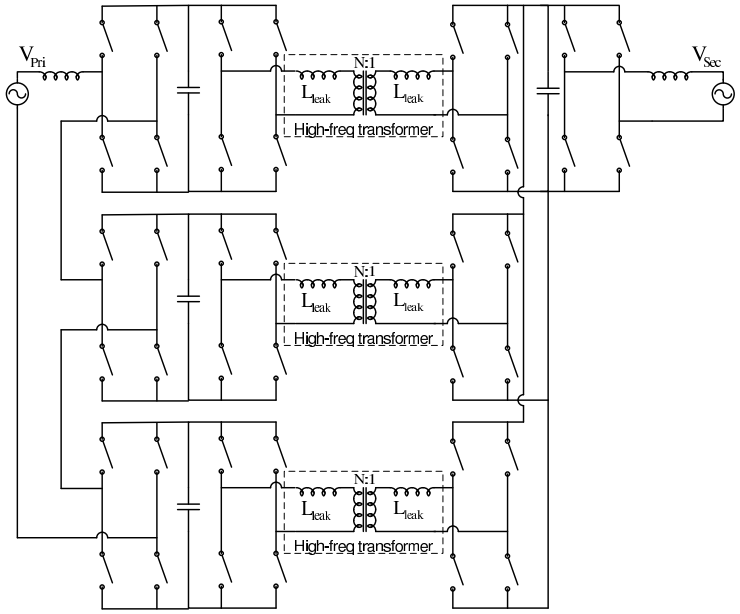

Figure 1.2. Configuration of SST2

4. SST4 uses an direct ac-ac version of DAB converter (Figure 1.4) [4]. It comprises three ac-ac DAB converters in an input-series-output-parallel connection. It is a single stage power converter, the simplest one of all four configurations. On the other hand, this simple topology controls only active power and lacks a dc port for renewable energy generation.

In the second, third, and fourth SST configuration, the galvanic isolation is achieved with a high-frequency transformer in a DAB converter.

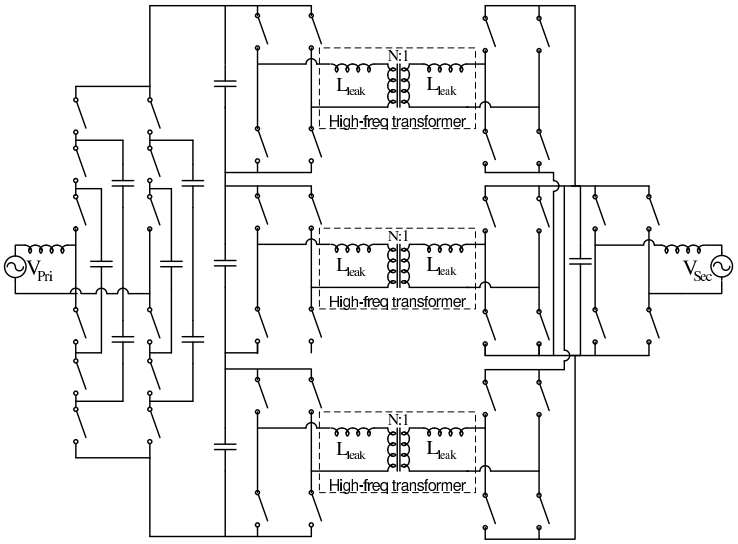

Figure 1.3. Configuration of SST3

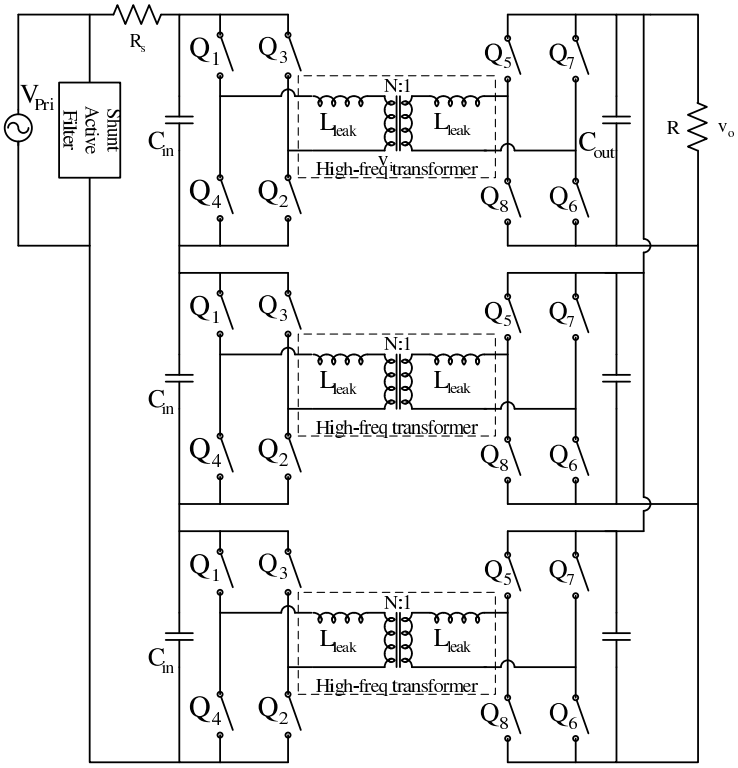

Figure 1.4. Configuration of SST4

1.1.3. Dual Active Bridge (DAB) Converters. A DAB converter is a high-power, high-power-density, and high-efficiency power converter with galvanic isolation [10, 11]. It consists of two H-bridges of active power switching devices and one high-frequency transformer. The high-frequency transformer provides both galvanic isolation and energy storage in its winding leakage inductance. The two H-bridges operate at fixed 50% duty ratio and the phase shift between the two bridges control the amount and direction of power flow. Based-on the configuration of switching devices, there are dc-dc DAB converters and ac-ac DAB converters. From Figure (1.2) to Figure (1.4), SST2, SST3, and SST4 all have some kind of DAB converters in certain stage of power conversion. In SST2 and SST3, dc-dc DAB converters are used, which connect the high voltage dc bus (12 kV) and the low voltage dc bus (400 V). In SST4, single stage ac-ac DAB converters are used as the main power conversion circuit.

1.2. LITERATURE REVIEW

Each power electronic converter design has four aspects: converter topology, model of the converter, controller for the converter, and other characteristics related to the application-specific background of the converter. The converter topology and operation must be analyzed in order to provide guidelines for designing a working converter. The power converter must be modeled accurately enough to capture the dynamics of the power converter and to provide insight for feedback and/or feedforward controller design. The controller must stabilize the control loop and achieve good steady-state and dynamic response. Overall, both the power converter and its controller must consider the application background and any application-specific attribute. This subsection summarizes prior works in these four aspects of power converters, with focuses on DAB converters.

1.2.1. Analysis and Applications of DAB Converters. Bidirectional isolated dc-dc DAB converters were initially proposed in [10] and [11] as candidates for high power density and high power dc-dc converters. The DAB topology is attractive because it has zero-voltage switching (ZVS), bidirectional power flow, and lower component stresses. A DAB converter consists of two H-bridges and one high-frequency transformer. One H-bridge converts the input voltage to an intermediate

high-frequency ac voltage, while another H-bridge converts the high-frequency square wave ac voltage back to the output voltage. A high-frequency transformer is used along with high-frequency switching devices because it reduces the weight and volume of passive magnetic devices. Beside galvanic isolation, the high-frequency transformer also has some leakage inductance in its primary and secondary windings, which together act as an energy storage component. The leakage inductance also helps achieve soft switching. During switching transients, transformer current resonates with the capacitors in parallel with switching devices, limiting the dv/dt and di/dt across the switches. Soft switching helps to reduce switching loss and achieve higher power efficiency.

Unlike other isolated dc-dc converters using asymmetrical topologies [12, 13, 14], DAB converters have a symmetrical circuit configuration, which enables bi-directional power flow needed for SSTs. The power flow of a DAB converter can be controlled by varying the phase shift between those two bridges. Such phase shift changes the voltage across the transformer leakage inductance. In this way the direction of power flow and the amount of power transferred are controlled. Power is transferred from the leading bridge to the lagging bridge.

DAB converters have become an interesting research topic during recent years. Some researchers focus on improvement of modulation methods. Dual phase-shift modulation has been proposed to reduce reactive power and loss for DAB converters [15]. Hybrid modulation methods have been developed to increase soft-switching range [16, 17]. Phase shift modulation plus duty-ratio control has been applied to DAB converters to achieve higher degree of control freedom [18, 19, 20, 21, 22]. Different modulation methods are evaluated and compared in [23]. New switching strategies are presented to reduce the switching loss and increase efficiency of DAB converters[15, 24]. More detailed circuit models are developed and analyzed to address some parasitic and nonlinear effects of DAB converters [25, 26]. Some published works focus on efficiency evaluation of DAB converters [27, 28]. Several circuit design optimizations are published in [29, 30, 31, 32, 33, 34, 35]

The DAB dc-dc converter has been used in battery-application systems, such as uuninterruptible power supplies (UPS), battery management systems, and auxiliary

power supplies for electric vehicles or hybrid electrical vehicles. For instance, an off-line UPS design based on the DAB topology is investigated in [36]. DAB converters are applied to manage bidirectional energy transfer between an energy storage system and a dc power system [37, 29, 38, 39]. DAB converters have been selected as a key component for automotive applications [40, 41, 42, 43, 44, 45]. DAB converters are also identified as the core circuit in the power electronic converter system between an ac power system and a renewable power source [46, 47, 48, 49]. The topology of DAB converters has been extended to allow multiple input/output ports [38, 50, 51, 52, 39]. The use of DAB converters in high power renewable power generation is reported in [34].

1.2.2. Modeling of Power Converters. Good controller design requires good plant models [53]. A high switching frequency power converter is essentially a nonlinear and time-varying system due to its switching nature. However, most control methodologies prefer a linear and time-invariant plant. Therefore, various modeling techniques have been proposed to approximate the nonlinearity and time-varying behaviors of a power converter and to provide a linear, time-invariant approximation of the power converter of interest.

One commonly used modeling technique is state-space averaging [54, 55, 56, 57, 58]. This conventional technique assumes that the switching frequency is much higher than the frequencies of interest and that the ripples in the state variables (such as inductor current and capacitor voltage) are small enough. It approximates the matrix exponentials in the solution of the power converter state equations using only linear and bi-linear terms, removes all quadratic terms, and results in a time-invariant model. This model can be further linearized around an steady-state operating point and then a linear, time-invariant small-signal model is derived. State-space averaging essentially takes the dc terms in the Fourier series of state variables. There is another averaging technique called generalized state space averaging, which keeps more terms in the Fourier series of state variables (normally the switching-frequency terms) [59, 60, 61, 62, 63, 64]. One advantage of generalized averaging is that it does not assume that the ripples of state variables are small. This technique discards less information and might be able to obtain more accurate models.

Besides generalized averaging, there is another averaging technique, called the Krylov-Bogoliubov-Mitropolsky (KBM) averaging method [65, 66]. Instead of using Fourier series of state variables, the KBM method approximates converter state variables by piecewise-polynomial equations. The effect of ripples caused by switching is included in this way. The KBM method is simpler than generalized averaging and does not require small ripples either. However, it might not be as useful as generalized averaging is when modeling pure ac state variables.

The three modeling techniques discussed above are all in the continuous-time domain. On the other hand, sampled-data models are in the discrete-time domain [67, 68, 69, 70, 57, 71]. A sampled-data model uses the fact that state variables of power converters have cycle-by-cycle repeatable trajectories in steady state. It is often derived by integrating the switched piecewise linear differential equations of state variables over one control cycle. The integration is in fact solving the state equations given a set of initial conditions, which involves multiplication and integration of exponentials. This process is often approximated by Taylor series expansions.

The controller design for DAB converters, like other power converters, also requires an average model of DAB converters. Currently there are two approaches to model a DAB converter in the literature: (1) a simplified reduced-order model that neglects the transformer current dynamic [72, 73, 74]; (2) a full-order discrete-time model that preserves the dynamic of transformer current [75, 76]. Discrete-time modeling is one approach to model those converters with large variation and resonant operations. However, a continuous-time model is usually preferred because it provides more physical insight and facilitates control design. The conventional state-space averaging technique for dc-dc converters requires negligible current ripple [58]. However, this condition is not satisfied in DAB converters because the transformer current of a DAB converter is purely ac. Instead, the generalized averaging technique, which uses more terms in the Fourier series of state variables, is able to capture the effect of pure ac current on converter dynamics [60, 62]. Therefore, generalized averaging technique is used in the present work to model DAB converters.

The rule-of-thumb for a dc-dc converter design is to separate the dynamics of current and voltage by selecting proper converter parameters. The simplified reduced-order model mentioned above assumes that the dynamics of the transformer current

are significantly faster than those of the output capacitor voltage. However, this assumption has not been verified analytically. Singular perturbation theory provides an analytical approach to separate the dynamics of different time-scales and provides the conditions of separation of the dynamics [77, 78]. The criteria of time-scale separation of state variables in dc-dc boost converters is reported in [78].

1.2.3. Control of Power Converters. A closed-loop controller is required when the output voltage of a power converter needs to be regulated and source/load disturbances need to be compensated. The idea of closed-loop control is essentially using the error between actual output and its reference to eliminate or minimize the error. The conventional controller design method for power converters is: derive the small-signal model around a steady-state operating point, find the control-to-output transfer function of the converter, specify the expected loop gain based on design specifications, and design the controller transfer function to match the desired loop gain [58]. A Proportional-Integral (PI) controller is a commonly used controller for power converters that require zero steady-state error when the reference is a dc signal. A lead compensator is another kind of controller for power converter that increases the phase-margin of the loop gain. One drawback of both PI controller and lead compensator is that they only achieve infinite gain at dc, making it difficult to obtain zero steady-state error if the reference or disturbance is a low-frequency ac signal.

A Proportional-Resonant (PR) controller is proposed to achieve infinite gain at a given frequency. It is analytically verified that PR controllers in a stationary frame are equivalent to PI controllers in a D-Q rotational frame [79, 80]. A PR controller is suitable for single phase ac applications because power in single phase systems is fluctuating at 120 Hz (second-order harmonic) [81, 82]. A PR controller is also used in three-phase inverters to achieve zero steady-state error and to compensate voltage harmonics and/or unbalanced contents caused by nonlinear loads, without using the time-consuming coordinate transformations [83, 84, 85, 81]. PR controllers have been applied to single-phase active rectifiers [86], grid-tie inverters [87], UPS [88], distributed power generation [89], and dynamic voltage restorer (DVR) [90]. A comprehensive review of PR controllers for single-phase dc-ac inverters is presented in [81]. The sensitivity of PR-controlled single-phase inverters is discussed in [91].

Impedance matching of a PR-controlled inverter is addressed in [92]; and the implementation of PR controllers in the form of digitial filters is discussed in [93] and [94].

The controllers described above are essentially designed for one operating point. Large phase margin and gain margin are necessary to ensure stable dynamic response when operating point deviates. However, the dynamic performance is not guaranteed when there is a large deviation of operating point caused by significant disturbance. Gain-scheduling control is one method of improvement [95, 96, 97, 98]. A set of controllers are selected using the above mentioned methods for different operating points. A supervisory controller switches between parameters according to feedback information, improving the performance over a wide operating range.

Adaptive control is a broader variant of gain-scheduling control. An adaptive controller adjusts its control parameters dynamically [99]. On-line parameter adjustment is able to provide better performance than the off-line adjustment in gain-scheduling control. Adaptive control is suitable for a system where the structure is known while the parameters of the system are varying or unknown. For instance, load resistance is treated as an unknown parameter in [100] and better output voltage regulation is achieved with an adaptive PI controller. Adaptive control has also been applied in active rectifiers [101], inverters [102], and fuel cell power generation systems [103].

Beside the control design methods based on (usually linear) small-signal average model, there are other nonlinear methods which use large signal models for controller design. One method is Lyapunov-based backstepping design. A positive-definite energy-like function, called a Lyapunov function, is defined based on the large signal converter average model. Control design is accomplished when the control input is able to make the time derivative of the Lyapunov function negative-definite [104, 105, 106, 107]. The Lyapunov-based control technique has been applied to dc-dc converters [108], active-front-end rectifiers [109], and voltage-source inverters [110]. Another nonlinear control method is sliding mode control (SMC) [111]. SMC is a variable structure control method. It defines a set of control structures. By switching between the control structures, the state variables are controlled to slide along a predefined expected trajectory. The switching nature of SMC makes it suitable as a controller for

power electronic converters. SMC has been applied in the control of dc-dc converters [112, 113], ac-ac converters [114], and doubly-fed inductor generators [115]. One advantage of nonlinear-based designs is that global stability and performance are studied and can be analytically verified. Another advantage of such control methods is the possibility of compensating for the non-minimum phase effect of boost-type converters [116].

Computational intelligence paradigms can also be applied for power converter controllers. Fuzzy logic is a computational intelligence paradigm. Advantages of fuzzy logic control include ease of implementation and resistance to disturbances [117]. Fuzzy logic has been used in adaptive energy management for electric vehicles [118], grid-tie solar inverters [119], and active front-end rectifiers [120].

There might be stability problems when two converters are cascaded connected [121, 122]. The load converter appears to be a negative impedance when it is tightly regulated by a fast control loop. Such negative impedance would make it difficult to develop a stabilizing controller [123]. This problem has been widely studied for dc-dc converters. The rule-of-thumb is that the output impedance of the driving converter should be less than the input impedance of the loading converter. Some studies based on state space models show that the problem of destabilizing negative impedance can be solved by filtering, or adding active damping [124, 125].

There are a number of literatures on the control of DAB converters. The state-of-the-art is using PI controllers with some simplified assumptions on converter models [126, 127, 128, 129]. As in multi-stage SSTs, a dc-dc DAB converter and a dc-ac inverter are cascaded. This issue is analyzed in [72, 130]. A relatively large dc-link capacitor is used to reduce the voltage ripple caused by second order harmonic. When several dc-dc DAB converters are connected in input-series-output-parallel configuration, instability problems might happen when bus voltage and output power are not balanced. Therefore, the works in [131] and [132] introduce voltage and balance control methods to solve such problems.

1.3. WORK SUMMARY

This dissertation presents the circuit analysis, modeling, design optimization, and controller design of DAB converters for SSTs.

The circuit analysis and operation principles of DAB converters are discussed in section 2. It studies steady-state operation and shows the principle of using phase-shift modulation to control the power flow of DAB converters. The proposed topology uses the leakage inductance in high frequency transformer, permitting soft-switching and regulation of output power by phase-shift modulation (PSM), which are absent in previously reported solutions [6]. This section also develops the conditions for achieving soft switching and analyzes the range of soft switching for different operation conditions. The analysis is applied to both dc-dc DAB converters and ac-ac DAB converters. Simulation of a dc-dc DAB converter and an ac-ac DAB converter are developed. A scaled-down prototype ac-ac DAB converter is built. Simulation and experimental results verify the theoretical analysis. Part of section 2 comes from the following papers:

- Solid State Transformer Architecture using AC-AC Dual Active Bridge Converter, submitted to IEEE Transactions on Industrial Electronics.
- AC-AC Dual Active Bridge Converter for Solid State Transformer, IEEE ECCE 2009
- A Comparative Efficiency Study of Silicon-based Solid State Transformers, IEEE ECCE, 2010
- Identifying techniques, topologies and features for maximizing the efficiency of a distribution grid with solid state power devices, North American Power Symposium 2010, NAPS 2010 (Second author)

Section 3 focuses on the development of a full-order continuous-time state-space average model using generalized state-space averaging technique. The pure ac transformer current is modeled by using the dc and first order terms in the Fourier series. The proposed full-order continuous-time average model uses the dc terms and first order terms of transformer current and capacitor voltage as state variables, resulting in a third-order model if capacitor equivalent series resistance (ESR) is not considered and a six-order model if ESR is considered. A control-to-output-voltage transfer function is derived for DAB converters. Experimental results of a 200 W dc-dc DAB

converter prototype confirm that the proposed model correctly predicts the small-signal dynamic response and more accurate prediction can be obtained if capacitor ESR is taken into account. By using singular perturbation theory, this section also develops the sufficient conditions for the separation of voltage and current dynamics, which is later confirmed by experimental results. Part of section 3 comes from the following paper:

- Generalized Average Modeling of DC-DC Dual Active Bridge Converters, accepted for publication in IEEE Transactions on Power Electronics.

Section 4 discusses the controller design for DAB converters when driving a single-phase dc-ac inverter. The conventional rule-of-thumb is to select an adequately large output capacitor bank to absorb the 120 Hz harmonic current. Because 120 Hz is relatively low, this might result in a large capacitor at the dc bus, increasing cost, weight, and volume. The large capacitor bank is also one major factor affecting the reliability of SSTs. This section addresses the effect of the 120 Hz harmonic current generated by single phase dc-ac inverters. By analyzing the loop gain of a DAB converter controlled by a PI controller, this section discusses the limitation of PI controllers. Two solutions, feedforward and a proportional-integral-resonant controller, are proposed to reduce the demand for large dc bus capacitance. In the first method, additional feedforward control is added to reduce output 120 Hz voltage ripple. The second method uses a proportional-resonant controller to achieve high gain at 120 Hz in the loop-gain. In this way, DAB converters can track the power fluctuation at 120 Hz and then reduce output 120 Hz voltage ripple. Part of section 4 will be submitted to IEEE ECCE 2012.

Finally, the contributions of this work and recommendation for future research are discussed in section 5.

2. DUAL ACTIVE BRIDGE CONVERTERS

This section discusses the circuit configuration, steady state operation, modulation, switching commutation, and circuit design of DAB converters for SSTs. It also describes the analysis and design of a DAB converter prototype as a case study.

This section is organized as follows: subsection 2.1 describes the circuit of a DAB converter, with both dc-dc variant and ac-ac variant discussed. Subsection 2.2 develops the steady state input-output relations of DAB converters. The effect of introducing ac-ac power conversion is stressed. Subsection 2.3 develops the conditions for soft switching and analyzes the range of soft switching of DAB converters at different operating conditions. Subsection 2.5 explains how to implement the switch commutation schemes for DAB converters. Sections 2.6 provides simulation results of DAB converters. Subsection 2.7 describes the design of a 200 W ac-ac DAB converter prototype as a case study. Subsection 2.8 presents the experimental results to verify the theoretical analysis. Finally, subsection 2.9 summarizes the contribution of this section.

2.1. CIRCUIT CONFIGURATION

A DAB converter consists of two switching bridges and one high-frequency transformer. Each switching bridge is made up of four high-frequency active controllable switching devices (MOSFETs or IGBTs) in an H-bridge connection. Such connection is similar to the one used in full-bridge dc-dc converters. However, instead of using uncontrollable switching devices (such as diodes) bridge in the other side of transformer, DAB converters use two active bridges formed by active controllable devices. This is why the name "Dual Active Bridge" is given to this kind of converters.

A transformer is used to provide galvanic isolation between the input side and the output side of a DAB converter. A high-frequency transformer is preferred to reduce the weight and volume of the magnetic core. Compared to those converters using line-frequency transformers, DAB converters uses more silicon devices (whose price is continuously going down) while using less copper and smaller magnetic core (whose price is continuously going up). Besides galvanic isolation, the high-frequency

transformer has some amount of leakage inductance in its primary and secondary windings. The leakage inductance has two purposes: (1) it is used as energy storage components in DAB converters and (2) it reduces the dv/dt across switching devices during commutation transients, facilitates soft switching, and reduces switching losses.

Figure 2.1 shows the circuit schematic of a dc-dc DAB converter. In the schematic, power MOSFETs can be used in place of IGBT-diode pairs. The IGBT-diode pairs can conduct current bidirectionally, so does the channel of power MOSFETs. Therefore, the circuit shown in Figure 2.1 is able to conduct bidirectional current. Furthermore, DAB converters have symmetrical dual active H-bridge configuration, which help achieve bidirectional power flow. On the other hand, such configuration can only block positive voltage. Therefore, the topology shown in Figure 2.1 is only for dc-dc DAB converters.

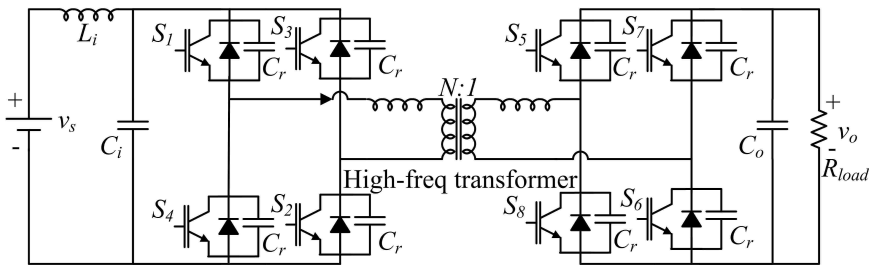

Figure 2.1. DAB converter schematic

An ac-ac DAB converter can be built using a different switching device configuration. Figure 2.2 shows the circuit schematic of an ac-ac DAB converter. Also note that IGBTs can be used in place of power MOSFETs. Since the input and output voltages are both ac, the switches in an SST must block voltage in both polarities. Additionally, they must conduct current in both directions. Therefore, each switch cell consists of two anti-serial connected switching devices.

In both dc-dc converters and ac-ac ones, resonant capacitors are connected in parallel with each switch cell to enable soft switching.

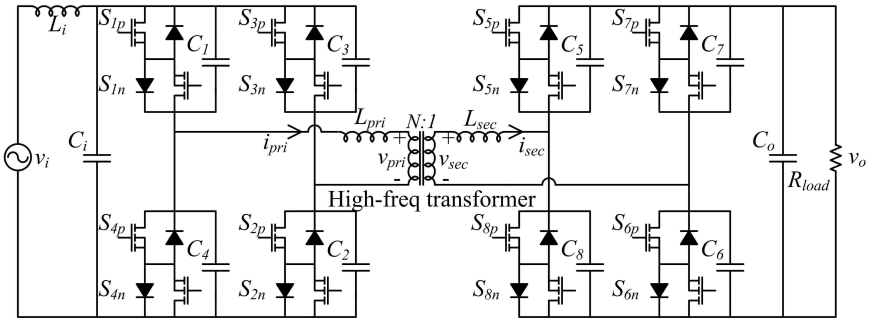

Figure 2.2. DAB converter schematic

The inherent symmetry of the power circuit in a DAB converter ensures bidirectional power flow. Each bridge is controlled using two-level modulation, with fixed 50% duty ratio. A DAB converter is controlled by Phase-Shift Modulation (PSM). Both the direction and the amount of power flow is regulated by controlling the phase shift between the those H-bridges. Power flows from the leading bridge to the lagging bridge. Two operating modes, corresponding to two directions of power flow of a DAB converter, respectively, are given in Figure 2.3(a) and Figure 2.3(b). In Figure 2.3(a), positive power flow is defined as power from the left to the right for the converter shown in Figure 2.1, while in Figure 2.3(b), negative power flow is defined as power from the right to the left. The next section will present the equation that describes the amount of power transferred by a DAB converter.

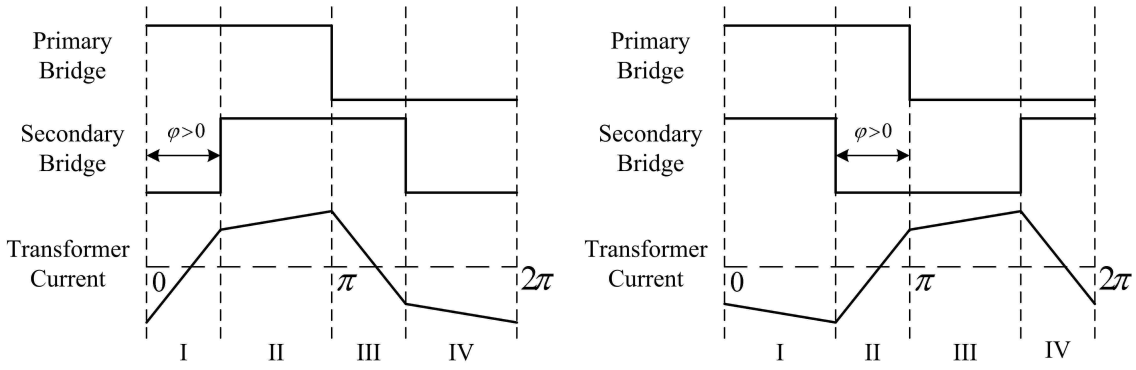

(a) Positive Power Flow (b) Negative Power Flow

Figure 2.3. Operation Modes

2.2. STEADY STATE ANALYSIS

As shown in Figure 1.2, Figure 1.3, and Figure 1.4, the DAB converters in SSTs at the distribution level described in this work is a voltage step-down converter from the high voltage side to the low voltaeg side. With the help of isolation transformers, the voltage transfer ratio can be very large (such as 7200 V:240 V) or very small (such as 240 V:7200 V), depending on the direction of power flow. This makes it difficult to analyze. Furthermore, conventional approaches cannot provide much insight when the voltage level scales (for instance, using an existing design of a 240 V:120 V DAB converter to facilitate the design of a 208 V:120 V DAB converter).

This work derives a per-unit steady-state model of a DAB converter for circuit analysis and converter design. This model works for both dc-dc DAB converters and ac-ac DAB converters. By using a per-unit model, the parameters of both bridges of an DAB converter can be scaled up/down easily to design a voltage step up/down SST.

2.2.1. Steady-State Model of DC-DC DAB Converters. Let v_i, v_o, v_{pri}, and v_{sec} be input voltage, output voltage, transformer primary winding voltage and transformer secondary winding voltage, respectively (as shown in Figure 2.1). $X_{pri} = \omega_s L_{pri}$ and $X_{sec} = \omega_s L_{sec}$ are the transformer leakage impedances due to leakage inductance at primary and secondary winding, respectively, where ω_s represents switching frequency. Assume that the DAB converter is operating in Quadrant 1 (which means positive input voltage and power transferred from the left to the right in Figure 2.1). During Interval I (from 0 to ϕ, as shown in Figure 2.3(a), where ϕ is the phase shift between two bridges), the current at transformer primary side is

$$i_{\phi,pri} = i_{0,pri} + \frac{v_i - v_{pri}}{X_{pri}}\phi, \tag{1}$$

where $i_{\phi,pri}$ and $i_{0,pri}$ are the primary side current at time $\omega_s t = \phi$ and $\omega_s t = 0$, respectively. Similarly, the current at transformer secondary side is

$$i_{\phi,sec} = i_{0,sec} + \frac{v_{sec} - v_o}{X_{sec}}\phi, \tag{2}$$

where $i_{\phi,sec}$ and $i_{0,sec}$ are the secondary side current at time $\omega_s t = \phi$ and $\omega_s t = 0$, respectively.

A per-unit system at both windings can be defined as

$$I_{b,pri} = \frac{S_b}{V_{b,pri}}, \tag{3}$$

$$I_{b,sec} = \frac{S_b}{V_{b,sec}}, \tag{4}$$

$$Z_{b,pri} = \frac{V_{b,pri}^2}{S_b}, \tag{5}$$

and

$$Z_{b,sec} = \frac{V_{b,sec}^2}{S_b}, \tag{6}$$

where S_b is base apparent power; $V_{b,pri}$ and $V_{b,sec}$ are base voltage at primary and at secondary side, respectively; $I_{b,pri}$ and $I_{b,sec}$ are base current at primary and at secondary side, respectively; and $Z_{b,pri}$ and $Z_{b,sec}$ are base impedance at primary and at secondary side, respectively. Base voltages and base apparent power are determined by the specifications of an SST.

By using (3), (4), (5), and (6), all voltage and currrent variables, v_i, v_o, v_{pri}, v_{sec}, $i_{0,pri}$, $i_{0,sec}$, $i_{\phi,pri}$, $i_{\phi,sec}$, can be converted into their corresponding per-unit variables, $v_{i,pu}$, $v_{o,pu}$, $v_{pri,pu}$, $v_{sec,pu}$, $i_{0,pri,pu}$, $i_{0,sec,pu}$, $i_{\phi,pri,pu}$, $i_{\phi,sec,pu}$, respectively. It is also intuitive that

$$i_{0,pri,pu} = i_{0,sec,pu} = i_{0,pu}, \tag{7}$$

$$i_{\phi,pri,pu} = i_{\phi,sec,pu} = i_{\phi,pu}, \tag{8}$$

and

$$v_{pri,pu} = v_{sec,pu} = v_{t,pu}. \tag{9}$$

The transformer leakage reactance can be lumped as $X_{pu} = X_{pri}/Z_{b,pri} + X_{sec}/Z_{b,sec}$. Using the per-unit system defined above and substituting all per-unit variables into

(1) and (2), the per-unit transformer current is

$$i_{\phi,pu} = i_{0,pu} + \frac{v_{i,pu} + v_{o,pu}}{X_{pu}}\phi. \tag{10}$$

Similarly, during Interval II (from ϕ to π, as shown in Figure 2.3(a)), the transformer current is

$$i_{\pi,pu} = i_{\phi,pu} + \frac{v_{i,pu} - v_{o,pu}}{X_{pu}}(\pi - \phi). \tag{11}$$

In steady state, the transformer current is symmetrical every half switching period $i_{\pi,pu} = -i_{0,pu}$. Therefore, $i_{0,pu}$ and $i_{\phi,pu}$ are calculated as

$$i_{0,pu} = \frac{1}{2X_{pu}}\left((\pi - 2\phi)\, v_{o,pu} - \pi v_{i,pu}\right), \tag{12}$$

$$i_{\phi,pu} = \frac{1}{2X_{pu}}\left(\pi v_{o,pu} - (\pi - 2\phi)\, v_{i,pu}\right). \tag{13}$$

From (12) and (13), the input current averaged over one switching period is

$$\hat{i}_{i,pu} = \frac{1}{2\pi}\left(\pi i_{\phi,pu} + (2\phi - \pi)\, i_{0,pu}\right) = \frac{v_{o,pu}}{X_{pu}}\phi\left(1 - \frac{\phi}{\pi}\right). \tag{14}$$

The amount of power transferred to the load is controlled by the phase shift angle between two bridges ϕ, the input voltage, and the output voltage, as described in (15),

$$P_o = \frac{v_{i,pu} v_{o,pu}}{X_{pu}}\left(\phi - \frac{\phi^2}{\pi}\right). \tag{15}$$

Ideally, when the loss of a converter is insignificant, output power is equal to input power:

$$P_i = v_{i,pu}\hat{i}_{i,pu} = P_o = v_{o,pu}^2 / R_{pu}, \tag{16}$$

where $R_{pu} = \frac{R}{Z_{b,sec}}$ and R is load resistance. Using per-unit notation, the ideal dc

voltage transfer ratio is

$$\gamma = \frac{v_{o,pu}}{v_{i,pu}} = \frac{R_{pu}}{X_{pu}}\phi\left(1 - \frac{\phi}{\pi}\right). \tag{17}$$

Equation (17) shows that the voltage transfer ratio of a dc-dc DAB converter is determined by transformer leakage inductance, phase shift between bridges, and load resistance.

2.2.2. Steady-State Model for AC-AC DAB Converters. The steady-state model in (17) is valid for dc-dc DAB converters, in which the output capacitor has infinite impedance at dc. However, (17) does not hold true for the ac-ac case when there exists an output filter and the impedance of capacitor is no longer infinite for an ac frequency (for example, at 60 Hz).

In the steady state of an ac system, (16) becomes

$$P_i = v_{i,pu}\hat{i}_{i,pu} = P_o = \frac{v_{o,pu}^2}{R_{pu}} + \frac{d}{dt}\left(\frac{1}{2}C_{pu}v_{o,pu}^2\right), \tag{18}$$

where $C_{pu} = C \cdot Z_{b,sec}$ and C is filter capacitance. Converted (18) into the frequency domain, the voltage transfer ratio becomes

$$\gamma_{ac} = \frac{1}{X_{pu}}\phi\left(1 - \frac{\phi}{\pi}\right)\frac{R_{pu}}{sR_{pu}C_{pu} + 1}. \tag{19}$$

According to (19), output voltage will vary sinusoidally as input voltage varies. Because ac-ac DAB converters use four-quadrant switching cells (as shown in Figure 2.2), this ratio holds regardless of the polarity of input voltage and the direction of transformer current. In steady state, output voltage follows input voltage sinusoidally. The load and output filter introduce a small phase shift between input and output voltages in steady state. This shows the feasibility of applying ac-ac DAB converters as galvanically-isolated fixed-frequency SSTs. Note that this steady-state model is valid for frequencies much lower than the switching frequency. This is generally the case because the switching frequency is in the range of kilo-hertz and it is much higher than the 60 Hz line frequency.

2.3. SOFT SWITCHING ANALYSIS

Figure 2.4(a) shows the soft switching transient of the primary bridge in the first operating quadrant. At the end of switching interval I, S1p and S2p are turned off. No switch is conducting during the soft switching transient. The four capacitors in parallel with the switch cells and transformer leakage inductor resonate. Switches S3n and S4n are turned on while C1 and C2 are charging and C3 and C4 are discharging. They begin to conduct when the voltages of C3 and C4 reach zero, realizing zero voltage turn-on for incoming switches S3n and S4n. When soft switching is not valid, hard switching is carried out by the switching devices as shown in Figure 2.4(b).

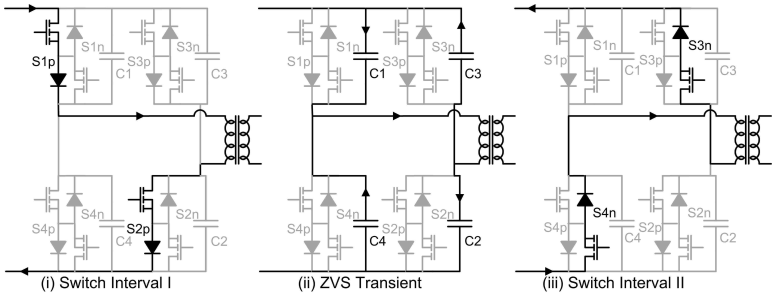

(a) Soft switching

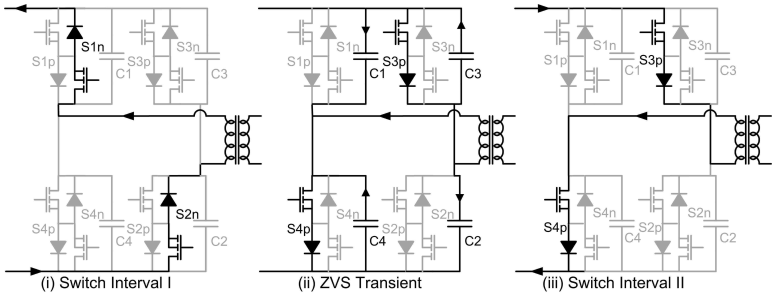

(b) Hard switching

Figure 2.4. Switch commutation transients

There are three switching states in every half switching period, two switching intervals and one switching transient. It is possible to solve the dynamic equations of all three states analytically. But the resulting transcendental equations complicate

analysis and do not provide much physical insight for converter design. An alternative is to exclude switching transients at first and include their effects later.

Soft switching requires adequate energy storage in the leakage inductor to charge the resonant capacitors that are in parallel with the outgoing switches and to discharge the resonant capacitors that are in parallel with the incoming switches. Resonant capacitors are chosen according to the transient behavior of the switching device. Define a per-unit ZVS admittance as $Y_{res,pu} = 2\sqrt{\frac{C_r}{L_l}} \cdot Z_b$ where C_r is the resonant capacitance across the switching cells, L_l is the lumped leakage inductance of the high-frequency transformer winding, and Z_b is the base impedance respect to the SST side of interest. According to [11], the minimum per-unit transformer current for soft switching is

$$I_{min,pu} = Y_{res,pu}\sqrt{v_{i,pu}v_{o,pu}}. \tag{20}$$

According to Figure 2.3(a), the conditions for soft switching in Quadrant 1 are $i_{0,pu} < -I_{min,pu}$ and $i_{\phi,pu} > I_{min,pu}$. Substitute (17) into (12), (13), and (20) to find the soft switching criteria:

$$\frac{2R_{pu}}{\pi X_{pu}}\phi^3 - \frac{3R_{pu}}{X_{pu}}\phi^2 + \frac{\pi R_{pu}}{X_{pu}}\phi - \pi < -\Psi, \tag{21}$$

$$-\frac{R_{pu}}{X_{pu}}\phi^2 + \left(\frac{\pi R_{pu}}{X_{pu}} + 2\right)\phi - \pi > \Psi, \tag{22}$$

where $\Psi = 2Y_{res,pu}\sqrt{R_{pu}X_{pu}}\sqrt{\phi - \frac{\phi^2}{\pi}}$. A similar analysis can be applied when $\phi < 0$ and power flows in the opposite direction (as shown in Figure 2.3(b). The currents at $\omega_s t = \pi$ and $\omega_s t = \phi$ become

$$i_{0,pu} = \frac{1}{2X_{pu}}\left(\pi v_{i,pu} - (\pi - 2\phi)\, v_{o,pu}\right) \tag{23}$$

$$i_{\phi,pu} = \frac{1}{2X_{pu}}\left((\pi - 2\phi)\, v_{i,pu} - \pi v_{o,pu}\right). \tag{24}$$

Conditions are then $i_{0,pu} > I_{min,pu}$ and $i_{\phi,pu} < -I_{min,pu}$ (Figure 2.3(b)). The minimum leakage inductor current for ZVS is unchanged. Thus, the soft switching criteria given in (21) and (22) are still valid for negative power flow. Note that this soft-switching

analysis uses a per-unit system. Therefore, the results can be easily scaled up or down to match designs at various voltage ratings and voltage transfer ratios.

Figure 2.5(a) and 2.5(b) combine the results of (21), (22) and (15). Figure 2.5(a) shows the effect of transformer leakage inductance on soft-switching range (solid lines). The voltage transfer ratio fixed at 1.0 pu. It illustrates whether soft switching is valid when output power varies and voltage transfer ratio is fixed at 1.0 pu. Increasing leakage inductance results in a wider soft-switching range. However, high leakage inductance limits power output capability. Figure 2.5(b) shows the effect of load power factor on soft-switching range. The shaded area represents soft switching range. The voltage transfer ratio fixed at 1.0 pu and leakage inductance is fixed. As load power factor becomes lower, more phase shift between input and output voltages causes narrower soft-switching range.

2.4. LOSS EVALUATION

One challenge for SSTs is the need for high power efficiency. Power losses in a DAB converter come in the forms of conduction loss and switching loss of power circuit, as well as core loss and copper loss in the high-frequency transformer. This section focuses on the quantitative analysis of losses in the power semiconductors and the high-frequency transformers of DAB converters. The calculation in this section will focus on loss evaluation of ac-ac DAB converters.

2.4.1. Conduction Loss. Each power semiconductor device in the current conduction path has forward voltage, which contributes to conduction loss. The forward voltage can be modeled as $v_{ce} = v_{ce0} + R_{on,t} i_f$ for an IGBT, $v_{ds} = R_{on,m} i_f$ for a MOSFET, and $v_f = v_{f0} + R_{on,d} i_f$ for a diode [133], where v_{ce0} is the static forward voltage for an IGBT, v_{f0} is the static forward voltage for a diode, and $R_{on,t}$, $R_{on,m}$, and $R_{on,d}$ are the on-time resistance for an IGBT, a MOSFET, and a diode, respectively. In each four-quadrant switch cell of an ac-ac DAB converter, the conduction path always consists of two devices, regardless of current direction. Therefore, the forward voltage drop is $v = (v_{ce0} + v_{f0}) + i_f (R_{on,t} + R_{on,d})$ when using IGBTs and $v = 2 i_f R_{on,m}$ when using MOSFETs.

According to Figure 2.3(a), the piecewise linear transformer current approximation consists of three parts: two triangular parts and one trapezoidal part. Using the

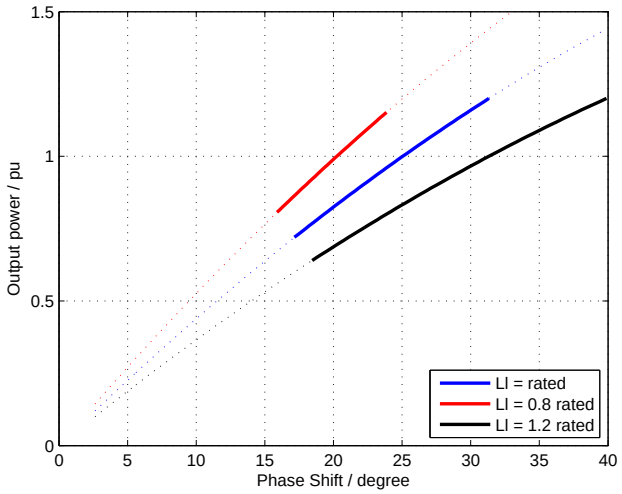

(a) Effect of leakage inductance on soft switching range

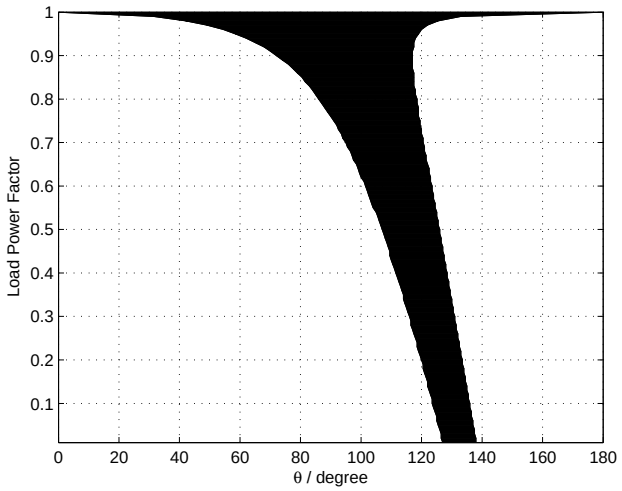

(b) Effect of load power factor on soft switching range

Figure 2.5. Soft switching analysis.

waveform symmetry over half-cycle, the RMS current at the primary side of transformer is

$$I_{rms,pri} = \sqrt{\frac{1}{3\pi}\left(i_{0,pri}^2\tau + i_{\phi,pri}^2(\phi-\tau) + (\pi-\phi)\left(i_{0,pri}^2 + i_{\phi,pri}^2 - i_{0,pri}i_{\phi,pri}\right)\right)}, \quad (25)$$

where $\tau = \frac{i_{0,pri}}{i_{0,pri}-i_{\phi,pri}}\phi$.

In steady state, phase shift ϕ can be calculated using (17). The expressions in (12) and (13) can be converted into SI system. The RMS current of the high

frequency transformer in an ac-ac DAB converter is calculated using the symmetry of transformer current:

$$I_{rms,pri} = \frac{1}{\sqrt{3}}\sqrt{i_{0,pri}^2 + i_{\phi,pri}^2 - i_{0,pri}i_{\phi,pri} + \frac{2\phi}{\pi}i_{0,pri}i_{\phi,pri}}. \tag{26}$$

The RMS current at the secondary side of transformer $I_{rms,sec}$ can be calculated in a similar way.

Finally, the conduction loss of two bridges is

$$P_{cond} = 2R_{on}I_{rms,pri}^2 + 2R_{on}I_{rms,sec}^2. \tag{27}$$

2.4.2. Switching Loss. As discussed in Section 2.3, ac-ac DAB converters experience both soft switching and hard switching during a single 60-Hz cycle. The number of soft switching events over that of hard switching events depends on circuit parameters and load conditions.

When designed properly, an ac-ac DAB converter allows soft switching most of the time. Switching devices are turned on and off with ZVS. Therefore, ZVS turn-on energy for one four-quadrant switch is close to zero, and turn-off energy can be calculated as

$$E_{soft} = \frac{(t_f I_{sw})^2}{12C_r}, \tag{28}$$

where t_f is the fall time of switching device, I_{sw} is the current during switching commutation, and C_r is the snubber capacitance.

Soft switching is not valid when voltage is zero-crossing or when load is too light. In these situations, hard-switching commutation is used. Hard-switching losses include device switching loss and the energy loss in the snubber capacitors.

$$E_{hard} = E_{on} + E_{off} + \frac{1}{2}C_r V^2, \tag{29}$$

where the turn-on energy E_{on} and turn-off energy E_{off} of a switching device can be found in the manufacture's datasheet. Thus, the switching loss of ac-ac DAB

converters is

$$P_{sw} = f_{sw}\left(\frac{N_{soft}}{N}E_{soft} + \frac{N_{hard}}{N}E_{hard}\right), \tag{30}$$

where N is the number of switching commutation events is a single 60-Hz cycle, N_{soft} and N_{hard} are the numbers of soft-switching and hard-switching events, respectively, in one grid cycle.

Note that the switching loss of an ac-ac DAB converter is slightly different from that of its dc-dc counterpart. Both i_0 and i_ϕ vary sinusoidally. ZVS is invalid around zero-crossing points. However, the extra hard switching losses are not significant because the voltage is also low around those points.

2.4.3. Copper Loss. The transformer in an ac-ac DAB converter operates at a frequency range of several kilo-hertz where the skin depth of wire is close to the wire diameter. Therefore, the high-frequency effect on winding resistance can be significant. The ac winding resistance of a high-frequency transformer is calculated using the orthogonality between skin effect and proximity effect [134]. AC resistance is the product of dc resistance and a factor representing skin and proximity effects:

$$k = \frac{\sinh\xi(\eta) + \sin\xi(\eta)}{\cosh\xi(\eta) - \cos\xi(\eta)} + \eta^2\left(2m-1\right)\frac{\sinh\xi(\eta) - \sin\xi(\eta)}{\cosh\xi(\eta) + \cos\xi(\eta)}, \tag{31}$$

where $\xi(\eta) = \frac{\sqrt{\pi}}{2}\frac{d}{\delta(\eta)}$ and $\delta(\eta) = \frac{1}{\sqrt{\pi f \mu_0 \eta/\rho}}$. The dc component of winding resistance is $R_{dc} = \frac{\rho N l_T}{A}$ where N is the total number of turns and A is the copper area of the wire. Copper loss is calculated using winding ac resistance and RMS current:

$$P_{cu} = I_{rms,pri}^2 R_{ac,pri} + I_{rms,sec}^2 R_{ac,sec}. \tag{32}$$

2.4.4. Core Loss. According to [135], peak flux density is

$$B_{ac} = \frac{V_{rms} \times 10^4}{4.44 N f A_e}, \tag{33}$$

where A_e is the core area of the magnetic core. Core loss depends on magnetic flux, operating frequency, the core weight, and the voltage waveform. For simplicity, it is

given by

$$P_{core} = kf^m B_{ac}^n, \tag{34}$$

where parameters k, m, and n for a given core material can be found in [135] or the manufacturer's datasheets.

2.5. SWITCH COMMUTATION SCHEMES

DC-DC DAB converters use the IGBT-diode pairs (or power MOSFETs) that normally appear in single-phase dc-ac inverters. Therefore, the existing commutation method for inverters can be applied to dc-dc DAB converters.

However, ac-ac DAB converters use four-quadrant switches, which makes switching commutation difficult. Multistep commutation schemes are normally used for hard switching [6] because inductive current should not be open and capacitive voltage should not be shorted. One advantage of the proposed ac-ac DAB converter is that it permits soft switching over a wide range. Inductive current can be conducted through capacitors when no switching device is conducting during soft switching commutation. This approach makes switch commutation less challenging. However, as discussed in [4], the criteria for ZVS cannot be met for all operating conditions. Therefore, a method to transition seamlessly between soft and hard switching must be developed. This work presents a novel switch commutation scheme to permit both soft switching and hard switching that uses transformer current as a reference signal. Table 2.1 summarizes the commutation sequence. Figure 2.6 demonstrates that this commutation scheme is suitable for both switching scenarios. The switching commands are the same for switches in a pair, e.g., S_{1p} is the same as S_{2p} while S_{3n} is the same as S_{4n}.

There are three transient switching states. As shown in Figure 2.6(a), before switching commutation, S_{1p}, S_{1n}, S_{2p}, and S_{2n} are conducting. The transformer current is positive enough to satisfiy the conditions for soft switching. At t_0, the nonconducting switches (S_{1n} in this case) are turned off. Since S_{1p} is still conducting, S_{1n} is turned off at zero voltage. The first transient state (t_0 – t_1) is relatively short, just for the nonconducting switches to turn off. At t_1, the to-be-conducting switches

Table 2.1. Current-based Commutation

	$i_t > 0$					$i_t < 0$				
	S1	Transient			S2	S1	Transient			S2
time	$< t_0$	t_0-t_1	t_1-t_2	t_2-t_3	$> t_3$	$< t_0$	t_0-t_1	t_1-t_2	t_2-t_3	$> t_3$
S1p	1	1	1	0	0	1	0	0	0	0
S1n	1	0	0	0	0	1	1	1	0	0
S2p	1	1	1	0	0	1	0	0	0	0
S2n	1	0	0	0	0	1	1	1	0	0
S3p	0	0	0	0	1	0	0	1	1	1
S3n	0	0	1	1	1	0	0	0	0	1
S4p	0	0	0	0	1	0	0	1	1	1
S4n	0	0	1	1	1	0	0	0	0	1

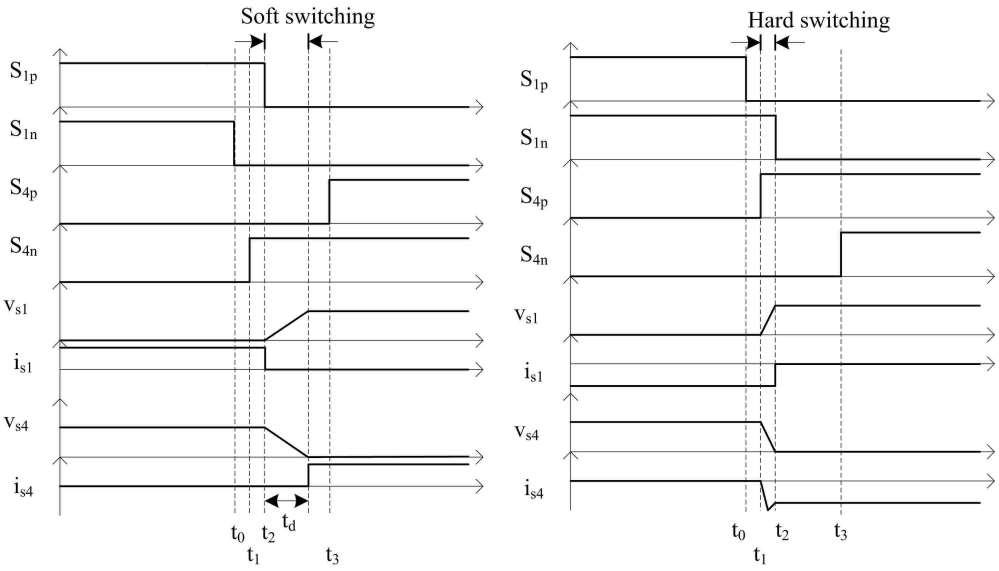

(a) Soft switching case (b) Hard switching case

Figure 2.6. Switch commutation from S1 to S2

(S_{4n}) in the incoming switching cells are turned on. However, it does not begin conducting because the diode in parallel with S_{4p} is reverse-biased. Thus, S_{4n} is turned on at zero current. At t_2, turning off the outgoing switches (S_{1p}) starts the resonating

commutation. C_1 is being charged while C_4 is being discharged. No switch conducts during this process, and the dv/dt across switches is limited. After completing the commutation from the outgoing to the incoming switch cells, S_{4p} is turned on at zero voltage at t_3. The switch cells are again ready to conduct bidirectional current and the converter enters another conducting state. All four switching devices commutates at soft switching.

At the operating point shown in Figure 2.6(b), the transformer current is negative before the switching transient, meaning soft switching is not valid. However, the same commutation scheme can be applied. Commutation process begins with turning off the nonconducting switches at t_0. They turn off at zero voltage. Then at t_1, the incoming switches are turned on at hard switching. The energy stored in C_4 is also discharged through S_{4p} during t_1 to t_2, resulting an inrush current spike. Because the dv/dt is not controlled, it is a hard-switching event. During this process, C_1 is charged by the source voltage. Once the voltage on C_1 rises, S_{1n} stops conducting because the diode is reverse-biased. At t_2, the outgoing switches (S_{1n}) are turned off. And at t_3, S_{4n} turns on. The converter enters another conducting state and hard switching commutation ends.

Since a switching device cannot be turned on or off instantaneously in practice, it is necessary to insert deadtime in the commutation scheme described above. The time interval from t_0 to t_1 must be long enough to turn off non-conducting switches, and the time interval from t_1 to t_2 must be long enough to turn on incoming switches. Considering device switching specifications and safety margin, the deadtimes t_0 to t_1 and t_1 to t_2 are both 400 ns in the experimental system described in Section 2.8. Out-going switches must be turned off after ZVS transients, which means $t_3 - t_2 > t_d$, where t_d is the amount of time to complete ZVS transients. The dv/dt across the switching device can be approximated by

$$\frac{dv}{dt} = \frac{V}{t_d} = \frac{i_t}{C_r}, \tag{35}$$

where V is the voltage across C_i or C_o, i_t is transformer current during commutation,

and C_r is resonant capacitor. Therefore, the deadtime for ZVS transient is

$$t_d = C_r \frac{V}{i_t}. \tag{36}$$

t_d is a design trade-off. Switching energy is low if C_r is large. However, large C_r leads to large t_d. In (36), t_d is small if i_t is large, which means soft switching range is limited. However, t_d is too long if a very wide soft switching range is required. When V varies sinusoidally over a period of 60 Hz, i_t also varies sinusoidally. Therefore, the peak voltage and current can be used.

2.6. SIMULATION RESULTS

To verify the above theoretical analysis and design, the present work developed an ac-ac DAB converter simulation model using PLECS. The circuit parameters are compiled in Table 2.2. Two operating points were simulated, and the results are shown in Figure 2.7 – 2.8.

The first case is a phase shift of $\phi = 35^\circ$ and $R_{load} = 100\ \Omega$ (1.0 pu), which is in the ZVS range. Figure 2.7(a) indicates that the transformer current changes direction correctly and that there is adequate energy to realize ZVS. The second case is for a phase shift of $\phi = 14^\circ$ and $R_{load} = 300\ \Omega$ (3.0 pu), which is outside the ZVS range. Figure 2.7(b) shows that the transformer current does not change direction at $\omega_s t = \phi$, so that ZVS is not valid at the secondary bridge.

Figure 2.8(a) shows that output voltage is nearly sinusoidal, which is an advantage of high-switching frequency. Switching ripple is apparent, but it could be reduced with additional output filter if necessary. Figure 2.8(b) is the zoom-in of Figure 2.8(a) around voltage zero-crossing. It clearly shows the small phase shift between input voltage and output voltage, which can be predicted by (19). It also confirms that soft switching is not valid around voltage zero-crossing points.

2.7. HARDWARE DESIGN

This section addresses the hardware design an ac-ac DAB converter. It discusses the selection of key components and high-frequency transformer design for a proof-of-concept 200 W 220 V/120 V ac-ac DAB converter.

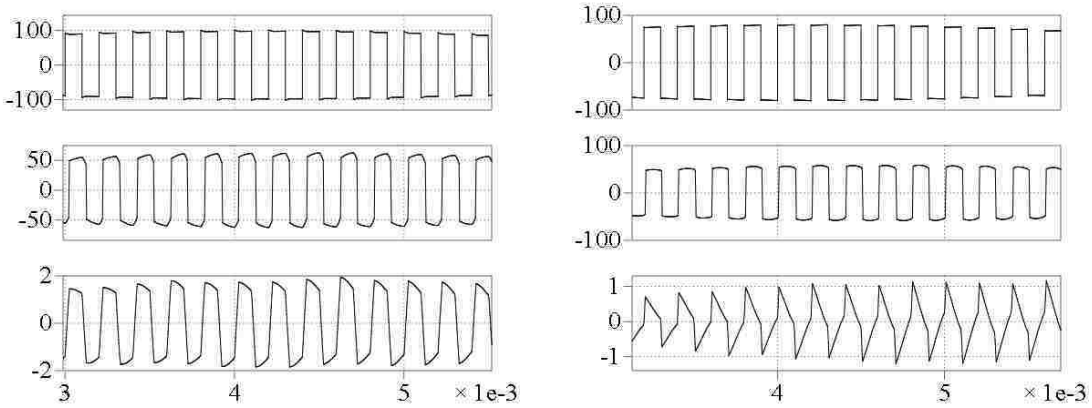

(a) Simulation Waveforms with ZVS.

(b) Simulation waveforms without ZVS.

Figure 2.7. Simulation Waveforms. Upper line: primary side transformer voltage (V), middle line: secondary side transformer voltage (V), lower line: transformer current (A)

Peak voltages on both sides of converter are approximately 300 V and 170 V, respectively. Considering enough safety margin, switching devices rated at 600V are selected. Peak currents can be calculated using (14) and (15). Device current rating is chosen to be 7 A. For designing simple gate drivers, it is preferable to use high-voltage power MOSFETs, such as those using CoolMOS or SuperMESH technologies. Two anti-series connected MOSFETs form one four-quadrant switching cell. Turning both MOSFETs on permits conduction of bidirectional current, as in synchronous rectification. A total of sixteen MOSFETs is used for an ac-ac DAB converter.

As mentioned before, the resonant capacitors in parallel of the each switch is a design trade-off. In this study, soft switching is valid until power is less than 0.3 pu. For instance, at the low voltage side, the rated output RMS voltage is 120 V and the rated output RMS current is 1.2 A. Given a design choice of $C_r = 4.7$ nF, an input voltage of $V = 120$ V, and load point corresponding to 0.3 pu power is $i_t = 0.3 \times 1.2 = 0.36$ A, $t_d = 1.56\mu s$ according to (36). Therefore, the deadtime from t_2 to t_3 is chosen to be $t_d = 2\mu s$. The deadtime for the high voltage side is calculated in a similar way.

The next step in circuit design is to select the necessary amount of inductance in the transformer windings using the per-unit model presented in the previous sections.

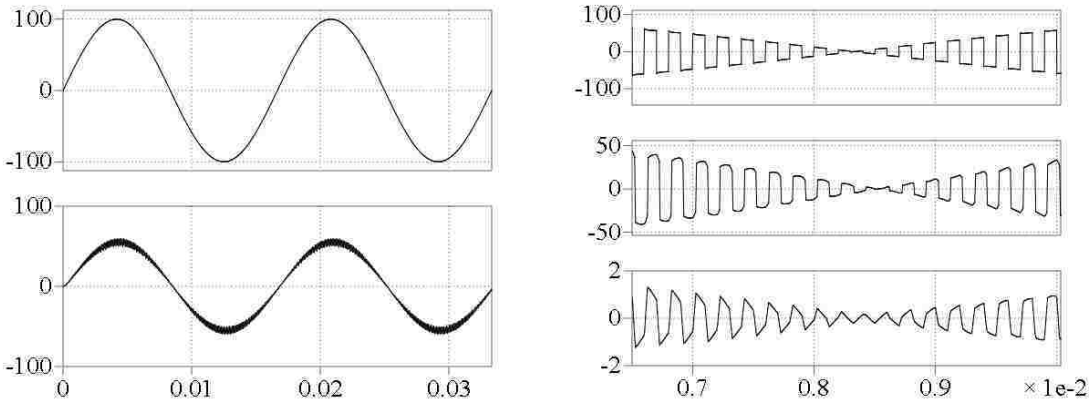

(a) Input voltage and output voltage waveforms. (b) Simulation waveforms at voltage zero-crossing.

Figure 2.8. Simulation results. For waveforms in (a), upper trace is input voltage (V) and lower trace is output voltage (V). For waveforms in (b), upper trace is primary side transformer voltage (V), middle trace is secondary side transformer voltage (V), and lower trace is transformer current (A).

The converter specification is 200 W, 220 V input, and 120 V output. Therefore, base power $S_b = 200$ W, primary side base voltage $V_{b,pri} = 220$ V, secondary side base voltage $V_{b,sec} = 120$ V, primary side base impedance $Z_{b,pri} = \frac{V_{b,pri}^2}{S_b} = 216\ \Omega$, and secondary side base impedance $Z_{b,sec} = \frac{V_{b,sec}^2}{S_b} = 72\ \Omega$. The phase shift at rated operating point is chosen to be $\phi = 35° = 0.61$ rad/s. According to (17), the per-unit transformer winding reactance is

$$X_{pu} = \frac{R_{pu}}{\gamma}\phi\left(1 - \frac{\phi}{\pi}\right) = 0.683 \text{ pu}, \tag{37}$$

where the per-unit load resistance $R_{pu} = 1.39$ (100 Ω in SI), and per-unit voltage transfer ratio $\gamma = 1.0$ at the rated operating point. If the transformer inductance is equally distributed between two windings and the switching frequency is chosen to be $f_s = 10$ kHz, the inductance of the primary side is

$$L_{pri} = \frac{1}{2}\frac{X_{pu}Z_{b,pri}}{2\pi f_s} = 1174\ \mu\text{H}, \tag{38}$$

and the inductance of the secondary side is

$$L_{sec} = \frac{1}{2}\frac{X_{pu}Z_{b,sec}}{2\pi f_s} = 391\ \mu\text{H}, \tag{39}$$

Therefore, the primary winding inductance is set to 1200μH, while the secondary winding inductance is set to 360μH.

The high-frequency transformer plays an important part in an ac-ac DAB converter. A ferrite magnetic core ETD–49 was used here because it has high saturation flux density and low core loss. Table 2.2 and Table 2.3 summarize circuit parameters and transformer design specifications, respectively.

Table 2.2. Circuit Parameters

Inductance, HV	Inductance, LV	Switch Frequency
1200 μH	360 μH	10 kHz
ZVS Capacitor, HV	ZVS Capacitor, LV	Switching Device
2.7 nF	4.7 nF	ST STD8NM60ND 600V 7A MOSFET
Input Capacitor	Output Capacitor	Load Resistor
3 μF	4 μF	100Ω

Table 2.3. Transformer Design

Core Type	Ferrite ETD49
Peak Flux Density	0.2 T
Core Area	2.11 cm^2
Window Area	2.73 cm^2
wire, HV	120 turns AWG 20
wire, LV	70 turns AWG 20
MMF Layout	HV: 3 portions, 1 layers LV: 2 portions, 1 layer

A controller for the ac-ac DAB converter was implemented in a single-chip Cyclone II series FPGA from Altera. It reads input voltage polarity and transformer current direction signals, feeds them to a look-up table, and then outputs PWM signals. Figure 2.9 shows the controller block diagram of the ac-ac DAB converter. A picture of the experimental prototype is shown in Figure 2.10.

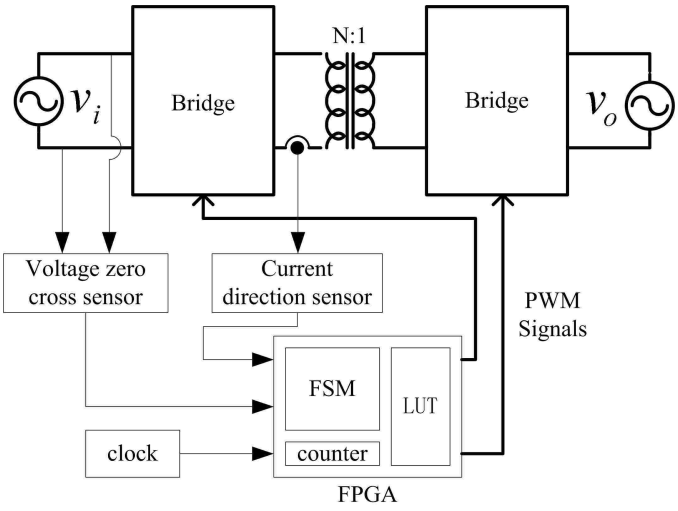

Figure 2.9. Hardware diagram

2.8. EXPERIMENT RESULTS

This section presents the experimental results of the 200 W, 220 V/120 V ac-ac DAB converter prototype discussed in the previous section.

Figure 2.11(a) and Figure 2.11(b) show the waveforms of input and output voltages and currents at 1.0 pu input voltage, in forward and reversed power flow direction, respectively. Input and output currents are sinusoidal. Output voltage follows input voltage, with a small phase shift as predicted in (19) and the simulation results in [4]. In Figure 2.11(b), current becomes out-of-phase of voltage because power is flowing in reversed direction. It confirms that the ac-ac DAB converter allows bi-directional power flow. Figure 2.11(c) shows the waveforms at 0.9 pu input

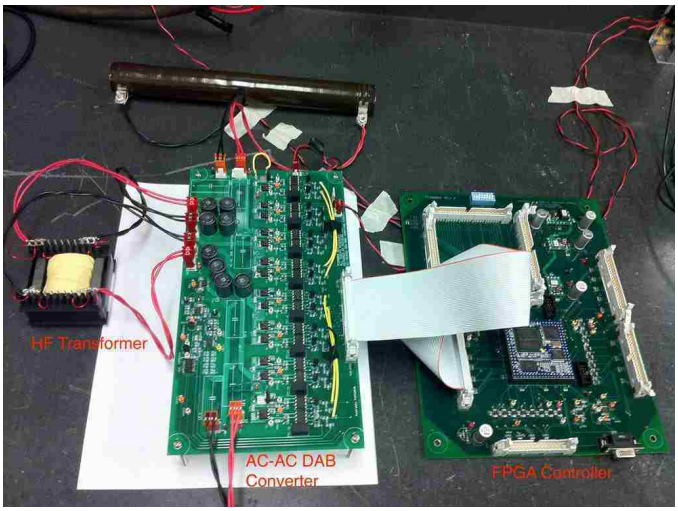

Figure 2.10. Experimental Prototype

voltage. It confirms that an input voltage sag can be compensated by varying the phase shift in the ac-ac DAB converter.

Figures 2.12(a) and 2.12(b) show the soft-switching transient from S_{4p} and S_{4n} to S_{1p} and S_{1n} in the first quadrant. S_{1p} is turned on after its drain-to-source voltage becomes zero. S_{4p} and S_{4n} are turned off when their drain-to-source voltages are zero. S_{1n} is turned on when its drain current is zero. The current ringing in Figure 2.12(b) is the result of body diode reverse recovery. Therefore, S_{1p}, S_{4p}, and S_{4n} switch at zero voltage, while S_{1n} switches at zero current. Figures 2.12(c) and 2.12(d) show the soft-switching transient from S_{8p} and S_{8n} to S_{5p} and S_{5n} in the third quadrant. Similar results are observed at the low voltage side. S_{5n} is turned on after its drain-to-source voltage becomes zero. S_{8p} and S_{8n} are turned off when their drain-to-source voltages are zero. S_{5p} is turned on when its drain current is zero. Therefore, S_{5n}, S_{8p}, and S_{8n} switch at zero voltage, while S_{5p} switches at zero current. The circuit of an ac-ac DAB converter is symmetric. So soft switching is valid for other switches.

Figure 2.13(a) shows transformer voltage and current waveforms. The direction of current permits soft switching for commutation at both primary and secondary bridges. Figure 2.13(b) shows the transformer voltage and current around zero-crossing points. A small phase shift occurs between primary and secondary voltages, as predicted in (19).

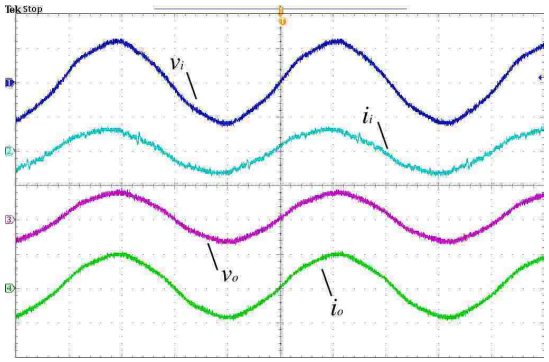

(a) Experiment waveforms of 1.0 pu input voltage.

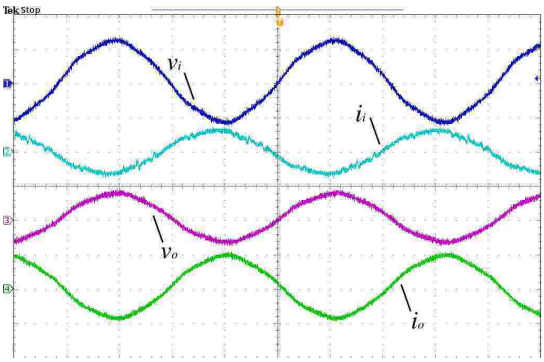

(b) Experiment waveforms of reverse power flow.

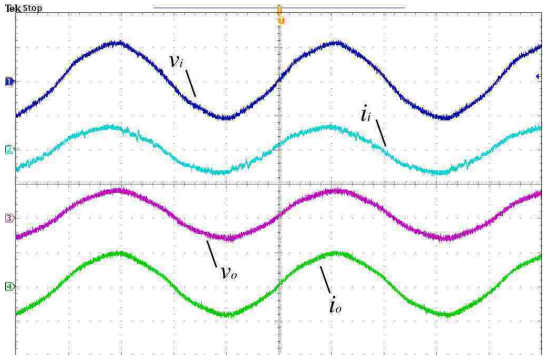

(c) Experiment waveforms of reverse power flow.

Figure 2.11. Input and Ouput Waveforms. From top, v_i (250 V/div), i_i (2 A/div), v_o (250 V/div), i_o (2 A/div), 4 ms/div.

Figure 2.14(a) and Figure 2.14(b) show the soft-switching range under RL loads. In this case, the load impedance is 1.0 pu and its power factor is 0.86 lagging. Figure 2.14(a) marks the soft switching range and Figure 2.14(b) is a zoomed-in view of Figure 2.14(a). The soft switching range begins at the point in the 60 Hz cycle where the current at ϕ is positive to drive the soft switching transients and it ends when the current at π becomes too low to drive the soft switching transients. The circuit is symmetric, so that the same range applies near both the positive peak and the negative peak. In Figure 2.14(b), soft switching is only valid around 80 degrees to 120 degrees during one 60 Hz period, which is consistent with the calculated result given by Figure 2.5(b). This experiment verifies that the soft-switching range decreses as load power factor decreases.

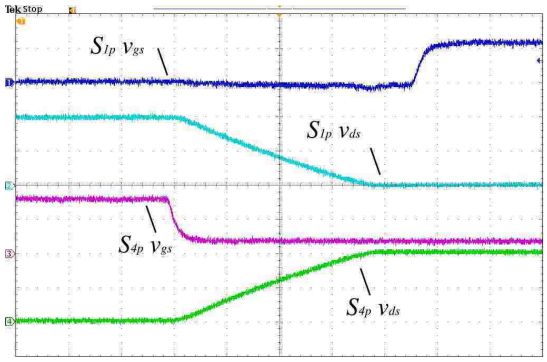

(a) Soft switching at Quadrant I: S_{1p} and S_{4p}.

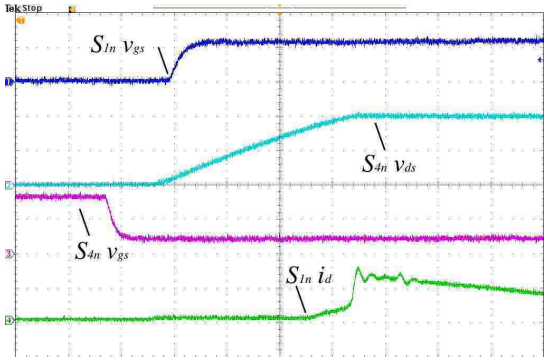

(b) Soft switching at Quadrant I: S_{1n} and S_{4n}.

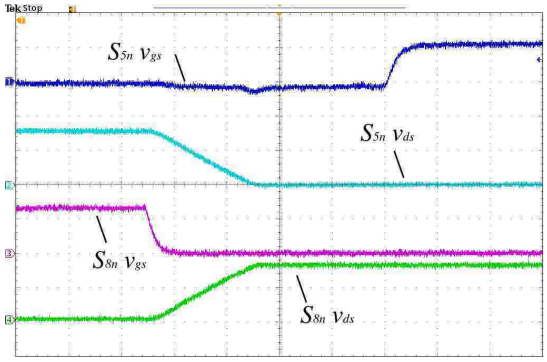

(c) Soft switching at the Quadrant III: S_{5n} and S_{8n}

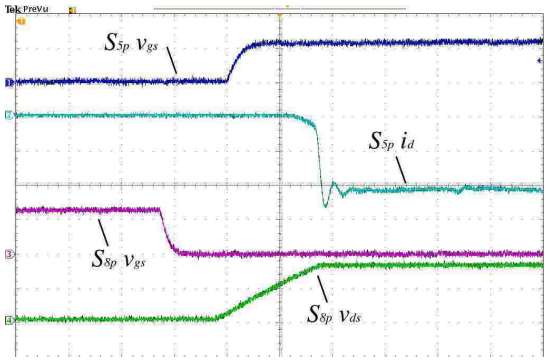

(d) Soft switching at the Quadrant III: S_{5p} and S_{8p}

Figure 2.12. Switch transient experiment results. For (a), from top, V_{gs} (10V/div), V_{ds} (100V/div), V_{gs} (10V/div), V_{ds} (100V/div), 400 ns/div. For (b), from top, V_{gs} (10V/div), V_{ds} (100V/div), V_{gs} (10V/div), I_d (1A/div), 400 ns/div. For (c), from top, V_{gs} (10V/div), V_{ds} (100V/div), V_{gs} (10V/div), V_{ds} (100V/div), 400 ns/div. For (d), from top, V_{gs} (10V/div), I_d (2A/div), V_{gs} (10V/div), V_{ds} (100V/div), 400 ns/div.

Figure 2.15 shows the output voltages at different input voltages. Test results of a MassGI isolated transformer is provided as comparison. The MassGI product is a commercial "transformer" that uses the circuit topology and control method of [6]. The output voltage of the MassGI isolated transformer varies if its input voltage is changed. On the other hand, the output voltage of the proposed ac-ac DAB converter can be regulated when input voltage varies. Figure 2.15 clearly indicates that the proposed ac-ac DAB converter is able to regulate output voltage and compensate variations in input voltage.

Figure 2.16 shows the calculated and measured efficiency of a prototype ac-ac DAB converter. Efficiency calculation was based on the loss evaluation methods

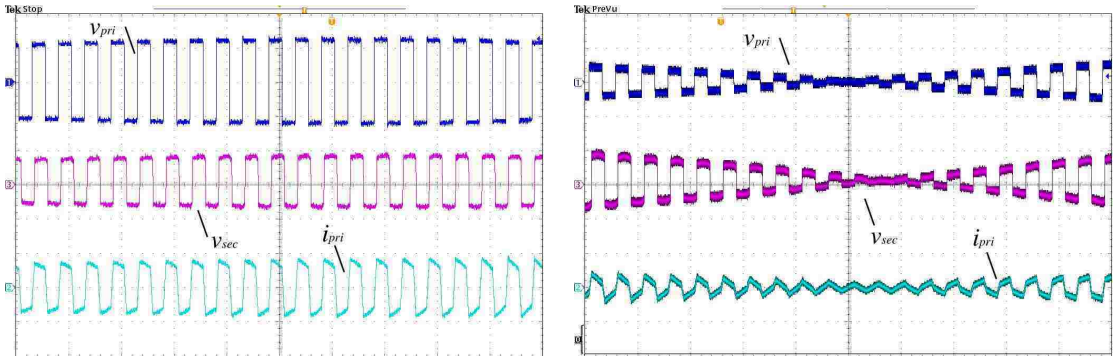

(a) Transformer waveform around peak voltage. (b) Transformer waveform around voltage zero crossing.

Figure 2.13. Transformer waveforms. From top, v_{pri} (250 V/div), v_{sec} (250 V/div), i_{pri} (2 A/div), 200 us/div.

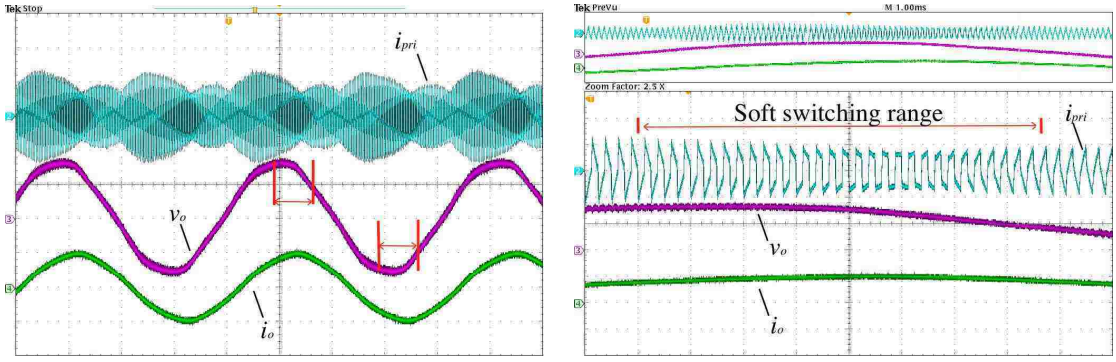

(a) Zoomed-out Waveforms, 4 ms/div. (b) Zoomed-in Waveforms, 400 us/div

Figure 2.14. Soft-switching range under a RL load. From top, i_{pri} (2 A/div), v_o (100 V/div), i_o (2 A/div), 4 ms/div.

discussed in [28] and efficiency measurement was performed by measuring input voltage/current and output voltage/current. The measured results are consistent with the calculated ones. Efficiency is high around rated power because of soft switching. However, efficiency drops significantly when power is less than 30 %. The reasons for low efficiency at light load are: (1) soft switching is not available at light load and (2) the transformer loss becomes more significant at light load. Higher efficiency is necessary to compete with traditional transformers, which requires overall converter design optimization [35] and possibly a new switching strategy [24].

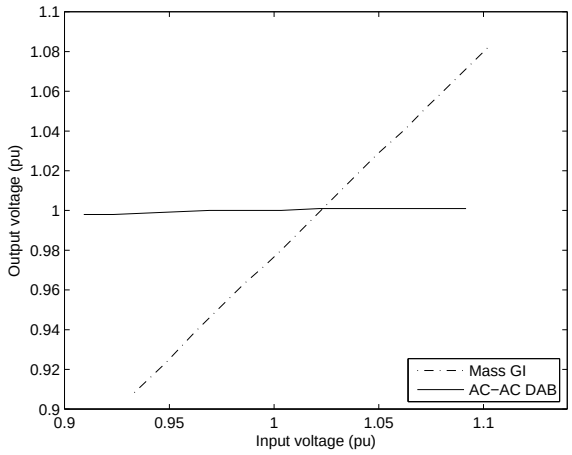

Figure 2.15. Measured output voltages at different input voltages

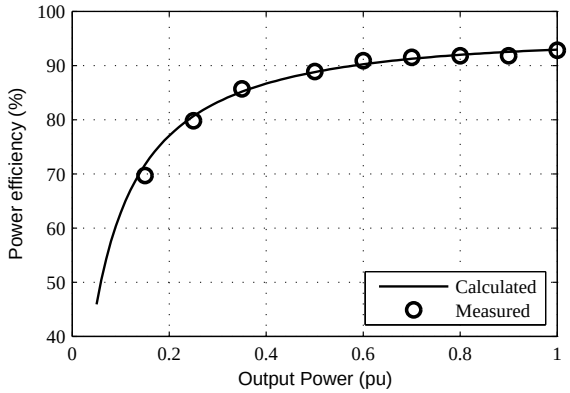

Figure 2.16. Calculated and measured power efficiency

2.9. CONCLUSIONS

This section has analyzed the steady-state operation of DAB converters. High-frequency transformers are used in DAB converters to minimize the bulk of passive components. Four-quadrant switch cells and phase-shift modulation ensure that energy can flow in both directions. Operating modes and soft switching conditions have been analyzed in detail using a generalized per-unit model. Soft switching is valid

over a wide range of load and voltage variations. A design case study is given. Simulation and experiment results confirm that the proposed ac-ac DAB converter can provide direct ac-ac power conversion with soft switching.

This work presents a proof-of-concept study of applying ac-ac DAB converters as SSTs. Several challenges remain for the success of SSTs: (1) the availability of SiC-based high-voltage high-frequency switching device; (2) Hardware optimization and control strategy to improve low power efficiency; and (3) achieving high voltage isolation (input-to-output, phase-to-ground) without significant cost or performance penalties. These will be investigated in future works. Other SST topologies face similar challenges, plus additional difficulties (such as interaction between stages in a multi-stage topology) or expenses (such as high-voltage capacitors).

3. GENERALIZED MODELING OF DAB CONVERTERS

The design of the controller requires a small-signal average model of the DAB converter. There are two approaches to model a DAB converter: (1) a simplified reduced-order continuous-time model neglects the transformer current dynamic [72, 73, 74]; (2) a full-order discrete-time model preserves the dynamic of transformer current [75, 76]. Discrete-time model is one approach to model those converters with large variation and resonant operations [69]. A full-order discrete-time model can obtain higher accuracy at low frequencies than a reduced-order model does [76]. However, a continuous-time model is usually preferred because it provides more physical insight and facilitates control design.

The conventional averaging technique for dc-dc converters requires negligible current ripple [58]. This is not satisfied in DAB converters because transformer current is purely ac. Instead, a generalized averaging technique, which uses more terms in the Fourier series of state variables, is used in the present work [60, 62]. Generalized average modeling has been applied to single-phase ac-dc rectifier [136] and dc-ac resonant inverter system [137]. This section develops a full-order continuous-time state-space average model for dc-dc DAB converters. As compared to the existing reduced-order continuous-time model [72, 73, 74], the proposed model is more accurate at dc and low frequency, and also properly captures effects of capacitor ESR.

This section is organized as follows. Subsection 3.1 describes the operation principles of DAB dc-dc converters as background. Subsection 3.2 presents the development of a full-order continuous-time average model of DAB converters using the generalized averaging approach. Subsection 3.3 discusses the small-signal control-to-output transfer function based on the proposed average model. Subsection 3.4 presents the sufficient conditions of time-scale separation of the dynamics of inductor and capacitor of dc-dc DAB converters. Subsection 3.5 discusses the effect of capacitor equivalent series resistance. Simulation and experimental results are provided in Subsection 3.6. Finally, subsection 3.7 summarizes the contributions of this section.

3.1. DAB DC-DC CONVERTERS

The schematic of a DAB dc-dc converter is given in Figure 3.1. Note that Figure 3.1 is slightly different from Figure 2.1. The reason for such difference is that the model in Figure 3.1 uses a Norton equivalent circuit as its load. Therefore, it can model the effect of bi-directional power flow of dc-dc DAB converters. The high-frequency transformer provides both galvanic isolation and energy storage through its winding leakage inductance. There is a resonant capacitor in parallel with each transistor-diode pair in order to enable soft switching.

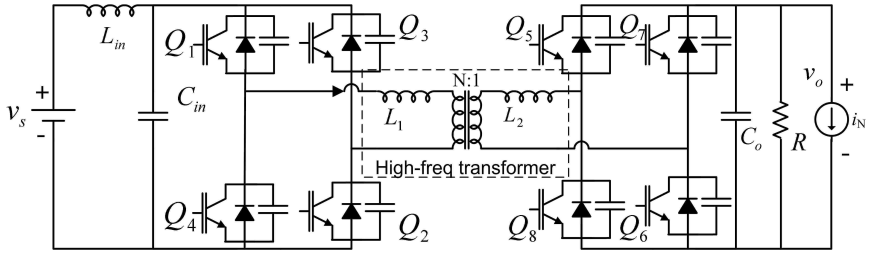

Figure 3.1. DAB converter schematic

A dc-dc DAB converter can be controlled by (1) the phase shift ϕ between two H-bridges, (2) the duty ratios of switching devices, and (3) the switching frequency. For simplicity, this work only analyzes phase shift modulation (PSM) at fixed switching frequency and fixed 50% duty ratio. Power is transferred from the leading bridge to the lagging bridge, which is given by

$$P = \frac{v_s v_o}{2N f_s L_t} d\,(1-d)\,, \tag{40}$$

where N is the turns ratio of the high-frequency transformer, v_s is the input voltage, v_o is the output voltage, phase shift ratio d is equal to $\frac{\phi}{\pi}$, ϕ is the phase shift in radians, f_s is the switching frequency, and $L_t = \frac{L_1}{N^2} + L_2$ is the leakage inductance of the high-frequency transformer, referred to the output side.

3.2. GENERALIZED MODEL OF DAB CONVERTERS

The model is derived by assuming that transformer magnetizing current is not significant, the voltage drop across transistor-diode pairs is negligible, and transistor switching transients are negligible. This subsection uses a simplified circuit schematic (as shown in Figure 3.2).

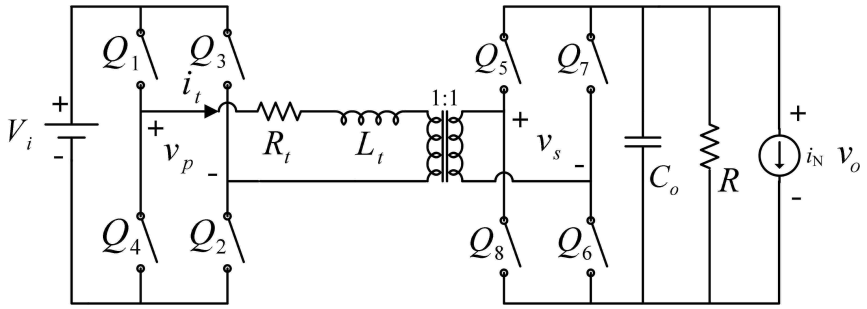

Figure 3.2. Simplified DAB converter schematic

The input capacitance C_{in} is usually relatively large. Therefore, the dynamics of the input capacitor are not considered in this work (Figure 3.2). The current source on the output may be of either polarity for bidirectional power flow. The voltage at the input side is referred to the output side, which is represented as $V_i = \frac{V_s}{N}$. Transformer leakage inductance at both windings is lumped as an equivalent inductance L_t, referred to the output side. Similarly, transistor on-time resistance and transformer winding resistance are lumped as an equivalent resistance R_t (Figure 3.2). Using PSM, the voltage at the transformer input side, v_p, can only have two states: (1) $+V_i$ when transistors Q1 and Q2 are on; (2) $-V_i$ when transistors Q3 and Q4 are on. Therefore,

$$v_p(\tau) = s_1(\tau)v_i(\tau), \tag{41}$$

where the switching function at input bridge, $s_1(\tau)$, is

$$s_1(\tau) = \begin{cases} 1, & 0 \le \tau < \frac{T}{2} \\ -1, & \frac{T}{2} \le \tau < T, \end{cases} \tag{42}$$

where $T = 1/f_s$. Throughout the analysis, τ is used to denote the time within a period, referenced to the rising edge of s_1. Similarly, at output bridge,

$$v_s(\tau) = s_2(\tau) v_o(\tau), \tag{43}$$

and the switching function at output bridge, $s_2(\tau)$, is

$$s_2(\tau) = \begin{cases} 1, & \frac{dT}{2} \le \tau < \frac{T}{2} + \frac{dT}{2} \\ -1, & 0 \le \tau < \frac{dT}{2} \text{ or } \frac{T}{2} + \frac{dT}{2} \le \tau < T. \end{cases} \tag{44}$$

If we select transformer current, i_t, and output capacitor voltage, v_o, as state variables, then the state equations of a DAB converter can be derived as

$$\frac{di_t(\tau)}{d\tau} = -\frac{R_t}{L_t} i_t(\tau) + \frac{s_1(\tau)}{L_t} v_i(\tau) - \frac{s_2(\tau)}{L_t} v_o(\tau), \tag{45}$$

and

$$\frac{dv_o(\tau)}{d\tau} = -\frac{1}{RC_o} v_o(\tau) + \frac{s_2(\tau)}{C_o} i_t(\tau) - \frac{I_N}{C_o}. \tag{46}$$

Equations (45) and (46) are both time-varying and nonlinear. To derive a linear time-invariant model, the next step is to apply averaging. The basic idea of averaging is to represent a state variable, $x(\tau)$, during the interval $t-T \le \tau \le t$, using its Fourier series

$$x(\tau) = \sum_{k=-\infty}^{\infty} \langle x \rangle_k(t) e^{jk\omega_s \tau}, \tag{47}$$

where $\omega_s = 2\pi f_s$, and $\langle x\rangle_k(t)$ is the k^{th} coefficient in the Fourier series

$$\begin{aligned}\langle x\rangle_k(t) &= \frac{1}{T}\int_{t-T}^{t} x(\tau)e^{-jk\omega_s\tau}d\tau. \\ &= \frac{1}{T}\int_{t-T}^{t} x(\tau)\cos k\omega_s\tau d\tau - j\frac{1}{T}\int_{t-T}^{t} x(\tau)\sin k\omega_s\tau d\tau. \end{aligned} \tag{48}$$

This formulation is equivalent to [60] where $\tau = t - T + s$ and $s \in [0, T)$.

Conventional state-space average can be applied when the ripples in state variables are small, which in fact only considers dc terms ($k = 0$) in (47) and (48). However, the transformer current in a DAB converter is purely ac, meaning ripple is large and the dc term is zero. The generalized averaging technique uses more terms in the Fourier series to represent more details in the model. In the case of DAB converters, it is natural to include more terms (both $k = 0$ and $k = \pm 1$) in the Fourier series to represent the averages of state variables.

According to [60, 62], the derivative of the k^{th} coefficient for variable x is

$$\frac{d}{dt}\langle x\rangle_k(t) = \langle\frac{d}{dt}x\rangle_k(t) - jk\omega_s\langle x\rangle_k(t), \tag{49}$$

where $\langle\frac{d}{dt}x\rangle_k$ represents the average of the differential of a state variable in (45) and (46). The k^{th} coefficient of the product of two variables x and y is

$$\langle xy\rangle_k = \sum_{i=-\infty}^{\infty}\langle x\rangle_{k-i}\langle y\rangle_i \tag{50}$$

Consider that the 1^{st} coefficient and the -1^{st} coefficient in Fourier series are complex conjugates, the product of 0^{th} coefficient terms is

$$\langle xy\rangle_0 = \langle x\rangle_0\langle y\rangle_0 + 2\left(\langle x_{1R}\rangle\langle y_{1R}\rangle + \langle x_{1I}\rangle\langle y_{1I}\rangle\right), \tag{51}$$

and the 1^{st} coefficient terms are

$$\langle xy\rangle_{1R} = \langle x\rangle_0\langle y\rangle_{1R} + \langle x\rangle_{1R}\langle y\rangle_0, \tag{52}$$

$$\langle xy\rangle_{1I} = \langle x\rangle_0\langle y\rangle_{1I} + \langle x\rangle_{1I}\langle y\rangle_0, \tag{53}$$

where the subscripts "R" and "I" mean the real and the imaginary parts of a complex number, respectively. The next step is to apply (49) and (51) – (53) to the state-space equations in (45) and (46), the 0^{th} and 1^{st} coefficients of state variables i_t and v_o are

$$\begin{aligned}
\frac{d\langle i_t\rangle_0}{dt} &= -\frac{R_t}{L_t}\langle i_t\rangle_0 + \frac{1}{L_t}\langle s_1\rangle_0\langle v_i\rangle_0 + \frac{2}{L_t}\langle s_1\rangle_{1R}\langle v_i\rangle_{1R} + \frac{2}{L_t}\langle s_1\rangle_{1I}\langle v_i\rangle_{1I} \\
&\quad -\frac{1}{L_t}\langle s_2\rangle_0\langle v_o\rangle_0 + \frac{2}{L_t}\langle s_2\rangle_{1R}\langle v_o\rangle_{1R} + \frac{2}{L_t}\langle s_2\rangle_{1I}\langle v_o\rangle_{1I}, \qquad (54) \\
\frac{d\langle i_t\rangle_{1R}}{dt} &= -\frac{R_t}{L_t}\langle i_t\rangle_{1R} + \omega_s\langle i_t\rangle_{1I} + \frac{1}{L_t}\left(\langle s_1\rangle_0\langle v_i\rangle_{1R} + \langle s_1\rangle_{1R}\langle v_i\rangle_0\right) \\
&\quad -\frac{1}{L_t}\left(\langle s_2\rangle_0\langle v_o\rangle_{1R} + \langle s_2\rangle_{1R}\langle v_o\rangle_0\right), \qquad (55) \\
\frac{d\langle i_t\rangle_{1I}}{dt} &= -\frac{R_t}{L_t}\langle i_t\rangle_{1I} - \omega_s\langle i_t\rangle_{1R} + \frac{1}{L_t}\left(\langle s_1\rangle_0\langle v_i\rangle_{1I} + \langle s_1\rangle_{1I}\langle v_i\rangle_0\right) \\
&\quad -\frac{1}{L_t}\left(\langle s_2\rangle_0\langle v_o\rangle_{1I} + \langle s_2\rangle_{1I}\langle v_o\rangle_0\right), \qquad (56)
\end{aligned}$$

and

$$\begin{aligned}
\frac{d\langle v_o\rangle_0}{dt} &= -\frac{1}{C_o}\langle i_N\rangle_0 - \frac{1}{RC_o}\langle v_o\rangle_0 + \frac{1}{C_o}\langle s_2\rangle_0\langle i_t\rangle_0 \\
&\quad +\frac{2}{C_o}\langle s_2\rangle_{1R}\langle i_t\rangle_{1R} + \frac{2}{C_o}\langle s_2\rangle_{1I}\langle i_t\rangle_{1I}, \qquad (57) \\
\frac{d\langle v_o\rangle_{1R}}{dt} &= -\frac{1}{C_o}\langle i_N\rangle_{1R} - \frac{1}{RC_o}\langle v_o\rangle_{1R} + \omega_s\langle v_o\rangle_{1I} \\
&\quad +\frac{1}{C_o}\langle s_2\rangle_0\langle i_t\rangle_{1R} + \frac{1}{C_o}\langle s_2\rangle_{1R}\langle i_t\rangle_0, \qquad (58) \\
\frac{d\langle v_o\rangle_{1I}}{dt} &= -\frac{1}{C_o}\langle i_N\rangle_{1I} - \frac{1}{RC_o}\langle v_o\rangle_{1I} - \omega_s\langle v_o\rangle_{1R} \\
&\quad +\frac{1}{C_o}\langle s_2\rangle_0\langle i_t\rangle_{1I} + \frac{1}{C_o}\langle s_2\rangle_{1I}\langle i_t\rangle_0. \qquad (59)
\end{aligned}$$

It is assumed that the dynamics of the input voltage and the load is much slower that those of the DAB converter. Therefore, the 0^{th} coefficient of input voltage $\langle v_i\rangle_0 = V_i$, the 1^{st} coefficients of input voltage $\langle v_i\rangle_{1R} = \langle v_i\rangle_{1I} = 0$, the 0^{th} coefficient of load current $\langle i_N\rangle_0 = i_N$, and the 1^{st} coefficient of load current $\langle i_N\rangle_{1R} = \langle i_N\rangle_{1I} = 0$.

Next, it is necessary to find the coefficients of switching functions $s_1(t)$ and $s_2(t)$. Because of the fixed 50% duty ratio, the 0^{th} coefficients of $s_1(t)$ and $s_2(t)$ are

both zero

$$\langle s_1 \rangle_0 = \langle s_2 \rangle_0 = 0. \tag{60}$$

The 1^{st} coefficients of $s_1(t)$ and $s_2(t)$ are

$$\langle s_1 \rangle_{1R} = 0, \tag{61}$$

$$\langle s_1 \rangle_{1I} = -\frac{2}{\pi}, \tag{62}$$

and

$$\langle s_2 \rangle_{1R} = -\frac{2\sin d\pi}{\pi}, \tag{63}$$

$$\langle s_2 \rangle_{1I} = -\frac{2\cos d\pi}{\pi}. \tag{64}$$

Finally, substitute (60) – (64) into (54) – (59), and organize differential equations into matrix representation in (65).

$$\frac{d}{dt}X = AX + Bu, \tag{65}$$

where

$$A = \begin{bmatrix} -\frac{1}{RC_o} & -\frac{4\sin(d\pi)}{\pi C_o} & -\frac{4\cos(d\pi)}{\pi C_o} & 0 & 0 & 0 \\ \frac{2\sin(d\pi)}{\pi L_t} & -\frac{R_t}{L_t} & \omega_s & 0 & 0 & 0 \\ \frac{2\cos(d\pi)}{\pi L_t} & -\omega_s & -\frac{R_t}{L_t} & 0 & 0 & 0 \\ 0 & 0 & 0 & -\frac{R_t}{L_t} & \frac{4\sin(d\pi)}{\pi L_t} & \frac{4\cos(d\pi)}{\pi L_t} \\ 0 & 0 & 0 & -\frac{2\sin(d\pi)}{\pi C_o} & -\frac{1}{RC_o} & \omega_s \\ 0 & 0 & 0 & -\frac{2\cos(d\pi)}{\pi C_o} & -\omega_s & -\frac{1}{RC_o} \end{bmatrix}, \tag{66}$$

$$B = \begin{bmatrix} 0 & 0 & -\frac{2}{\pi L_t} & 0 & 0 & 0 \\ -\frac{1}{C_o} & 0 & 0 & 0 & 0 & 0 \end{bmatrix}^T, \tag{67}$$

$$X = \begin{bmatrix} v_{o0} & i_{t1R} & i_{t1I} & i_{t0} & v_{o1R} & v_{o1I} \end{bmatrix}^T, \tag{68}$$

and

$$u = \begin{bmatrix} V_i & I_N \end{bmatrix}^T . \tag{69}$$

In (65), i_{t0}, v_{o1R}, and v_{o1I} are all zero if their initial values are zero. The dynamics of i_{t0}, v_{o1R}, and v_{o1I} are decoupled from the rest of system. Therefore, the state-space representation in (65) can be equivalently reduced to

$$\begin{aligned} \frac{d}{dt}\begin{bmatrix} v_{o0} \\ i_{t1R} \\ i_{t1I} \end{bmatrix} &= \begin{bmatrix} -\frac{1}{RC_o} & -\frac{4\sin(d\pi)}{\pi C_o} & -\frac{4\cos(d\pi)}{\pi C_o} \\ \frac{2\sin(d\pi)}{\pi L_t} & -\frac{R_t}{L_t} & \omega_s \\ \frac{2\cos(d\pi)}{\pi L_t} & -\omega_s & -\frac{R_t}{L_t} \end{bmatrix} \begin{bmatrix} v_{o0} \\ i_{t1R} \\ i_{t1I} \end{bmatrix} \\ &\quad + \begin{bmatrix} 0 & -\frac{1}{C_o} \\ 0 & 0 \\ -\frac{2}{\pi L_t} & 0 \end{bmatrix} \begin{bmatrix} v_i \\ i_N \end{bmatrix} . \end{aligned} \tag{70}$$

The state equation in (70) indicates that the dynamics of DAB dc-dc converters can be represented using the 0^{th} coefficient of output voltage and the 1^{st} coefficients of transformer current as state variables. If more terms in the Fourier series were used, then the model would be more accurate. However, the resulting model would be too complex to provide insightful information for controller design.

3.3. SMALL-SIGNAL AVERAGE MODEL

Equation (70) is a time-invariant but non-linear system because there are multiplications of state variables. Controller design and stability analysis for a power converter require the derivation of small-signal control-to-output transfer function, which is the dynamic response of a converter from a small perturbation in the control signal. In (70), when there is a small perturbation in d, the state variables v_{o0}, i_{t1R}, and i_{t1I} will deviate from their steady states. Assume that the input voltage is constant, capital variables represent steady states, lower case variables represent large-signal states, and Δ variables represent small-signal states. Define the deviations of state variables as

$$\begin{aligned} \Delta d &= d - D, && (71)\\ \Delta v_{o0} &= v_{o0} - V_{o0}, && (72)\\ \Delta i_{t1R} &= i_{t1R} - I_{t1R}, && (73)\\ \Delta i_{t1I} &= i_{t1I} - I_{t1I}. && (74) \end{aligned}$$

Equation (70) contains multiplication of control input and state variables. For small Δd, the nonlinear term $\sin(\pi d)\, v_{o0}$ is approximated by using (71) – (74)

$$\begin{aligned} \sin(\pi d)\, v_{o0} &= \sin(\pi D)\, \Delta v_{o0} + V_{o0} \sin(\pi D) \cos(\pi \Delta d) \\ &\quad + V_{o0} \cos(\pi D) \sin(\pi \Delta d) \\ &= \sin(\pi D)\, \Delta v_{o0} + V_{o0} \sin(\pi D) \\ &\quad + V_{o0} \cos(\pi D)\, (\pi \Delta d)\,. \end{aligned} \tag{75}$$

Other non-linear terms are approximated in a similar way.

Steady state values of v_{o0}, i_{t1R}, and i_{t1I} can be found from (70) by solving

$$\frac{d}{dt} \begin{bmatrix} v_{o0} & i_{t1R} & i_{t1I} \end{bmatrix}^T = 0. \tag{76}$$

Substituting (71) – (76) into (70), the small-signal model of the DAB converter is given in (77), which is time-invariant linear system in state-space representation. Equation (77) can be used to calculate the control-to-output transfer function of DAB converters.

$$\begin{aligned} \frac{d}{dt} \begin{bmatrix} \Delta v_{o0} \\ \Delta i_{t1R} \\ \Delta i_{t1I} \end{bmatrix} &= \begin{bmatrix} -\frac{1}{RC_o} & -\frac{4\sin(D\pi)}{\pi C_o} & -\frac{4\cos(D\pi)}{\pi C_o} \\ \frac{2\sin(D\pi)}{\pi L_t} & -\frac{R_t}{L_t} & \omega_s \\ \frac{2\cos(D\pi)}{\pi L_t} & -\omega_s & -\frac{R_t}{L_t} \end{bmatrix} \begin{bmatrix} \Delta v_{o0} \\ \Delta i_{t1R} \\ \Delta i_{t1I} \end{bmatrix} \\ &\quad + \begin{bmatrix} \frac{4}{C_o} \left(I_{0I} \sin(\pi D) - I_{0R} \cos(\pi D) \right) \\ \frac{2V_{o0}}{L_t} \cos(\pi D) \\ -\frac{2V_{o0}}{L_t} \sin(\pi D) \end{bmatrix} \Delta d. \end{aligned} \tag{77}$$

3.4. SINGULAR PERTURBATION ANALYSIS

Singular perturbation analysis focuses on the time-scale separation of state variables in a dynamic system. It separates the "fast" dynamics from the "slow" dynamics. If a system is singularly perturbed, then its state variables can be separated into slow variables ,x, and fast variables, z. When studying the fast variables, x can be approximated as constants; when studying the slow variables, z can be approximated using algebraic expressions. A detailed description of singular perturbation analysis can be found in [77].

To perform singular perturbation analysis, the dynamic system must be converted into a normalized form. As in [19], let nominal output voltage be V_0 and the nominal current be $I_0 = V_0/R$. Then Eq. (70) can be normalized by

$$\hat{v_o} = \frac{v_o}{V_0} \tag{78}$$

$$\hat{i_t} = \frac{i_t}{I_0} \tag{79}$$

$$\hat{v_i} = \frac{v_i}{V_0} \tag{80}$$

$$\hat{t} = \frac{t}{RC_o} \tag{81}$$

$$\epsilon = \frac{L_t}{R^2 C_o}. \tag{82}$$

The normalized average system is

$$\frac{dx}{dt} = f(x,z) = -x + 2Uz, \tag{83}$$

$$\epsilon\frac{dz}{dt} = g(x,z) = b\hat{v_i} - U^T x - \delta z, \tag{84}$$

where, x $= \hat{v}_{o0}$, $z = \begin{bmatrix}\hat{i}_{1R} & \hat{i}_{1I}\end{bmatrix}^T$, $U = \begin{bmatrix}-\frac{2\sin(d\pi)}{\pi} & -\frac{2\cos(d\pi)}{\pi}\end{bmatrix}$, $\delta = \begin{bmatrix}-\frac{R_t}{R} & \frac{X_t}{R} \\ -\frac{X_t}{R} & -\frac{R_t}{R}\end{bmatrix}$, $b = \begin{bmatrix}0 & -\frac{2}{\pi}\end{bmatrix}^T$, and $X_t = \omega_s L_t$ is transformer leakage reactance.

The first step of singular perturbation analysis is to find zero-order term of the integral manifold of g. By solving $g(x, \varphi_0) = 0$ for φ_0,

$$\begin{aligned} \varphi_0 &= \delta^{-1}\left[b\hat{v}_i - U^T x\right] \\ &= \frac{2R}{\pi\left(R_t^2 + X_t^2\right)}\begin{bmatrix} -X_t\hat{v}_i + X_t x\cos\left(d\pi\right) + R_t x\sin\left(d\pi\right) \\ -R_t\hat{v}_i + R_t x\cos\left(d\pi\right) - X_t x\sin\left(d\pi\right) \end{bmatrix}. \end{aligned} \tag{85}$$

The first-order term φ_1 is

$$\begin{aligned} \varphi_1 &= \left(\frac{\partial g}{\partial z}\right)^{-1}\left(\frac{\partial \varphi_0}{\partial x}\right)^{-1} f\left(x, \varphi_0\right) \\ &= \mathcal{K}\begin{bmatrix} 2R_t X_t\cos\left(\pi d\right) + \left(R_t^2 - X_t^2\right)\sin\left(\pi d\right) \\ -2R_t X_t\sin\left(\pi d\right) + \left(R_t^2 - X_t^2\right)\cos\left(\pi d\right) \end{bmatrix}, \end{aligned} \tag{86}$$

where $\mathcal{K} = \frac{2R^2\left(x\left(8RR_t + \pi^2\left(R_t^2 + X_t^2\right)\right) - 8R\hat{v}_i\left(R_t\cos(\pi d) + X_t\sin(\pi d)\right)\right)}{\pi^3\left(R_t^2 + X_t^2\right)^3}$.

Next, the off-manifold dynamic of z is

$$\epsilon\frac{d\eta}{dt} = g\left(x, \varphi_0 + \epsilon\varphi_1 + \eta\right) - \epsilon\left(\frac{\partial \varphi_0}{\partial x}\right) f\left(x, \varphi_0 + \eta\right). \tag{87}$$

Substitute (83) and (84) into (85) – (87), the state equation of off-manifold dynamic is

$$\epsilon\frac{d\eta}{d\hat{t}} = \left(-\delta + \frac{N}{D}\Gamma\right)\eta, \tag{88}$$

where $N = 8R^2\epsilon\left(X_t\cos\left(d\pi\right) + R_t\sin\left(d\pi\right)\right)$, $D = \pi^2 R\left(R_t^2 + X_t^2\right)$, and $\Gamma = \begin{bmatrix} \sin\left(d\pi\right) & \cos\left(d\pi\right) \\ \sin\left(d\pi\right) & \cos\left(d\pi\right) \end{bmatrix}$.

The sufficient condition for time-scale separation is that the fast variables converge to their quasi-steady-state quickly, which means the off-manifold dynamic in (88) converges to zero. Therefore, the condition for convergence is that the eigenvalues of state matrix in (88) have a negative real part. The eigenvalues of (88) are

$$\lambda = \frac{1}{D}\mathcal{R} \pm \sqrt{\mathcal{I}}, \tag{89}$$

where

$$\mathcal{R} = -\pi^2 R_t \left(R_t^2 + X_t^2\right) + 4R^2 R_t \epsilon \tag{90}$$

and

$$\mathcal{I} = -\pi^4 X_t^2 \left(R_t^2 + X_t^2\right)^2 - 8\pi^2 R^2 X_t^2 \left(R_t^2 + X_t^2\right) \epsilon + 16 R^4 R_t^2 \epsilon^2. \tag{91}$$

If we define $Q = X_t/R_t$ and assume that $Q > 1$, then

$$\begin{aligned} \mathcal{I} &= -\pi^4 Q^2 \left(1+Q^2\right)^2 R_t^6 - 8\pi^2 Q^2 \left(1+Q^2\right) R_t^4 \frac{L_t}{C_o} + 16 R_t^2 \frac{L_t^2}{C_o^2} \\ &< \left(\sqrt{2} R_t \frac{L_t}{C_o}\right)^2 - \left(\pi^2 R_t^3 + 4 R_t \frac{L_t}{C_o}\right)^2 \\ &< 0. \end{aligned} \tag{92}$$

Equation (92) indicates that the eigenvalues of (88) are complex conjugates. Therefore, the condition that the eigenvalues in (88) have negative real part is

$$\mathcal{R} = 4 R_t \frac{L_t}{C_o} - \pi^2 R_t \left(R_t^2 + X_t^2\right) < 0. \tag{93}$$

Defining $\alpha = \sqrt{\frac{1+Q^2}{Q^2}}$, the condition in (93) becomes

$$f_c = \frac{1}{2\pi\sqrt{L_t C_o}} < \frac{\pi}{2} \alpha f_s. \tag{94}$$

Equation (94) is a sufficient condition that the dynamics of transformer current and output voltage are separated.

3.5. EFFECT OF CAPACITOR EQUIVALENT SERIES RESISTANCE

The average model in the previous subsections does not consider the effect of output capacitor equivalent series resistance (ESR). This subsection discusses the influence of ESR on the generalized average model of DAB converters. When ESR is

considered, the state space equations of DAB converters in (45) and (46) are

$$\frac{di_t(t)}{dt} = -\frac{R_t}{L_t}i_t(t) - \frac{s_2}{L_t}\frac{R_cR}{R_c+R} + \frac{s_1(t)}{L_t}v_i(t) - \frac{s_2(t)}{L_t}\frac{R}{R_c+R}v_o(t), \tag{95}$$

$$\frac{dv_c(t)}{dt} = -\frac{1}{(R+R_c)\,C_o}v_o(t) + \frac{s_2(t)}{C_o}\frac{R}{R_c+R}i_t(t) - \frac{1}{C_o}I_N(t), \tag{96}$$

and

$$v_o(t) = \frac{R}{R_c+R}v_c(t) + s_2\frac{R_cR}{R_c+R}i_t(t) - \frac{R_cR}{R_c+R}I_N(t), \tag{97}$$

in which capacitor voltage v_c is different from output voltage v_o in this case.

In (95), (96), and (97), the same generalized averaging technique described in (51) – (53) can also be applied. Therefore, the 0-index and 1-index of state variables are given in (98) (shown in the bottom),

$$\frac{d}{dt}X = A_{esr}X + Bu, \tag{98}$$

where

$$A_{esr} = \begin{bmatrix} -\frac{1}{(R+R_c)C_o} & -\frac{4K_1\sin(d\pi)}{\pi C_o} & -\frac{4K_1\cos(d\pi)}{\pi C_o} & 0 & 0 & 0 \\ \frac{2K_1\sin(d\pi)}{\pi L_t} & -\frac{R_t}{L_t} & \omega_s & \frac{2K_2\sin(d\pi)}{\pi L_t} & 0 & 0 \\ \frac{2K_1\cos(d\pi)}{\pi L_t} & -\omega_s & -\frac{R_t}{L_t} & \frac{2K_2\cos(d\pi)}{\pi L_t} & 0 & 0 \\ 0 & \frac{4K_2\sin(d\pi)}{\pi L_t} & \frac{4K_2\cos(d\pi)}{\pi L_t} & -\frac{R_t}{L_t} & \frac{4K_1\sin(d\pi)}{\pi L_t} & \frac{4K_1\cos(d\pi)}{\pi L_t} \\ 0 & 0 & 0 & -\frac{2K_1\sin(d\pi)}{\pi C_o} & -\frac{1}{(R+R_c)C_o} & \omega_s \\ 0 & 0 & 0 & -\frac{2K_1\cos(d\pi)}{\pi C_o} & -\omega_s & -\frac{1}{(R+R_c)C_o} \end{bmatrix}, \tag{99}$$

$K_1 = \frac{R}{R_c+R}$, and $K_2 = \frac{R_cR}{R_c+R}$. The definition of B, X, and u are the same as in (65). Comparing (98) and (65), it is obvious that the dynamics of all six state variables are now coupled. As a result, it is impossible to reduce (98) into a third-order system. Small-signal perturbation can be applied to (98) as well to derive a control-to-output transfer function. The procedure is the same and it is not repeated here.

3.6. SIMULATION AND EXPERIMENT RESULTS

Simulation and experiment results are provided in order to verify the proposed average model. A time-domain switching model has been developed in PLECS. An experiment setup has been built. The main parameters for the power stage of simulation model and experimental prototype are given in Table 3.1. Switching devices are IGBT STGF19NC60HD from STMicroelectronics, rated at 19 A, 600 V. The switching frequency of IGBTs is 10 kHz. A high-frequency transformer is made up of a UU-100 ferrite core from Ferroxcube. Both primary and secondary windings consist of 40 turns and each turn is made up of four AWG 18 magnetic wires. Series inductors are added on both windings to form the necessary winding inductance for the proper operation of the DAB converter prototype. Two 350V 270μF aluminium electrolytic capacitors are connected in parallel to form the output capacitor. A 4.7 nF ceramic capacitors is connected in parallel with each IGBT to reduce switching loss. This DAB converter prototype is controlled using a 32-bit floating-point micro-processor TMS320F28335 from Texas Instruments. A picture of the experimental prototype is shown in Figure 3.3.

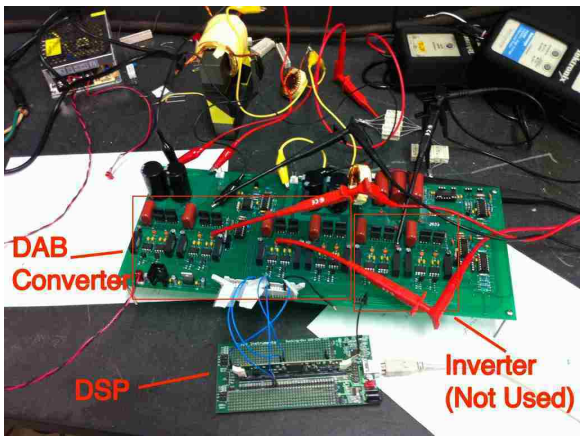

Figure 3.3. Experimental Prototype of DC-DC DAB Converter

Table 3.1. Circuit Parameters

Leakage Inductance	250 μH
Winding Resistance	0.4 Ω
Resonant Capacitor	4.7 nF
Output Filter Capacitor	540 μF
Switch Frequency	10 kHz
Switching Device	STGF19NC60HD
Load Resistor	35 Ω
Capacitor ESR	0.8Ω

The control-to-output transfer function is a metric for small-signal average model of power converters. Three averaging techniques are compared:

1. Reduced-order continuous-time model derived from steady-state transformer current [72, 73];

2. Full-order discrete-time model [75, 76];

3. The proposed full-order continuous-time model.

The test conditions are: the input voltage is 100 V, and the voltage transfer ratio is set to 1; the load resistance at the output side is set to 38 Ω, and output power is 260 W. The control-to-output transfer function of a DAB dc-dc converter was measured using a varying frequency sinusoidal signal superimposed on a steady-state duty ratio. The procedure to measure control-to-output transfer function is described as follows (Figure 3.4). In controller software, a function generator generated a sinusoidal perturbation signal at frequency f_{pert}, which is specified as an input. The perturbation signal was superimposed on steady-state duty ratio. The superimposed duty ratio was fed into the on-chip PWM generator to control the switching devices in the power stage of DAB converter. The magnitude of perturbation signal, $d_{i,pert}$, was set to 0.01 when f_{pert} was less than 512 Hz and 0.02 when f_{pert} was larger than 512 Hz. The output voltage of DAB converter was measured and recorded using a Tektronix MSO-4054 oscilloscope. Measured data were imported and processed in

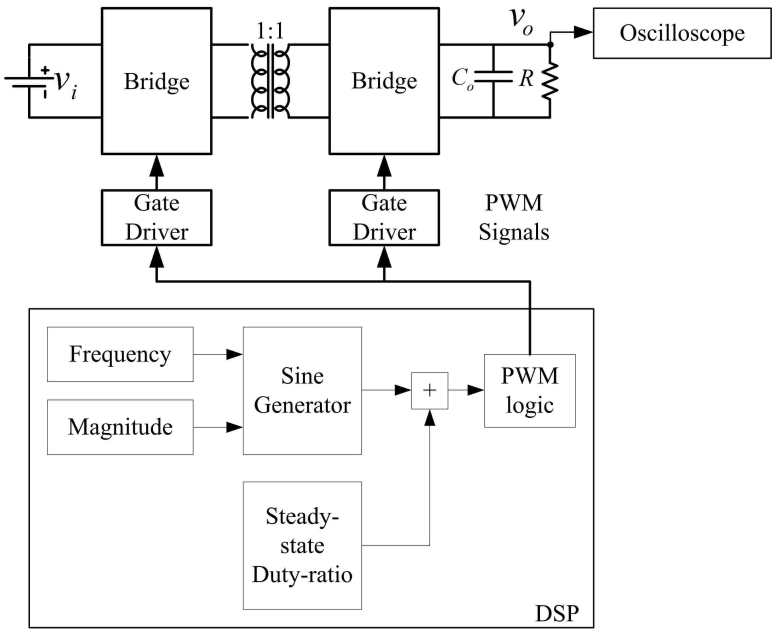

Figure 3.4. Diagram to measure control-to-output transfer function

MATLAB. The magnitude of the output voltage perturbation, v_{pert}, at $f_{o,pert}$ was extracted by FFT analysis. Therefore, control-to-output gain at f_{pert} is given by

$$Gain = 20\log_{10}\left(\frac{v_{o,pert}}{d_{i,pert}}\right), \tag{100}$$

where $d_{i,pert} = 0.01$ when $f_{pert} < 512$Hz and $d_{i,pert} = 0.02$ when $f_{pert} > 512$Hz.

The small-signal control-to-output gains of the three previously mentioned models are plotted in Figure 3.5 and Figure 3.6. The obtained results from the PLECS simulation and the hardware experiment show a very good match between calculated and measured transfer functions. Figure 3.5 shows the models without considering ESR. There are some mismatches between the reduced-order continuous-time model and the measured results at low frequencies. On the other hand, both the discrete-time model and the proposed full-order continuous-time model provide more accurate results than does the reduced-order model at low frequency. The proposed approach obtains similar accuracy as the discrete-time model does. However, the proposed approach provides a continuous-time model, which is easy to manipulate and more convenient for controller design.

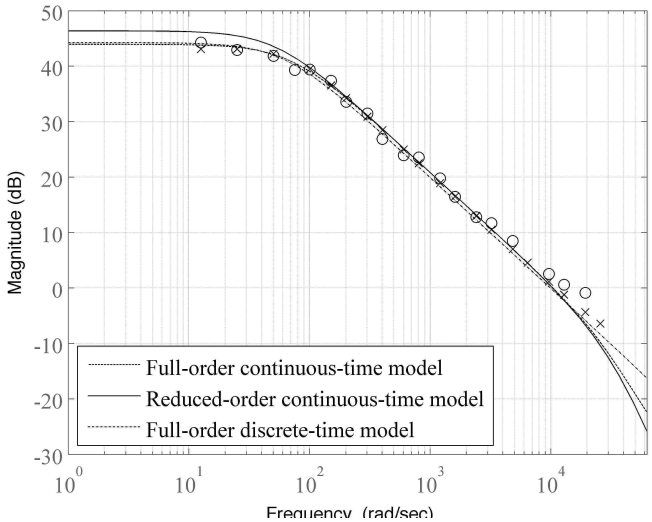

Figure 3.5. Without ESR. Calculated and measured control-to-output gain. Dashed line: proposed full-order continuous-time model; solid line: reduced-order continuous-time model; dash-dot line: full-order discrete-time model; crosses: results from detailed switching simulation; and circles: results from hardware measurement. All gains are measured in dB.

The effect of ESR becomes significant at the frequency where $1/\omega C_o$ is equal to R_c, which is 1180 Hz for the capacitors used in this experimental prototype. Figure 3.6 shows the models with ESR considered. The reduced-order average model fails to predict the control-to-output gain at high frequency. The higher-order average model in (98) provide more accurate match than the third-order model in (65) does. Figure 3.6 also indicates a trade-off between model complexity and model accuracy. A simpler, third-order model is preferred if the effect of ESR can be ignored, while a complex, higher order model is necessary in the case that ESR must be considered.

With the values in Table 3.1, $Q = \frac{2\pi f L_t}{R_t} = 30$, $\alpha = 1.006$, $f_c = 434\text{Hz} < \frac{\pi \alpha f_s}{2} = 15994\text{Hz}$ in (94), meaning the DAB dc-dc converter prototype does meet the time-scale separation condition. A duty ratio step change, from 0.19 to 0.22, was applied. Output voltage and transformer current are shown in Figure 3.7(a) for the simulation and in Figure 3.7(b) for the experiment. Classic first-order behavior can be observed, which indicates that the dynamics of voltage and current are decoupled.

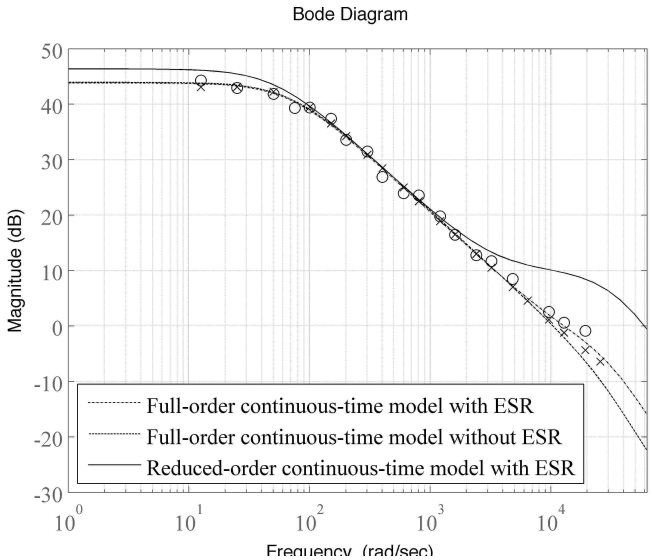

Figure 3.6. With ESR. Calculated and measured control-to-output gain. Dashed line: proposed full-order continuous-time model; solid line: reduced-order continuous-time model; dash-dot line: full-order discrete-time model; crosses: results from detailed switching simulation; and circles: results from hardware measurement. All gains are measured in dB.

3.7. CONCLUSIONS

A novel average modeling approach for a phase-shift controlled bidirectional dc-dc DAB converter is presented in this section. The proposed method, which uses switching frequency terms in the Fourier series of state variables, captures the effects of purely ac transformer current on converter dynamics. The proposed model is compared with the previously presented modeling methods. Both simulation and experimental results show that the proposed model provides more accurate frequency-domain control-to-output gain. In particular, the proposed model is more accurate at dc and low frequency than the reduced-order models in [72, 73, 74]. The proposed average model for DAB converter is in continuous-time domain and is insightful and friendly to controller design. The effect of capacitor ESR is considered when the 0^{th} and 1^{st} coefficients of both transformer current and output capacitor voltage are kept. A higher-order model is able to obtain more accurate predictions at the cost

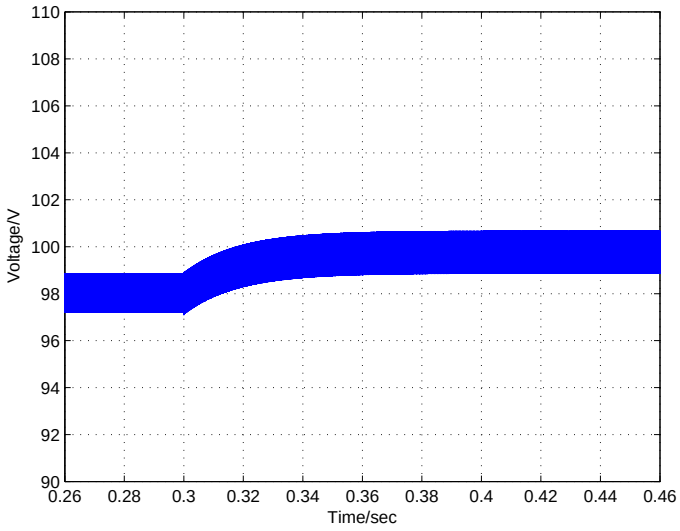

(a) Simulation.

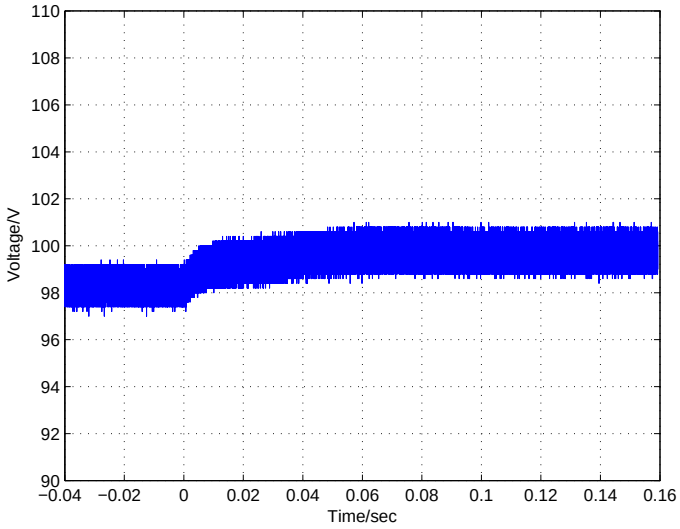

(b) Experiment.

Figure 3.7. Duty ratio step change of the designed DAB converter, Output voltage (V).

of complexity. Singular perturbation analysis is performed based on the proposed full-order continuous-time average model. The sufficient condition for state variable time-scale separation, output voltage as slow dynamic and transformer current as fast dynamic, is derived and verified by both simulation and experiment results.

4. CONTROL OF DAB CONVERTERS DRIVING INVERTERS

The multi-stage ac-dc-ac-dc-ac configuration (as shown as SST2 in Figure 1.2 or SST3 in Figure 1.3) is one of many feasible SST topologies [1, 2, 3]. In a multi-stage configuration of single-phase SSTs (Figure 1.2 or Figure 1.3), the output voltage and the output current of the inverter stage are 60 Hz grid frequency, while the input and output voltages of the DAB converter stage are dc. As a result, the instantaneous output power fluctuates at 120 Hz and there is significant second order harmonic current at the input side of the inverter stage. Therefore, when a dc-dc DAB converter is driving such an inverter, it is common to select an adequately large output capacitor bank to absorb the 120 Hz harmonic current and to minimize the output voltage ripple. Because the second order harmonic frequency is relatively low, this might result in large capacitor bank at the output side of the DAB converter, which increases cost, weight, and volume. Furthermore, large electrolytic capacitors are one major factor affecting the reliability of power converters.

One way to reduce the output capacitor bank is to enable dc-dc DAB converters with the ability to process power at 120 Hz. As a result, both average power and 120 Hz power are processed by rectifier, DAB converter, and inverter, from the grid to the load. How dose a DAB converter track a second order reference? The control bandwidth at 120 Hz is limited because the switching frequency of DAB converters is constrained by the availability of power devices [3]. When a conventional PI controller is used, it only achieves infinite gain at dc, making it difficult to track and to obtain zero steady-state error at 120 Hz, resulting in high voltage ripple at the output of DAB converters.

This section addresses such limitations of a conventional PI controller for a dc-dc DAB converter driving a single-phase dc-ac inverter. Two methods are proposed to solve this issue. The first one adds an additional feedforward path to a conventional PI controller. The second method uses a Proportional-Integral-Resonant (PI-R) controller, which achieves high gain at 120 Hz. The section is organized as follows. Subsection 4.1 discusses the model approximation in this study. Subsection 4.2 uses the average models of DAB converters to discuss the limitation of conventional PI

controllers. Subsection 4.3 presents two solutions: (1) an additional feedforward path to conventional PI controller and (2) a novel PI-R controller. It studies the dynamics in frequency domain to show the advantages of a PI-R controller for DAB converters. Subsection 4.4 presents the simulation and experimental results to verify the proposed control strategy. Subsection 4.5 summaries the contrition of this section.

4.1. SYSTEM CONFIGURATION AND APPROXIMATION

Without loss of generality, this section lumps the paralleled rectifiers and DAB converters into one rectifier and one DAB converter, respectively. The schematic of a single-phase SST is shown in Figure 4.1. The first stage is a single-phase active front-end rectifier, which converts the grid ac voltage to dc voltage. The second stage is an isolated dc-dc DAB converter, which transfers power from its input dc bus to its output dc bus by a high-frequency transformer. The last stage is a single-phase dc-ac inverter, which generates an ac sinusoidal voltage as the SST's output voltage.

The conventional power flow diagram of a multi-stage SST is given in Figure 4.2. Ideally, the voltage and current at both the input of rectifier and the output of inverter are 60 Hz. Therefore, the input power of rectifier and the output power of inverter consist mainly of average power (which is in dc) and ripple power (which is the second order harmonic content in 120 Hz).

$$P = \sqrt{2}V\sin(\omega_s t)\sqrt{2}I\sin(\omega_s t) = VI\left(1+\cos\left(2\omega_s t\right)\right), \tag{101}$$

where V represents input/output RMS voltage, I represents input/output RMS current, $\omega_s = 2\pi f_s$, and $f_s = 60$ Hz is the grid frequency. On the other hand, the conventional control method for a dc-dc DAB converter can only process dc power. This means that the two dc buses must absorb the 120 Hz ripple power, as visualized in Figure 4.2 (solid lines represent dc power while dash lines represent 120 Hz ripple power). Because 120 Hz is relatively low (second order harmonic), large bus capacitance is needed to reduce the bus voltage fluctuation.

The novel power flow diagram of a multi-stage SST is given in Figure 4.3. Once the DAB converter is capable of processing power at 120 Hz, both average power and 120 Hz ripple power are transferred from the input port to the output port, which

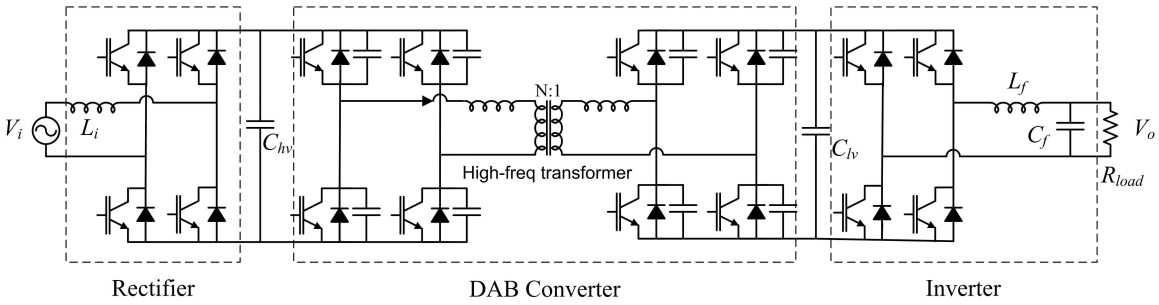

Figure 4.1. Circuit Configuration of Multi-stage SSTs

Figure 4.2. Conventional Power Flow of Multi-stage SSTs

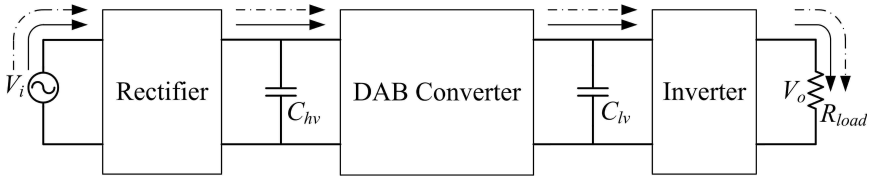

Figure 4.3. Novel Power Flow of Multi-stage SSTs

reduces the requirement for the capacitance on the two dc buses. This is advantageous because less capacitance means lower component cost and higher reliability.

The first step of controller design for a given plant is to find the model of the plant itself. The circuit in Figure 4.1 contains three power converters. There are six state variables. It is difficult and tedious to develop a sixth-order state-space averaging model. The order of such a model could be even higher if the closed-loop controllers of these three converters are also included. What is more, it is not insightful to analyze a high-order state-space model. Therefore, it is necessary to do some simplification and approximation based on some reasonable assumptions.

Since the focus of the present work is on the DAB converters in SSTs, the following assumptions are made: (1) the rectifier stage has been well designed to provide a stable input dc voltage for the DAB stage; (2) the inverter stage has been well designed to provide a 120 V sinusoidal output voltage at 60 Hz; and (3) the switching frequency of the inverter is higher than that of the DAB converter and the switching frequencies of all converter stages are much higher than the grid frequency. In this study, the switching frequencies of the DAB converter and the inverter are set to 5 kHz and 20 kHz, respectively. Because the DAB input voltage is much higher than the inverter input voltage for an SST at the distribution level [1], lower switching frequency of the DAB converter is required.

Using the first assumption above, the active front-end rectifier is replaced by a constant voltage source. Simplification can also be applied to the inverter using the second and the third assumptions. Assuming that the output voltage and the load current of the inverter are both sinusoidal and that the voltage ripple at the low-voltage dc bus is relatively small, the input current of inverter can be approximated by

$$i_{inv,in} = \frac{P_{avg}\left(1+\cos\left(2\omega_s t\right)\right)}{V_{dc}}, \tag{102}$$

where P_{avg} is average output power and V_{dc} is the average output voltage of the DAB converter (also the input voltage of the inverter). Then the input admittance of the inverter is

$$Y_{inv,in} = \frac{i_{inv,in}}{V_{dc}} = \frac{P_{avg}\left(1+\cos\left(2\omega_s t\right)\right)}{V_{dc}^2} = Y_{dc} + Y_{ac}, \tag{103}$$

where $Y_{dc} = Y_0 = \frac{P_{avg}}{V_{dc}^2}$ and $Y_{ac} = Y_0 \cos\left(2\omega_s t\right)$. The input admittance given in (103) represents the equivalent inverter model looking from its input side, at the frequency range well below switching frequency.

As mentioned before, the switching frequency of the DAB converter is lower than that of the inverter because of limited device switching performance. The input current of inverter contains mainly dc and second order harmonic contents. Furthermore, the switching frequencies of both DAB converter and inverter (5 kHz and

20 kHz, respectively) are significantly higher than the grid frequency and its second order harmonic frequency (60 Hz and 120 Hz, respectively). Therefore, the quasi-steady-state inverter model is valid and the input admittance of the inverter varies in the frequency of 120 Hz. Therefore, the inverter, as the load of DAB converter, is modeled as a variable resistor consisting of two parts, one in dc and one varying in 120 Hz. The simplified system schematic is shown in Figure 4.4.

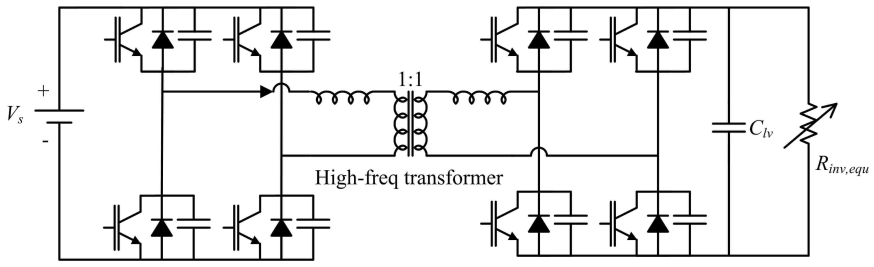

Figure 4.4. Simplified schematic of a DAB converter driving an inverter

4.2. MODEL ANALYSIS

After the approximation, the problem becomes how to model a dc-dc DAB converter. Instead of using the simplified reduced-order continuous-time model in [72, 73, 74] or the full-order discrete-time model in [75, 76], this present work uses the full-order continuous-time model based on generalized average modeling technique, which is discussed in Section 3. The proposed model is able to provide more accurate control-to-output transfer function. For convenience, the small-signal control-to-output transfer function given in (77) is repeated below in the matrix form.

$$\frac{d}{dt}x = Ax + B\Delta d, \tag{104}$$

$$y = Cx, \tag{105}$$

where

$$x = \begin{bmatrix} \Delta v_{o0} & \Delta i_{t1R} & \Delta i_{t1I} \end{bmatrix}^T, \tag{106}$$

$$y = \begin{bmatrix} \Delta v_{o0} \end{bmatrix}, \tag{107}$$

$$A = \begin{bmatrix} -\frac{1}{RC_o} & -\frac{4\sin(D\pi)}{\pi C_o} & -\frac{4\cos(D\pi)}{\pi C_o} \\ \frac{2\sin(D\pi)}{\pi L_t} & -\frac{R_t}{L_t} & \omega_s \\ \frac{2\cos(D\pi)}{\pi L_t} & -\omega_s & -\frac{R_t}{L_t} \end{bmatrix}, \tag{108}$$

$$B = \begin{bmatrix} \frac{4}{C_o}\left(I_{0I}\sin(\pi D) - I_{0R}\cos(\pi D)\right) \\ \frac{2V_{o0}}{L_t}\cos(\pi D) \\ -\frac{2V_{o0}}{L_t}\sin(\pi D) \end{bmatrix}, \tag{109}$$

and

$$C = \begin{bmatrix} 1 & 0 & 0 \end{bmatrix}^T \tag{110}$$

In (104), (105), (106), (107), (108), (109) and (110), v_{o0} is the output voltage of DAB converter; i_{1R} and i_{1I} are the real part and imaginary part of the transformer current of DAB converter, respectively; $R = \frac{1}{Y_{dc}+Y_{ac}}$ is equivalent input impedance of the inverter; C_o is the output capacitance of DAB converter; L_t is the transformer leakage inductance of DAB converter; R_t is the lumped equivalent series resistance of transformer windings; $\omega_s = 2\pi f_s$ and $f_s = 5000$Hz is the switching frequency of DAB converter; and d is the phase-shift ratio between the two bridges of DAB converter. Variables in captial letters represent nominal values while those in lower case letters represent small-signal variables.

The control-to-output transfer function of a DAB converter is given by

$$G_{vd}(s) = C\left(sI - A\right)^{-1} B. \tag{111}$$

Given the circuit parameters described in Table 4.1, Table 4.2 and Table 4.3, Figure 4.5 shows the control-to-output transfer function of a DAB converter driving a variable inverter-equivalent load. The plots show the transfer functions when the instantaneous power of the inverter is 1.0 pu, 1.5 pu, 1.732 pu, 2 pu, 0.732 pu, 0.5 pu, and 0 pu (corresponding to the power phase angle of 0, $\frac{\pi}{6}$, $\frac{\pi}{3}$, $\frac{\pi}{2}$, $\frac{7\pi}{6}$, $\frac{4\pi}{3}$, and $\frac{3\pi}{2}$, respectively). This transfer function shows how the low frequency gain of a DAB converter changes as its equivalent load resistance varies, which is the result of the 2nd-order

Table 4.1. Circuit Parameters of DAB Converter

Inductance, input side	500 μH
Inductance, LV	500 μH
Switch Frequency	5 kHz
ZVS Capacitor	2.7 nF
Output Capacitor	200 μF
Switching Device	ST STD8NM60ND 600V 7.3A MOSFET

Table 4.2. Transformer Design of DAB Converter

Core Type	Ferrite ETD 54
Core Area	3.55 cm^2
Window Area	3.16 cm^2
Area Product	8.85 cm^4
wire, input side	108 turns AWG 20
wire, output side	108 turns AWG 20
MMF Layout	Input: 3 portions, 1 layer/portion Output: 3 portions, 1 layer/portion

Table 4.3. Circuit Parameters of Inverter

Filter inductance	300 μH
Filter capacitance	30 μF
Switch Frequency	20 kHz
Rated Load Resistance	36 Ω
Switching Device	ST STGD3HF60HD 600V 7A IGBT

fluctuating power caused by the inverter. It also shows that the pole dependence on the load admittance Y_{ac}.

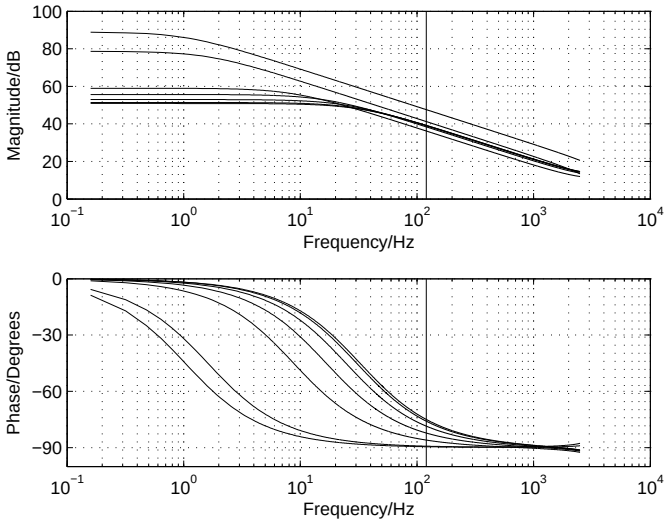

Figure 4.5. Variation of DAB Control-to-Output Transfer Function caused by Inverter (Vertical line marks 120 Hz).

According to Section 2, the power transferred by a DAB converter is given by

$$P = \frac{v_s v_o}{2 f_s L_t} d\,(1-d)\,, \tag{112}$$

and v_s is the input voltage. Given a specified power rating, a range of preferred phase-shift ratio d, and a specific range of soft switching, the product of transformer leakage inductance L_t and switching frequency f_S is fixed. Therefore, increase of f_s would result in decrease of L_t, canceling the effect of increasing switching frequency. The dc-dc DAB converter, whose parameters are listed in Table 4.1, satisfies the condition of dynamics decoupling, according to the result of singular perturbation analysis in Section 3. Therefore, the gain and phase of the transfer function in (111) at low frequency are mainly determined by the dynamic characteristics of the slower state variable, which is the capacitor voltage. This phenomenon leads to the conclusion that switching frequency has insignificant effect on the low-frequency dynamic response of a dc-dc DAB converter.

Such effect is visualized in Figure 4.6. It shows the transfer function in (111) under different sets of parameters. The curves with rated parameters (those given in Table 4.1) match the curves with f_s doubled (and with L_t reduced by half). The curves

with C_o quadrupled illustrates that the dominant pole of (111) is largely determined by the DAB converter's output capacitance C_o.

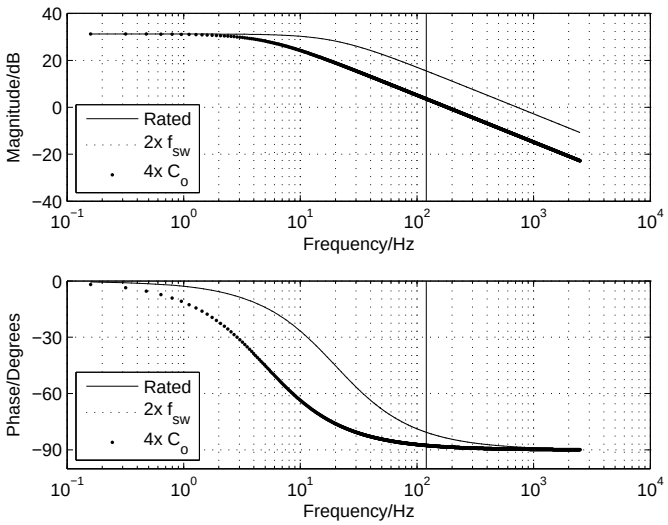

Figure 4.6. Bode Plot of DAB Control-to-Output Transfer Function caused by Different Parameters (Vertical line marks 120 Hz).

For a well designed inverter, there is significant 120 Hz harmonic current at the input side of inverter. This harmonic current poses a design challenge to the DAB converter, caused by limited control bandwidth of DAB converter. Figure 4.7 shows the small-signal schematic of a closed loop feedback control system that consists of a DAB converter and a PI controller (as shown in Figure 4.8). Note that a delay term e^{sT_d} is added to the feedback loop in Figure 4.7 to represent the sampling and processing delay T_d, which is caused by the digital implementation of the control algorithm and modulation processes.

Since the DAB converter has one dominant pole according to Figure 4.5, a single PI controller seems a candidate solution because of simplicity. Figure 4.8 shows the structure of a PI controller. Figure 4.9 shows the bode plot of the loop gain of a dc-dc DAB converter with a PI controller. The gain around 120 Hz (753 rad/s) is low, which indicates that it is difficult to track and compensate the disturbance caused by the 120 Hz harmonic current from inverter. One possible solution is to increase

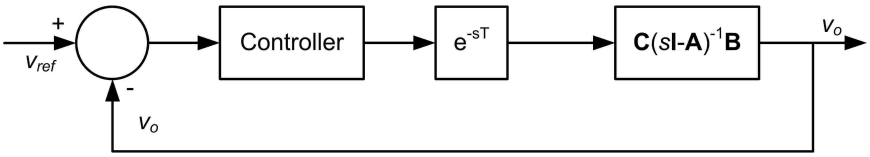

Figure 4.7. Small-Signal Schematic of Closed-loop Controlled DAB Converter

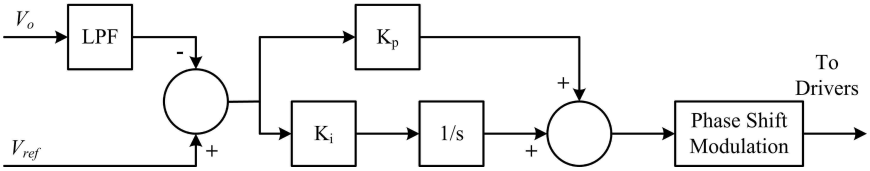

Figure 4.8. Diagram of PI-only control

the gain (K_p) of the PI controller. However, as shown in Figure 4.10, a high gain PI controller would decrease phase margin and might even destabilize the control loop. A larger output capacitor is preferred in order to increase phase margin and improve stability, which, however, results in lower gain at 120 Hz and cancels the effect of increasing controller gain.

As discussed above, a PI controller is not the optimal control solution for a DAB converter driving an inverter because of low gain around 120 Hz. Two improvements over PI-only control will be introduced.

4.3. TWO PROPOSED SOLUTIONS

The control target of a DAB converter driving an inverter consists of two parts: (1) regulate output dc voltage and control the average output power and (2) suppress the 120 Hz disturbance from the inverter and track the 120 Hz ripple power. As discussed before, PI-only control can only meet the first target and fails to meet the second target. Two methods are proposed to address the control challenge caused by low gain at 120 Hz of the feedback loop with only a PI controller. The first method adds a feedforward path to the existing PI controller, while the second one uses an additional resonant controller to form a PI-R control. These two methods will be discussed in detail as follows.

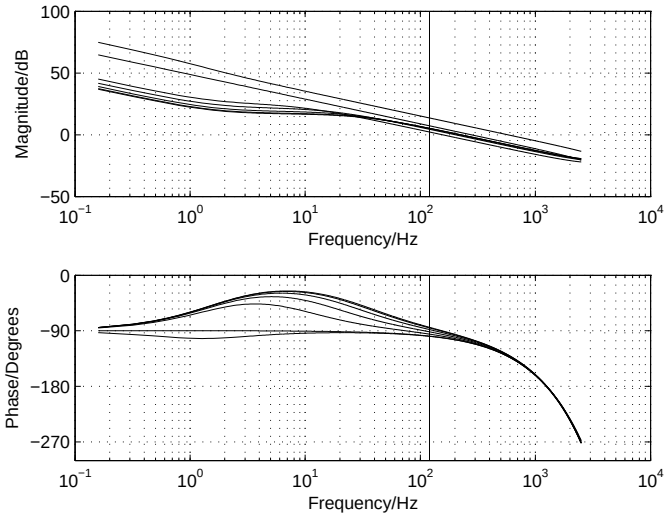

Figure 4.9. Bode Plot of PI-only Method (Vertical line marks 120 Hz).

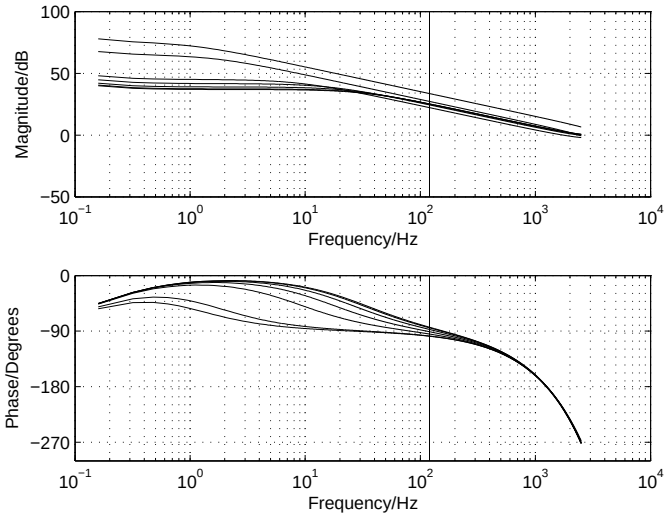

Figure 4.10. Bode Plot of PI-only Method with higher gain (Vertical line marks 120 Hz).

4.3.1. Method 1: PI Plus Feedforward Control. The first method is a PI controller assisted by an additional direct feedforward portion. Figure 4.11 shows the schematic of the proposed control method. In Figure 4.11, the PI controller only takes care of the first control target: output dc voltage, while the feedforward portion is responsible for tracking the 120 Hz fluctuating power.

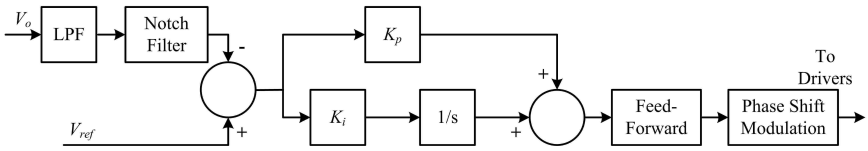

Figure 4.11. Diagram of PI plus Feedforward control

After sampling the output voltage of the DAB converter, instead of using an anti-aliasing filter, this method uses a low-pass filter (LPF) whose passband is below 120 Hz. As a result, the 120 Hz content in the sampled signal is suppressed by the LPF. The feedback signal fed into the PI controller is essentially dc. Therefore, the PI controller shown in Figure 4.11 is called the dc regulator. Because the LPF has a low cut-off frequency and the PI controller only regulates dc voltage, the bandwidth of the PI controller does not need to be high and it is called low-bandwidth PI controller.

The feedforward portion is introduced in order to track the 120 Hz ripple power generated by the inverter. In this study, the inverter and the DAB converter share a single DSP unit as controller. The phase angle of inverter's output voltage is set by the controller of inverter. Therefore, such phase angle is also known to the controller of the DAB converter. From (101), the power angle in a 120 Hz cycle can be calculated from the output voltage's phase angle

$$\theta_p = 2\theta_v - \frac{\pi}{2}. \tag{113}$$

The sinusoidal feedforward signal in (113) is at 120 Hz and is used to compensate the 2nd order harmonic content.

Although the above solution is able to track the 120 Hz power by inverter, the analysis and parameter selection is not straightforward. Also, if the load power factor is non-unity, the feedforward term may not properly track the output power ripple. Therefore, a closed-loop controller combining a PI controller with a resonant controller is introduced next.

4.3.2. Method 2: PI-R Control. To compensate for the 120 Hz power fluctuation, it is vitally important that the feedback compensator has high gain around that frequency. Increasing the gain of the PI controller might meet this goal, but

at the expense of reduced phase margin. The present work develops a new compensator based on the PI-resonant (PI-R) scheme, in which the PI portion regulates the dc output voltage and the resonant portion directly compensates the 120 Hz ripple voltage. The schematic diagram of the proposed controller is shown in Figure 4.12. Such controller, instead of using any feedforward from the inverter, adds an additional resonant controller (R controller) in parallel with the existing PI controller.

An R controller is known for its equivalence to a PI controller in the synchronously rotating reference frames [83, 84, 85, 81]. It is able to obtain zero steady-state error for a sinusoidal reference single without coordinate transformation. The transfer function of R-controller is

$$G_{PR}(s) = K_r \frac{2s}{s^2 + \omega_2^2}, \tag{114}$$

where $\omega_2 = 2\pi \times 120$ rad/s represents the 2nd order harmonic frequency of grid frequency. The R controller has added two poles at 120 Hz and helped obtaining high gain in the loop gain around that frequency. Combining a PI controller with an R controller, the transfer function of the regulator is

$$G_{PIR}(s) = K_p + K_i \frac{1}{s} + K_r \frac{2s}{s^2 + \omega_2^2}. \tag{115}$$

The idea of this method is: the PI controller achieves high gain at dc while the R controller achieves high gain at the second order harmonic frequency. Therefore, both the error at dc and the one at 120 Hz are attenuated.

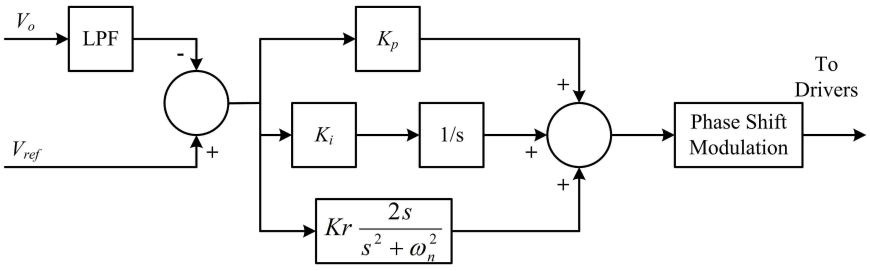

Figure 4.12. Diagram of PI-R control

If output voltage reference v_{ref} is considered as reference and inverter input current i_{inv} is considered as disturbance, the output voltage v_o in the frequency domain can be expressed as

$$v_o(s) = v_{ref}(s) \cdot G_1(s) + i_{inv} \cdot G_2(s), \tag{116}$$

where

$$G_1(s) = \frac{G_{PIR}(s) \cdot G_{vd}(s)}{1 + G_{PIR}(s) \cdot G_{vd}(s)}, \tag{117}$$

$$G_2(s) = \frac{\frac{1}{sC_o}}{1 + G_{PIR}(s) \cdot G_{vd}(s)}, \tag{118}$$

and $v_{ref}(s)$, $i_{inv}(s)$ and $v_o(s)$ are variables v_{ref}, i_{inv} and v_o in Laplace domain.

In (116), $v_{ref}(s)$ is dc while $i_{inv}(s)$ contains mainly dc and second order harmonic contents generated by inverter. Therefore, the steady-state value of (116) is

$$v_o = v_{ref} \cdot 1 + i_{inv} \cdot 0 = v_{ref}, \tag{119}$$

if $K_i \cdot K_p \cdot K_r \neq 0$, because

$$\lim_{s \to 0} G_{PIR}(s) = +\infty \tag{120}$$

and

$$\lim_{s \to \omega_2} G_{PIR}(s) = +\infty. \tag{121}$$

Equation (119) means that ideally, the proposed PI-R control can obtain zero steady-state error.

The Bode plot of loop gain using PI-R controller is shown in Figure 4.13. The loop gain has the high gain at dc and around 120 Hz. The R controller only affects the loop gain around 120 Hz, besides which the loop gain is very similar the one shown in Figure 4.9. This is an advantage of the proposed control scheme. The PI controller and the R controller can be designed separately, the first one for dc regulation and the second one for 120 Hz harmonic regulations. This means that the closed-loop

feedback system with the PI-R control provides good regulation of output voltage at dc and at 120 Hz.

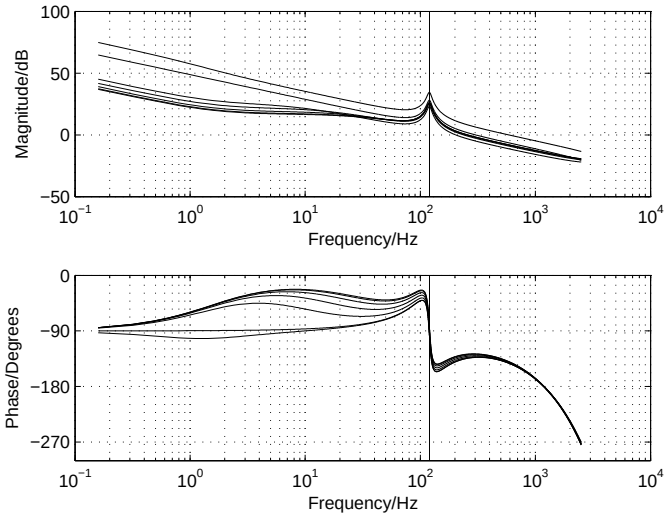

Figure 4.13. Bode Plot of PI-R Method (Vertical line marks 120 Hz).

The effect of adding an R controller to the existing PI controller can also be analyzed using the impedance approach. The small-signal output impedance of the DAB converter is expressed as the transfer function from the output current of the DAB converter to its output voltage,

$$Z_o = \frac{\frac{1}{sC_o}}{1 + G_{PIR}(s) \cdot G_{vd}(s)}. \tag{122}$$

Figure 4.14 and 4.15 show the bode plot of the DAB converter's output impedance with PI-only control and PI-R control, respectively. When using the PI-R control scheme, the DAB converter has lower output impedance around 120 Hz than the one using PI-only control. This means that lower voltage ripple will be caused by the same 120 Hz ripple current when the proposed PI-R control is used.

4.3.3. Implementation in Digital Processor. To implement the proposed control schemes digitally in a low-cost Texas Instruments floating-point DSP

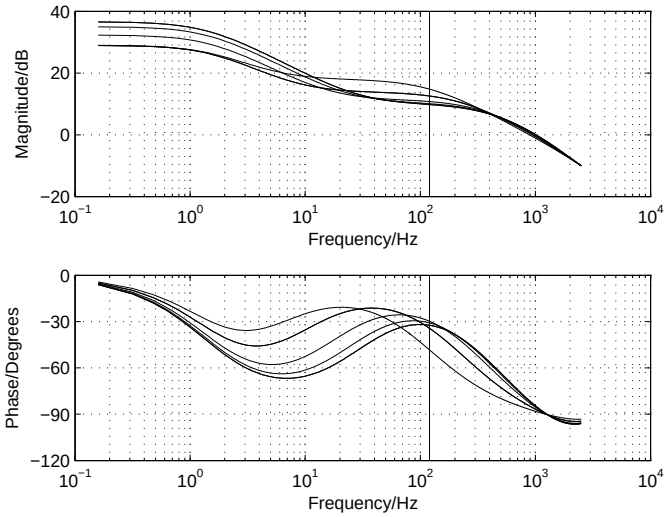

Figure 4.14. Output Impedance with PI-only control (Vertical line marks 120 Hz).

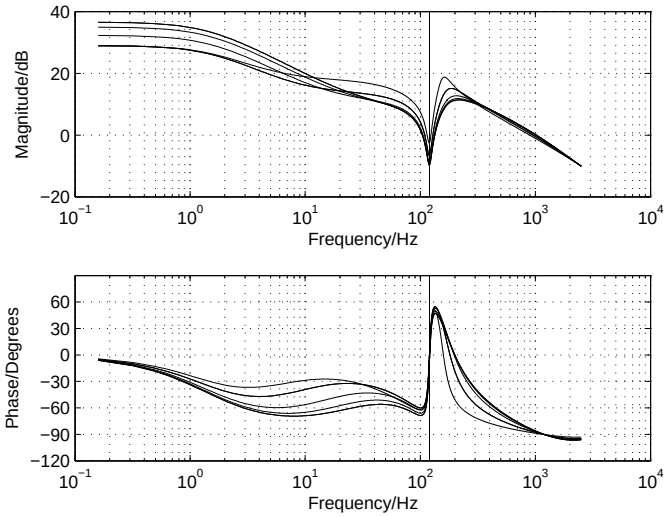

Figure 4.15. Output Impedance with PI-R control (Vertical line marks 120 Hz).

TMS320F28335 processor, the continuous-time domain transfer functions of controllers and filters have to be digitized using an appropriate discrete-time conversion method.

Discretization is a process transferring continuous-time domain differential equations into discrete-time domain difference equations. Zero-order hold (ZOH) and

bilinear transformation (also known as Tustin transformation) are two well-known methods [138]. The ZOH method is simple but it introduces delay that is disadvantageous because phase lag distorts frequency response and might destabilize the control loop. The Tustin transformation preserves the stability of the continuous-time transfer functions, which means that the digitalized system is always stable if the original system is stable. Therefore, the present work uses the Tustin transformation, is given by:

$$s = \frac{2}{T}\frac{z-1}{z+1}, \tag{123}$$

where T is the sample time, s and z mean the operators of Laplace transformation and Z-transformation, respectively.

Given a general 2nd order continuous-time transfer function

$$G(s) = \frac{b_0 s^2 + b_1 s + b_2}{a_0 s^2 + a_1 s + a_2}. \tag{124}$$

Substitutue (123) into (124), the discretization of (124) is

$$G(z) = \frac{\beta_0 s^2 + \beta_1 s + \beta_2}{\alpha_0 s^2 + \alpha_1 s + \alpha_2}, \tag{125}$$

where $\beta_0 = 4b_0 + 2b_1T + b_2T^2$, $\beta_1 = -8b_0 + 2b_2T^2$, $\beta_2 = 4b_0 - 2b_1T + b_2T^2$, $\alpha_0 = 4a_0 + 2a_1T + a_2T^2$, $\alpha_1 = -8a_0 + 2a_2T^2$, and $\alpha_2 = 4a_0 - 2a_1T + a_2T^2$.

Using (125), the parameters of digitalized controller transfer functions of $K_p = 0.01$, $K_i = 0.1$, $K_r = 0.12$, and $T = 200$ μsec are listed in Table 4.4. Using the same method in (125), the parameters for the anti-aliasing filter (for PI-only and PI-R control, sampling frequency 5 kHz, passband frequency 1.0 kHz, stopband gain -40 dB) and the LPF (for PI-Feedforward control, sampling frequency 5 kHz, passband frquency 32 Hz, stopband gain -40 dB) are given in Table 4.5.

4.4. SIMULATION AND EXPERIMENTAL RESULTS

Several PLECS simulations have been run to demonstrate the effectiveness of the proposed controllers when a DAB converter is driving an inverter. System parameters are given in Tables 4.1 – 4.5. Simulation results of all three methods, PI-only,

Table 4.4. Parameters of Controllers

	β_0	β_1	β_2	α_0	α_1	α_2
PI Controller	0	0.02002	-0.01998	0	1	-1
R Controller	0.00062	0	-0.00062	1	-1.965	0.9876

Table 4.5. Parameters of Digital Filters

	0	1	2	3	4	5
LPF $f_{pass} = 1kHz$, β_i	0.754	0.2331	0.3821	0.3821	0.2331	0.754
LPF $f_{pass} = 1kHz$, α_i	1	-0.3873	0.7755	-0.0959	-0.0891	0.000307
LPF $f_{pass} = 32Hz$, β_i	0.000151	0.00106	0.00318	0.00318	0.00106	0.000151
LPF $f_{pass} = 32Hz$, α_i	1	-3.9274	7.0375	-1.8829	0.4271	-0.0424

PI plus feedforward control, and PI-R control, are given in the following figures. Four simulation cases are compared: PI-only with rated bus capacitance (in Figure 4.16(a)), PI-only with four times larger bus capacitance (in Figure 4.16(b)), PI with Feedforward with rated bus capacitance (in Figure 4.16(c)), and PI-R control with rated bus capacitance (in Figure 4.16(d)).

Figure 4.16(a) shows the results when using PI-only control. With just the PI controller, the ripple at 120 Hz is high. Voltage ripple is observed to be approximately 20 V peak-to-peak at 120 Hz. Comparing the middle waveform with the lower waveform in Figure 4.16(a), the duty ratio of the DAB converter is lagging the inverter output power (the lower waveform), which is the result of low loop gain and high output impedance of the DAB converter at 120 Hz.

Figure 4.16(b) shows the results when using PI-only control and increasing the bus capacitance by a factor of four. The results show reduction of output voltage ripple. This can be confirmed by the decrease of output impedance caused by larger capacitance. On the other hand, there is even more lag between the duty ratio of DAB converter and the inverter output power, which is confirmed by reduced loop gain when output capacitance is increased.

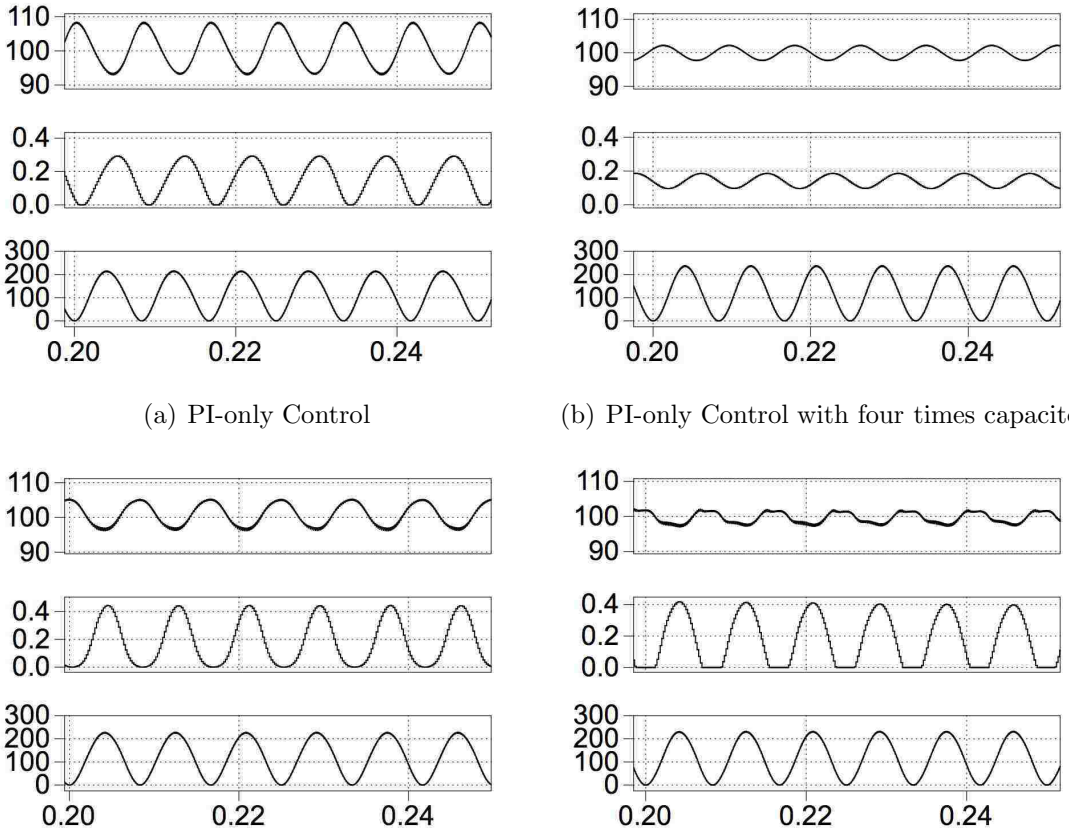

(a) PI-only Control

(b) PI-only Control with four times capacitor

(c) PI-Feedforward Control

(d) PI-R Control

Figure 4.16. Simulation Results. From top to bottom: output voltage of DAB converter (V), duty ratio of DAB converter, output power of inverter (W)

Figure 4.16(c) shows the results when using PI-Feedforward control at rated output capacitance. The duty ratio of the DAB converter is in phase with the inverter output power. This means that with the help of information from feedforward, the DAB converter is able to track the power demanded by the inverter. Therefore, output voltage ripple is reduced without increasing output capacitance.

Figure 4.16(d) shows the results when using PI-R control at rated output capacitance. With an additional R controller, the duty ratio of the DAB converter is in phase with the inverter output power, which is similar to the one using feedforward control. This is the result of high gain at 120 Hz and low output impedance of the DAB converter generated by adding the R controller to the loop gain. Therefore, Figure 4.16(d) shows similar reduction of voltage ripple.

Figure 4.17 shows the diagram of experimental setup. Output voltage of the DAB converter is sampled by an operational amplifier circuit and the on-chip analog-to-digital converter of TI TMS320F28335 DSP. Low-pass filters are used as an anti-alias filter for digital implementation of controllers. Feedback control algorithms, configurable to be PI-only, PI-Feedforward, or PI-R control, are programmed in the interrupt service routine (ISR) of the DSP chip. The outputs of the feedback controller are fed to the on-chip PWM generator. The PWM signals are sent to gate drivers to turn-on/turn-off the power IGBTs. Figure 4.18 shows a picture of the experiment setup, which consists of a DAB converter circuit board, an inverter circuit board, and a DSP control circuit board. Experimental results are given in Figure 4.19(a) – Figure 4.19(d).

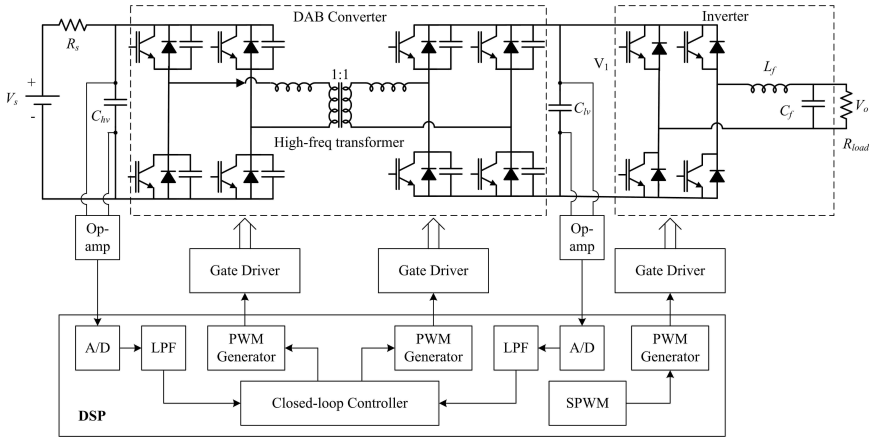

Figure 4.17. Experimental Hardware Diagram

Figure 4.19(a) and 4.19(b) show the experimental results of using the PI-only control scheme, when the output capacitance of the DAB converter is set to 200μF (the rated value) and to 800μF (four times of the rated value). The larger capacitor bank, which reduces the output impedance of a DAB converter, obviously reduces the ripple in DAB converter's output voltage (channel 2) caused by the 120 Hz current by the single-phase inverter. The transformer current of the DAB converter (channel 4) also indicates how high the loop-gain is at 120 Hz and how the feedback controller

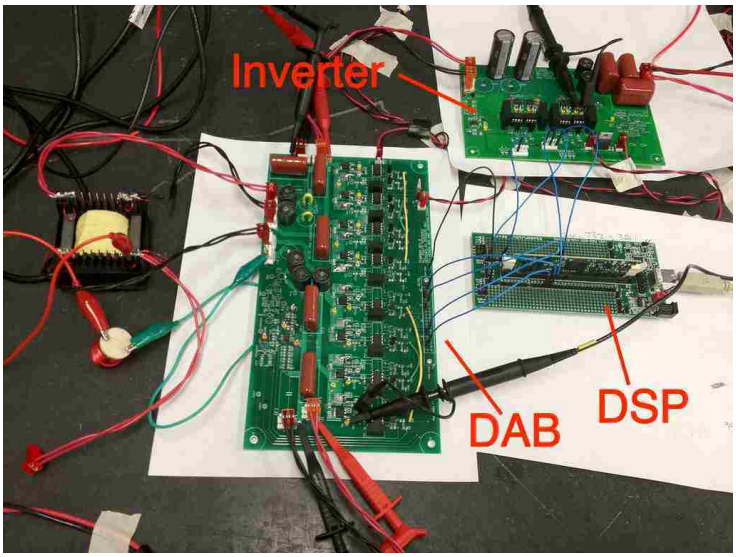

Figure 4.18. Picture of Experimental Hardware

tracks the error at 120 Hz. When the phase-shift ratio of a DAB converter tracks the output power ripple cause the down-string inverter, there would be a 120 Hz envelop in the resulting transformer current. Comparing the waveforms of channel 4 (the green one) in Figure 4.19(a) and Figure 4.19(b), the 120 Hz envelope is more observable for the first case. For the same controller parameters, high output capacitance slows down the feedback loop. The reason for low voltage ripple at the dc bus is simply that a larger capacitor can absorb more ripple current.

Figure 4.19(c) shows the experimental results of using the PI-Feedforward control scheme. Voltage ripple reduces comparing to Figure 4.19(a). However, contrary to the case in Figure 4.19(b), this is achieved not by increasing output capacitance, but by providing the DAB converter with the ability to track 120 Hz ripple power. Such ability is indicated by the 120 Hz envelope of the transformer current. When output voltage of inverter approaches its peak (either positive peak or negative peak), the instantaneous power is also approaching its peak. As a result, the DAB converter supplies higher current to its load, the inverter. On the other hand, when output voltage of the inverter is crossing zero, the instantaneous power is approaching zero. Therefore, the DAB converter also supply near-zero current. This confirms that the DAB converter has the ability to track 120 Hz ripple power, enabled by feedforward.

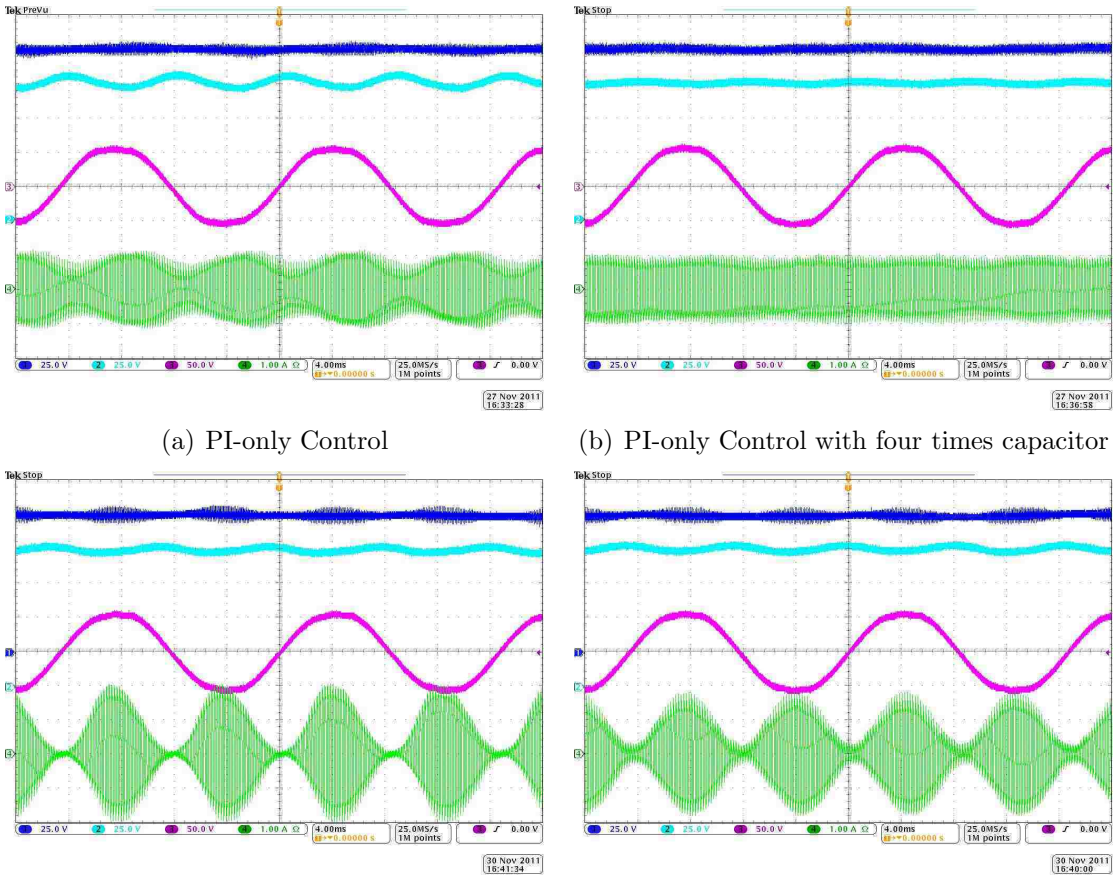

(a) PI-only Control

(b) PI-only Control with four times capacitor

(c) PI-Feedforward Control

(d) PI-R Control

Figure 4.19. Experimental Results. From top to bottom: Input Voltage of DAB Converter (V), Output Voltage of DAB Converter (V), Output Voltage of Inverter (V), Transformer Current of DAB Converter (A). 4ms/div.

Figure 4.19(d) shows the experimental results of using the PI-R control scheme. Similar to Figure 4.19(c), lower voltage ripple is observed without using larger capacitor. The 120 Hz envelope of the transformer current also confirms the the ability to track second order ripple power. However, such ability is not enabled by feedforward. It is given by adding an additional R controller.

4.5. SUMMARY

In the multi-stage configuration of an SST, a dc-dc DAB converter drives a single-phase dc-ac inverter. The cascaded connection of power converters poses a challenge to closed-loop controller design. A single-phase inverter has significant

second order (120 Hz) harmonic current in its input side. A conventional PI controller has limited bandwidth at 120 Hz because of the relatively low switching frequency of the DAB converter. What is more, simply increasing switching frequency would not result in higher bandwidth. Two control methods are proposed to solve the above challenge without using large dc bus capacitor between the DAB converter and the inverter. The first method uses the feedforward information from the inverter, while the second method adds an R controller to the feedback loop. Bode plot analysis of the loop gain and the closed-loop output impedance of DAB converters is used to study the limitation of PI controller and the effect of adding an R controller. Simulation and experimental results confirm the effectiveness of the proposed methods.

5. SUMMARY AND CONCLUSIONS

The objective of this dissertation is to analyze three different aspects of DAB converters and to provide a set of tools to help design DAB converters for SST applications. DAB converters have some specific characteristics, which require new analysis approaches, new modeling techniques, and new control schemes. This dissertation presents three contributions.

Different SST topologies have their own advantages and disadvantages. Some have more functionalities and complicated circuits, while some others lack reactive power control but have a simpler circuit. The proposed ac-ac DAB converter is an alternative SST topology when only active power control is required. While the conventional SST topology uses a multi-stage configuration, the ac-ac DAB converter is a single-stage converter that is able to provide regulated voltage step-up/step-down as a utility transformer. The proposed topology uses the nonzero transformer leakage inductance to facilitate voltage regulation and soft-switching. Four-quadrant switch cells and phase-shift modulation ensure that energy can flow in both directions. This work presents a proof-of-concept study of applying ac-ac DAB converters as SSTs.

Average models of DAB converters are necessary for the analysis and design of DAB converters. Most previously published papers have assumed that the dynamics of DAB converters can be approximated by a reduced-order model. The reason for such approximation is the pure ac transformer current of DAB converter, which is difficult to model using the conventional averaging technique. This dissertation provides a full-order continuous-time model for DAB converters by using the generalized state-space averaging technique. It uses more terms in the Fourier Series of a state variable, leading to a third-order model if capacitor ESR is not considered and a sixth-order model if ESR is considered. Experimental results show improved accuracy of the proposed modeling approach. The proposed average model, singular perturbation analysis provides a formal analysis of the conditions of separating the fast dynamic variable from the the slow ones. Designers of SSTs can use the new model to obtain an average model that is a better match to real hardware.

In the multi-stage configuration of SSTs, a dc-dc DAB converter is in between the rectifier stage and the inverter stage. Since both the rectifier and the inverter process ac power. It is useful to enable the DAB converter with such ability so that both average power and ripple power can be transferred in a streamline. This dissertation provides two methods for dc-dc DAB converters to track the 120 Hz power demand by the inverter stage. The first method uses the feedforward information from the inverter, while the second method adds an R controller to the feedback loop. The later method is preferred because its effect on the feedback loop can be analyzed using classic frequency domain design tool such as the Bode plot.

5.1. FUTURE WORK

The ac-ac DAB converter is modular in nature and can be expanded easily to a multiphase configuration. The input-series-output-parallel circuit configuration can block high voltage on the primary side and share large current on the secondary side [78, 72, 139]. It is feasible to use three modules with 6.5 kV IGBTs to implement a single-phase 7.2 kV/120 V 20 kVA distribution-level transformer (Figure 5.1). The proposed modular configuration can also be applied for three-phase applications (Figure 5.2) in future work. For both cases, a shunt active power filter would be needed to provide reactive power compensation to ensure that only active power is transferred through the SST.

The proposed average model of dc-dc DAB converters can be integrated with average models of ac-dc rectifiers and dc-ac inverters to build a average model of an SST. Future work could use the SST average model as a building block to model a large smart grid (similar to the IEEE 34 bus distribution system [140]) with a number of SSTs. A large system of interconnected power electronic converters might have some interesting complex or chaotic behaviors that are worth analysis before actual hardware deployment.

The next step in the analysis of a dc-dc DAB converter driving a dc-ac inverter could be adding closed-loop control the inverter. When two regulated converters are in a cascaded connection, the well-known negative impedance effect might be a challenge for controller design. The conventional rule-of-thumb is to use a large dc bus capacitor, not only to absorb the 120 Hz harmonic current, but also to minimize the

de-stabilizing effect caused by the regulated load converter. An appropriate approach to model the input impedance of a regulated inverter is necessary for such study. Future work could also focus on the development of a nonlinear control scheme to address the previously mentioned effects.

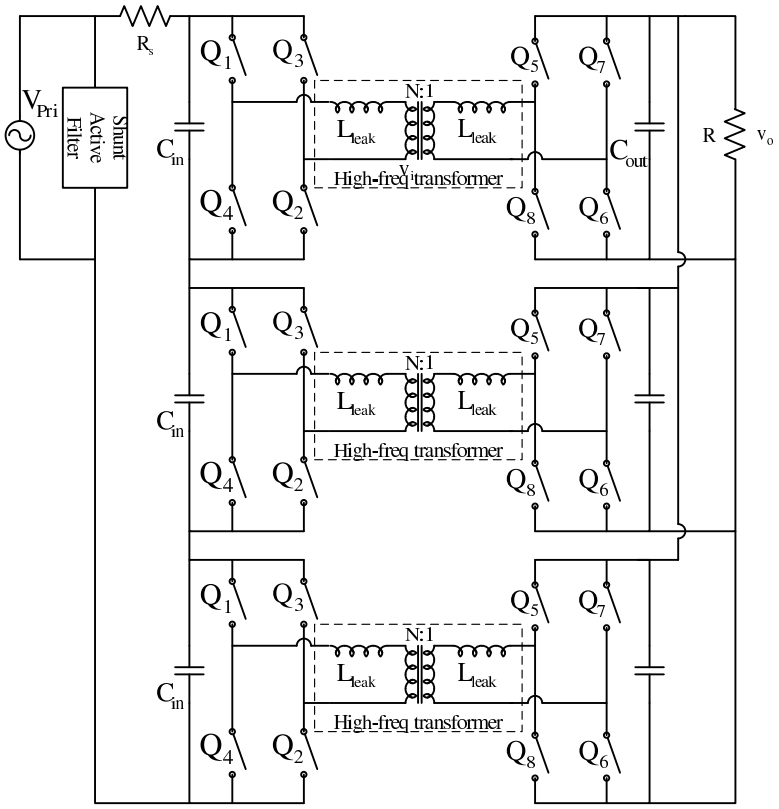

Figure 5.1. Single-phase 10 kVA 7.2 kV/120 V SST configuration

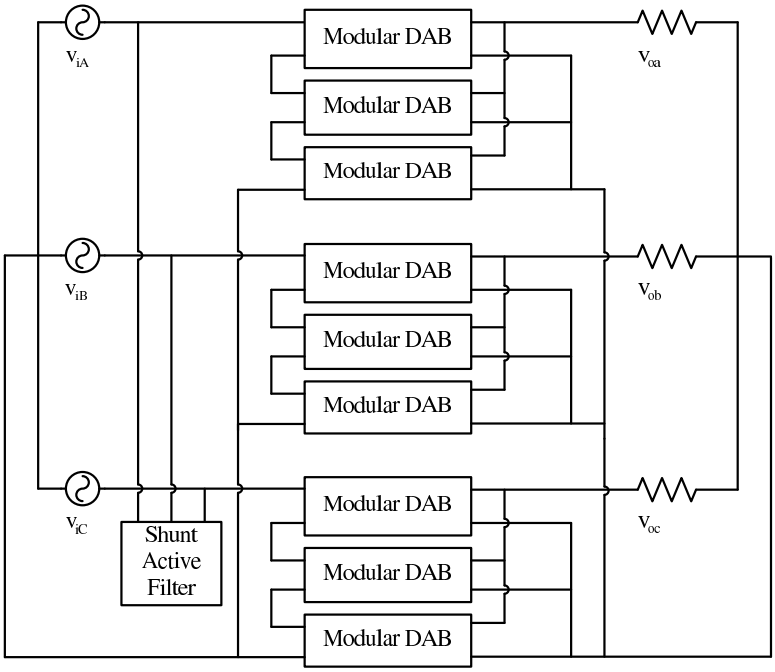

Figure 5.2. Three-phase 30 kVA 7.2 kV/120 V SST configuration

BIBLIOGRAPHY

[1] A. Huang, M. Crow, G. Heydt, J. Zheng, and S. Dale, "The Future Renewable Electric Energy Delivery and Management (FREEDM) System: The Energy Internet," *Proceedings of the IEEE*, vol. 99, pp. 133–148, Jan. 2011.

[2] E. R. Ronan, S. D. Sudhoff, S. F. Glover, and D. L. Galloway, "A power electronic-based distribution transformer," *IEEE Power Engineering Review*, vol. 22, pp. 61–61, Mar. 2002.

[3] S. Bhattacharya, T. Zhao, G. Wang, S. Dutta, S. Baek, Y. Du, B. Parkhideh, X. Zhou, and A. Q. Huang, "Design and development of Generation-I silicon based solid state transformer," in *IEEE Applied Power Electronics Conference and Exposition (APEC), 2010*, pp. 1666–1673, 2010.

[4] H. Qin and J. W. Kimball, "Ac-ac dual active bridge converter for solid state transformer," in *IEEE Energy Conversion Congress and Exposition (ECCE), 2009*, pp. 3039–3044, 2009.

[5] M. D. Manjrekar, R. Kieferndorf, and G. Venkataramanan, "Power electronic transformers for utility applications," in *IEEE Industry Applications Society (IAS) Annual Meeting, 2000*, vol. 4, pp. 2496–2502, 2000.

[6] M. Kang, P. N. Enjeti, and I. J. Pitel, "Analysis and design of electronic transformers for electric power distribution system," *IEEE Transactions on Power Electronics*, vol. 14, pp. 1133–1141, Jun. 1999.

[7] R. K. Gupta, K. K. Mohapatra, and N. Mohan, "A novel three-phase switched multi-winding power electronic transformer," in *IEEE Energy Conversion Congress and Exposition (ECCE), 2009*, pp. 2696–2703, 2009.

[8] U.S. Department of Energy, "The smart grid: An introduction." http://energy.gov/oe/downloads/smart-grid-introduction, 2010.

[9] M. Khazraei, H. Sepahvand, K. Corzine, and M. Ferdowsi, "Active capacitor voltage balancing in single-phase flying-capacitor multilevel power converters," *IEEE Transactions on Industrial Electronics*, vol. 59, pp. 769–778, Feb. 2012.

[10] R. De Doncker, D. Divan, and M. Kheraluwala, "A three-phase soft-switched high-power-density dc/dc converter for high-power applications," *IEEE Transactions on Industry Application*, vol. 27, pp. 63–73, Jan./Feb. 1991.

[11] M. N. Kheraluwala, R. W. Gascoigne, D. M. Divan, and E. D. Baumann, "Performance characterization of a high-power dual active bridge," *IEEE Transactions on Industry Application*, vol. 28, pp. 1294–1301, Jun. 1992.

[12] F. Peng, H. Li, G.-J. Su, and J. Lawler, "A new ZVS bidirectional dc-dc converter for fuel cell and battery application," *IEEE Transactions on Power Electronics*, vol. 19, pp. 54–65, Jan. 2004.

[13] D. Xu, C. Zhao, and H. Fan, "A PWM plus phase-shift control bidirectional dc-dc converter," *IEEE Transactions on Power Electronics*, vol. 19, pp. 666–675, Mar. 2004.

[14] H. Xiao and S. Xie, "A ZVS bidirectional dc-dc converter with phase-shift plus PWM control scheme," *IEEE Transactions on Power Electronics*, vol. 23, pp. 813–823, Mar. 2008.

[15] H. Bai and C. Mi, "Eliminate reactive power and increase system efficiency of isolated bidirectional dual-active-bridge dc-dc converters using novel dual-phase-shift control," *IEEE Transactions on Power Electronics*, vol. 23, pp. 2905–2914, Nov. 2008.

[16] Z. Haihua and A. M. Khambadkone, "Hybrid modulation for dual-active-bridge bidirectional converter with extended power range for ultracapacitor application," *IEEE Transactions on Industry Application*, vol. 45, pp. 1434–1442, Apr. 2009.

[17] G. Oggier, G. Garci anda, and A. Oliva, "Modulation strategy to operate the dual active bridge dc-dc converter under soft switching in the whole operating range," *IEEE Transactions on Power Electronics*, vol. 26, pp. 1228–1236, Apr. 2011.

[18] J. Kim, I. Jeong, and K. Nam, "Asymmetric duty control of the dual-active-bridge dc/dc converter for single-phase distributed generators," in *IEEE Energy Conversion Congress and Exposition (ECCE), 2009*, pp. 75–82, Sept. 2009.

[19] H. Plesko, J. Biela, and J. Kolar, "Novel modulation concepts for a drive-integrated auxiliary dc-dc converter for hybrid vehicles," in *IEEE Applied Power Electronics Conference and Exposition (APEC), 2009*, pp. 164–170, Feb. 2009.

[20] A. Jain and R. Ayyanar, "PWM control of dual active bridge: comprehensive analysis and experimental verification," in *34th Annual Conference of IEEE Industrial Electronics (IECON), 2008*, pp. 909–915, Nov. 2008.

[21] A. Jain and R. Ayyanar, "Pwm control of dual active bridge: Comprehensive analysis and experimental verification," *IEEE Transactions on Power Electronics*, vol. 26, pp. 1215–1227, Apr. 2011.

[22] J. Kim, H.-S. Song, and K. Nam, "Asymmetric duty control of a dual-half-bridge dc/dc converter for single-phase distributed generators," *IEEE Transactions on Power Electronics*, vol. 26, pp. 973–982, Mar. 2011.

[23] Y. Wang, S. W. H. de Haan, and J. A. Ferreira, "Optimal operating ranges of three modulation methods in dual active bridge converters," in *IEEE 6th International Power Electronics and Motion Control Conference (IPEMC), 2009*, pp. 1397–1401, 2009.

[24] G. G. Oggier, G. O. Garcia, and A. R. Oliva, "Switching control strategy to minimize dual active bridge converter losses," *IEEE Transactions on Power Electronics*, vol. 24, pp. 1826–1838, Jul. 2009.

[25] B. Hua, C. C. Mi, and S. Gargies, "The short-time-scale transient processes in high-voltage and high-power isolated bidirectional dc-dc converters," *IEEE Transactions on Power Electronics*, vol. 23, pp. 2648–2656, Jun. 2008.

[26] Y. Xie, J. Sun, and J. S. Freudenberg, "Power flow characterization of a bidirectional galvanically isolated high-power dc/dc converter over a wide operating range," *IEEE Transactions on Power Electronics*, vol. 25, pp. 54–66, Jan. 2010.

[27] F. Krismer and J. Kolar, "Accurate power loss model derivation of a high-current dual active bridge converter for an automotive application," *IEEE Transactions on Industrial Electronics*, vol. 57, pp. 881–891, Mar. 2010.

[28] H. Qin and J. Kimball, "A comparative efficiency study of silicon-based solid state transformers," in *IEEE Energy Conversion Congress and Exposition (ECCE), 2010*, pp. 1458–1463, Sept. 2010.

[29] F. Krismer, S. Round, and J. Kolar, "Performance optimization of a high current dual active bridge with a wide operating voltage range," in *IEEE Power Electronics Specialists Conference (PESC), 2006*, pp. 1–7, Jun. 2006.

[30] J. Biela, U. Badstubner, and J. Kolar, "Design of a 5kW, 1U, 10kW/ltr. resonant dc-dc converter for telecom applications," in *IEEE International Telecommunications Energy Conference (INTELEC), 2007*, pp. 824–831, Oct. 2007.

[31] D. Aggeler, J. Biela, and J. Kolar, "A compact, high voltage 25 kW, 50 kHz dc-dc converter based on SiC JFETs," in *IEEE Applied Power Electronics Conference and Exposition (APEC), 2008*, pp. 801–807, Feb. 2008.

[32] C. Mi, H. Bai, C. Wang, and S. Gargies, "Operation, design and control of dual H-bridge-based isolated bidirectional dc-dc converter," *IET Power Electronics*, vol. 1, pp. 507–517, Dec. 2008.

[33] Y. Wang, S. de Haan, and J. Ferreira, "High power density design of high-current dc-dc converter with high transient power," in *IEEE Energy Conversion Congress and Exposition (ECCE), 2010*, pp. 3001–3008, Sept. 2010.

[34] G. Ortiz, J. Biela, D. Bortis, and J. Kolar, "1 Megawatt, 20 kHz, isolated, bidirectional 12kV to 1.2kV dc-dc converter for renewable energy applications," in *International Power Electronics Conference (IPEC), 2010*, pp. 3212–3219, Jun. 2010.

[35] F. Krismer and J. Kolar, "Efficiency-optimized high current dual active bridge converter for automotive applications," *IEEE Transactions on Industrial Electronics*, vol. PP, p. 1, Nov 2011.

[36] R. Morrison and M. Egan, "A new power-factor-corrected single-transformer UPS design," *IEEE Transactions on Industry Application*, vol. 36, pp. 171–179, Jan./Feb. 2000.

[37] F. Krismer, J. Biela, and J. Kolar, "A comparative evaluation of isolated bi-directional dc/dc converters with wide input and output voltage range," in *IEEE Industry Applications Society (IAS) Annual Meeting, 2005*, vol. 1, pp. 599–606, Oct. 2005.

[38] H. Tao, A. Kotsopoulos, J. Duarte, and M. Hendrix, "Transformer-coupled multiport ZVS bidirectional dc-dc converter with wide input range," *IEEE Transactions on Power Electronics*, vol. 23, pp. 771–781, Mar. 2008.

[39] J. Duarte, M. Hendrix, and M. Simoes, "Three-port bidirectional converter for hybrid fuel cell systems," *IEEE Transactions on Power Electronics*, vol. 22, pp. 480–487, Mar. 2007.

[40] J. Walter and R. De Doncker, "High-power galvanically isolated dc-dc converter topology for future automobiles," in *IEEE Power Electronics Specialist Conference (PESC), 2003*, vol. 1, pp. 27–32, Jun. 2003.

[41] S. Han and D. Divan, "Bi-directional dc/dc converters for plug-in hybrid electric vehicle (PHEV) applications," in *IEEE Applied Power Electronics Conference and Exposition (APEC), 2008*, pp. 784–789, Feb. 2008.

[42] J. ming Hu, Y. rui Chen, and Z. juan Yang, "Study and simulation of one bi-directional dc/dc converter in hybrid electric vehicle," in *International Conference on Power Electronics Systems and Applications (PESA), 2009*, pp. 1–4, May 2009.

[43] Y.-J. Lee and A. Emadi, "Integrated bi-directional ac/dc and dc/dc converter for plug-in hybrid electric vehicle conversion," in *IEEE Vehicle Power and Propulsion Conference (VPPC), 2007*, pp. 215–222, Sept. 2007.

[44] D. Erb, O. Onar, and A. Khaligh, "An integrated bi-directional power electronic converter with multi-level ac-dc/dc-ac converter and non-inverted buck-boost converter for PHEVs with minimal grid level disruptions," in *IEEE Vehicle Power and Propulsion Conference (VPPC), 2010*, pp. 1–6, Sept. 2010.

[45] Y. Gurkaynak, Z. Li, and A. Khaligh, "A novel grid-tied, solar powered residential home with plug-in hybrid electric vehicle (PHEV) loads," in *IEEE Vehicle Power and Propulsion Conference (VPPC), 2009*, pp. 813–816, Sept. 2009.

[46] S. Inoue and H. Akagi, "A bidirectional isolated dc-dc converter as a core circuit of the next-generation medium-voltage power conversion system," *IEEE Transactions on Power Electronics*, vol. 22, pp. 535–542, Feb. 2007.

[47] S. Inoue and H. Akagi, "A bidirectional dc-dc converter for an energy storage system with galvanic isolation," *IEEE Transactions on Power Electronics*, vol. 22, pp. 2299–2306, Nov. 2007.

[48] S. Inoue and H. Akagi, "A bi-directional dc/dc converter for an energy storage system," in *Twenty Second Annual IEEE Applied Power Electronics Conference (APEC), 2007*, pp. 761–767, Mar. 2007.

[49] N. Tan, N. Tan, S. Inoue, S. Inoue, A. Kobayashi, and H. Akagi, "Voltage balancing of a 320-V, 12-F electric double-layer capacitor bank combined with a 10-kW bidirectional isolated dc-dc converter," *IEEE Transactions on Power Electronics*, vol. 23, pp. 2755–2765, Nov. 2008.

[50] H. Tao, A. Kotsopoulos, J. Duarte, and M. Hendrix, "Triple-half-bridge bidirectional converter controlled by phase shift and pwm," in *IEEE Applied Power Electronics Conference and Exposition (APEC), 2006*, pp. 7–13, Mar. 2006.

[51] Z. Chuanhong, S. D. Round, and J. W. Kolar, "An isolated three-port bidirectional dc-dc converter with decoupled power flow management," *IEEE Transactions on Power Electronics*, vol. 23, pp. 2443–2453, Sept. 2008.

[52] H. Krishnaswami and N. Mohan, "Three-port series-resonant dc-dc converter to interface renewable energy sources with bidirectional load and energy storage ports," *IEEE Transactions on Power Electronics*, vol. 24, pp. 2289–2297, Oct. 2009.

[53] K. Ogata, *Modern Control Engineering (5th Edition)*. Prentice Hall, 2009.

[54] S. Middlebrook, S. Cuk, "A general unified approach to modeling switching converter power stages," in *Proc. of IEEE Power Electronics Specialists Conference, 1976*, pp. 18–34, 1976.

[55] S. Middlebrook, S. Cuk, "A general unified approach to modeling switching dc-to-dc converters in discontinuous conduction mode," in *Proc. of IEEE Power Electronics Specialists Conference*, pp. 36–57, 1977.

[56] R. Middlebrook, "Small-signal modeling of pulse-width modulated switched-mode power converters," *Proceedings of the IEEE*, vol. 76, pp. 343–354, Apr 1988.

[57] D. Maksimovic, A. Stankovic, V. Thottuvelil, and G. Verghese, "Modeling and simulation of power electronic converters," *Proceedings of the IEEE*, vol. 89, pp. 898–912, Jun. 2001.

[58] R. W. Erickson and D. Maksimovic, *Fundamentals of Power Electronics (Second Edition)*. Springer, 2001.

[59] B. Lehman and R. Bass, "Switching frequency dependent averaged models for PWM dc-dc converters," *IEEE Transactions on Power Electronics*, vol. 11, pp. 89–98, Jan 1996.

[60] S. R. Sanders, Noworolski, J. M., X. Z. Liu, and G. C. Verghese, "Generalized averaging method for power conversion circuits," *IEEE Transactions on Power Electronics*, vol. 6, pp. 251–259, Feb. 1991.

[61] J. Sun and H. Grotstollen, "Symbolic analysis methods for averaged modeling of switching power converters," *IEEE Transactions on Power Electronics*, vol. 12, pp. 537–546, May 1997.

[62] V. A. Caliskan, O. C. Verghese, and A. M. Stankovic, "Multifrequency averaging of dc/dc converters," *IEEE Transactions on Power Electronics*, vol. 14, pp. 124–133, Jan. 1999.

[63] Z. Mihajlovic, B. Lehman, and C. Sun, "Output ripple analysis of switching dc-dc converters," *IEEE Transactions on Circuits and Systems I: Regular Papers*, vol. 51, pp. 1596–1611, Aug. 2004.

[64] C.-C. Hou and P.-T. Cheng, "Experimental verification of the active front-end converters dynamic model and control designs," *IEEE Transactions on Power Electronics*, vol. 26, pp. 1112–1118, Apr. 2011.

[65] P. Krein, J. Bentsman, R. Bass, and B. Lesieutre, "On the use of averaging for the analysis of power electronic systems," *IEEE Transactions on Power Electronics*, vol. 5, pp. 182–190, Feb. 1990.

[66] P. Krein and R. Bass, "A new approach to fast simulation of periodically switching power converters," in *IEEE Industry Applications Society (IAS) Annual Meeting, 1990*, pp. 1185–1189, Oct 1990.

[67] D. Shortt and F. Lee, "Improved switching converter model using discrete and averaging techniques," *IEEE Transactions on Aerospace and Electronic Systems*, vol. 19, pp. 190–202, Mar. 1983.

[68] D. Shortt and F. Lee, "Extensions of the discrete-average models for converter power stages," *IEEE Transactions on Aerospace and Electronic Systems*, vol. 20, pp. 279–289, May 1984.

[69] G. C. Verghese, M. E. Elbuluk, and J. G. Kassakian, "A general approach to sampled-data modeling for power electronic circuits," *IEEE Transactions on Power Electronics*, vol. 1, pp. 76–89, Apr. 1986.

[70] M. Elbuluk, G. Verghese, and J. Kassakian, "Sampled-data modeling and digital control of resonant converters," *IEEE Transactions on Power Electronics*, vol. 3, pp. 344–354, Jul. 1988.

[71] S. Zheng and D. Czarkowski, "Modeling and digital control of a phase-controlled series-parallel resonant converter," *IEEE Transactions on Industrial Electronics*, vol. 54, pp. 707–715, Apr. 2007.

[72] H. K. Krishnamurthy and R. Ayyanar, "Building block converter module for universal (ac-dc, dc-ac, dc-dc) fully modular power conversion architecture," in *IEEE Power Electronics Specialists Conference (PECS), 2007*, pp. 483–489, 2007.

[73] B. Hua, C. C. Mi, and S. Gargies, "The short-time-scale transient processes in high-voltage and high-power isolated bidirectional dc-dc converters," *IEEE Transactions on Power Electronics*, vol. 23, pp. 2648–2656, Jun. 2008.

[74] H. Bai, Z. Nie, and C. C. Mi, "Experimental comparison of traditional phase-shift, dual-phase-shift, and model-based control of isolated bidirectional dc-dc converters," *IEEE Transactions on Power Electronics*, vol. 25, pp. 1444–1449, Jun. 2010.

[75] F. Krismer and J. W. Kolar, "Accurate small-signal model for the digital control of an automotive bidirectional dual active bridge," *IEEE Transactions on Power Electronics*, vol. 24, pp. 2756–2768, Dec. 2009.

[76] C. Zhao, S. D. Round, and J. W. Kolar, "Full-order averaging modelling of zero-voltage-switching phase-shift bidirectional dc-dc converters," *IET Power Electronics*, vol. 3, pp. 400–410, Mar. 2010.

[77] P. Kokotovic, H. K. Khalil, and J. O'Reilly, *Singular Perturbation Methods in Control Analysis and Design*. London, U.K.: Academic, 1999.

[78] J. W. Kimball, J. T. Mossoba, and P. T. Krein, "A stabilizing, high-performance controller for input series-output parallel converters," *IEEE Transactions on Power Electronics*, vol. 23, pp. 1416–1427, Mar. 2008.

[79] D. Holmes, T. Lipo, B. McGrath, and W. Kong, "Optimized design of stationary frame three phase ac current regulators," *IEEE Transactions on Power Electronics*, vol. 24, pp. 2417–2426, Nov. 2009.

[80] J. Hwang, P. Lehn, and M. Winkelnkemper, "A generalized class of stationary frame-current controllers for grid-connected ac-dc converters," *IEEE Transactions on Power Delivery*, vol. 25, pp. 2742–2751, Oct. 2010.

[81] D. Dong, T. Thacker, R. Burgos, D. Boroyevich, and F. Wang, "On zero steady-state error voltage control of single-phase pwm inverters with different load-types," *IEEE Transactions on Power Electronics*, vol. PP, no. 99, p. 1, 2011.

[82] W. Zhao, D. D.-C. Lu, and V. G. Agelidis, "Current control of grid-connected boost inverter with zero steady-state error," *IEEE Transactions on Power Electronics*, vol. 26, pp. 2825–2834, Oct. 2011.

[83] V.-T. Phan and H.-H. Lee, "Control strategy for harmonic elimination in stand-alone DFIG applications with nonlinear loads," *IEEE Transactions on Power Electronics*, vol. 26, pp. 2662–2675, Sept. 2011.

[84] P. Loh, Y. Tang, F. Blaabjerg, and P. Wang, "Mixed-frame and stationary-frame repetitive control schemes for compensating typical load and grid harmonics," *IET Power Electronics*, vol. 4, pp. 218–226, Feb. 2011.

[85] H. Nian and R. Zeng, "Improved control strategy for stand-alone distributed generation system under unbalanced and non-linear loads," *IET Renewable Power Generation*, vol. 5, pp. 323–331, Sept. 2011.

[86] J. Hu and Y. He, "Modeling and control of grid-connected voltage-sourced converters under generalized unbalanced operation conditions," *IEEE Transactions on Energy Conversion*, vol. 23, pp. 903–913, Sept. 2008.

[87] S. Yang, Q. Lei, F. Peng, and Z. Qian, "A robust control scheme for grid-connected voltage-source inverters," *IEEE Transactions on Industrial Electronics*, vol. 58, pp. 202–212, Jan. 2011.

[88] A. Hasanzadeh, O. Onar, H. Mokhtari, and A. Khaligh, "A proportional-resonant controller-based wireless control strategy with a reduced number of sensors for parallel-operated UPSs," *IEEE Transactions on Power Delivery*, vol. 25, pp. 468–478, Jan. 2010.

[89] A. Timbus, M. Liserre, R. Teodorescu, P. Rodriguez, and F. Blaabjerg, "Evaluation of current controllers for distributed power generation systems," *IEEE Transactions on Power Electronics*, vol. 24, pp. 654–664, Mar. 2009.

[90] Y. W. Li, F. Blaabjerg, D. Vilathgamuwa, and P. C. Loh, "Design and comparison of high performance stationary-frame controllers for DVR implementation," *IEEE Transactions on Power Electronics*, vol. 22, pp. 602–612, Mar. 2007.

[91] A. Yepes, F. Freijedo, O. Lopez, and J. Doval-Gandoy, "Analysis and design of resonant current controllers for voltage-source converters by means of nyquist diagrams and sensitivity function," *IEEE Transactions on Industrial Electronics*, vol. 58, pp. 5231–5250, Nov. 2011.

[92] A. Roslan, K. Ahmed, S. Finney, and B. Williams, "Improved instantaneous average current-sharing control scheme for parallel-connected inverter considering line impedance impact in microgrid networks," *IEEE Transactions on Power Electronics*, vol. 26, pp. 702–716, Mar. 2011.

[93] P. Mattavelli, "Synchronous-frame harmonic control for high-performance ac power supplies," *IEEE Transactions on Industry Application*, vol. 37, pp. 864–872, May/Jun 2001.

[94] M. Newman and D. Holmes, "Delta operator digital filters for high performance inverter applications," *IEEE Transactions on Power Electronics*, vol. 18, pp. 447–454, Jan. 2003.

[95] J. Reeve and M. Sultan, "Robust adaptive control of HVDC systems," *IEEE Transactions on Power Delivery*, vol. 9, pp. 1487–1493, Jul. 1994.

[96] M. AI-Numay and D. Taylor, "A piecewise linear method for digital control of PWM systems," in *IEEE Power Electronics Specialists Conference (PESC), 1996*, vol. 1, pp. 803–809, Jun 1996.

[97] A. Prodic and D. Maksimovic, "Design of a digital PID regulator based on look-up tables for control of high-frequency dc-dc converters," in *IEEE Workshop on Computers in Power Electronics, 2002.*, pp. 18–22, Jun. 2002.

[98] A. Forsyth, I. Ellis, and M. Moller, "Adaptive control of a high-frequency dc-dc converter by parameter scheduling," *IEE Proceedings - Electric Power Applications,*, vol. 146, pp. 447–454, Jul. 1999.

[99] K. J. Astrom and B. Wittenmark, *Adaptive Control: Second Edition*. Dover Publications, 2008.

[100] M. Hernandez-Gomez, R. Ortega, F. Lamnabhi-Lagarrigue, and G. Escobar, "Adaptive PI stabilization of switched power converters," *IEEE Transactions on Control Systems Technology*, vol. 18, pp. 688–698, May 2010.

[101] L. Yacoubi, K. Al-Haddad, L.-A. Dessaint, and F. Fnaiech, "Linear and nonlinear control techniques for a three-phase three-level NPC boost rectifier," *IEEE Transactions on Industrial Electronics*, vol. 53, pp. 1908–1918, Dec. 2006.

[102] S. Vazquez, J. Sanchez, J. Carrasco, J. Leon, and E. Galvan, "A model-based direct power control for three-phase power converters," *IEEE Transactions on Industrial Electronics*, vol. 55, pp. 1647–1657, Apr. 2008.

[103] Z. Jiang, L. Gao, and R. Dougal, "Adaptive control strategy for active power sharing in hybrid fuel cell/battery power sources," *IEEE Transactions on Energy Conversion*, vol. 22, pp. 507–515, Jun. 2007.

[104] S. Sanders and G. Verghese, "Lyapunov-based control for switched power converters," *IEEE Transactions on Power Electronics*, vol. 7, pp. 17–24, Jan. 1992.

[105] R. Ortega, A. Loria, P. Nicklasson, and H. Sira-Ramirez, *Passivity-Based Control of Euler-Lagrange Systems*. Springer, 1998.

[106] S. Banerjee and G. Verghese, *Nonlinear Phenomena in Power Electronics: Bifurcations, Chaos, Control, and Applications*. Wiley-IEEE Press, 2001.

[107] D. Jeltsema and J. Scherpen, "A power-based perspective in modeling and control of switched power converters [past and present]," *IEEE Industrial Electronics Magazine*, vol. 1, pp. 7–54, May 2007.

[108] H. Zhou, A. Khambadkone, and X. Kong, "Passivity-based control for an interleaved current-fed full-bridge converter with a wide operating range using the brayton-moser form," *IEEE Transactions on Power Electronics*, vol. 24, pp. 2047–2056, Sept. 2009.

[109] L. Harnefors, M. Bongiorno, and S. Lundberg, "Input-admittance calculation and shaping for controlled voltage-source converters," *IEEE Transactions on Industrial Electronics*, vol. 54, pp. 3323–3334, Dec. 2007.

[110] L. Harnefors, L. Zhang, and M. Bongiorno, "Frequency-domain passivity-based current controller design," *IET Power Electronics*, vol. 1, pp. 455–465, Dec. 2008.

[111] K. Young, V. Utkin, and U. Ozguner, "A control engineer's guide to sliding mode control," *IEEE Transactions on Control Systems Technology*, vol. 7, pp. 328–342, May 1999.

[112] S.-C. Tan, Y. Lai, C. Tse, and L. Martinez-Salamero, "Special family of PWM-based sliding-mode voltage controllers for basic dc-dc converters in discontinuous conduction mode," *IET Electric Power Applications*, vol. 1, pp. 64–74, Jan. 2007.

[113] S.-C. Tan, Y. Lai, C. Tse, and M. Cheung, "Adaptive feedforward and feedback control schemes for sliding mode controlled power converters," *IEEE Transactions on Power Electronics*, vol. 21, pp. 182–192, Jan. 2006.

[114] S. Pinto and J. Silva, "Sliding mode direct control of matrix converters," *IET Electric Power Applications*, vol. 1, pp. 439–448, May 2007.

[115] A. Susperregui, G. Tapia, I. Zubia, and J. Ostolaza, "Sliding-mode control of doubly-fed generator for optimum power curve tracking," *Electronics Letters*, vol. 46, pp. 126–127, Nov. 2010.

[116] Z. Chen, W. Gao, J. Hu, and X. Ye, "Closed-loop analysis and cascade control of a nonminimum phase boost converter," *IEEE Transactions on Power Electronics*, vol. 26, pp. 1237–1252, Apr. 2011.

[117] C.-F. Hsu, I.-F. Chung, C.-M. Lin, and C.-Y. Hsu, "Self-regulating fuzzy control for forward dc-dc converters using an 8-bit microcontroller," *IET Power Electronics*, vol. 2, pp. 1–12, Jan. 2009.

[118] M. Zandi, A. Payman, J.-P. Martin, S. Pierfederici, B. Davat, and F. Meibody-Tabar, "Energy management of a fuel cell/supercapacitor/battery power source for electric vehicular applications," *IEEE Transactions on Vehicular Technology*, vol. 60, pp. 433–443, Feb. 2011.

[119] C. Cecati, F. Ciancetta, and P. Siano, "A multilevel inverter for photovoltaic systems with fuzzy logic control," *IEEE Transactions on Industrial Electronics*, vol. 57, pp. 4115–4125, Dec. 2010.

[120] A. Bouafia, F. Krim, and J.-P. Gaubert, "Fuzzy-logic-based switching state selection for direct power control of three-phase PWM rectifier," *IEEE Transactions on Industrial Electronics*, vol. 56, pp. 1984–1992, Jun. 2009.

[121] B. Choi, B. Cho, and S.-S. Hong, "Dynamics and control of dc-to-dc converters driving other converters downstream," *IEEE Transactions on Circuits and Systems I: Fundamental Theory and Applications*, vol. 46, pp. 1240–1248, Oct 1999.

[122] P. Liutanakul, A.-B. Awan, S. Pierfederici, B. Nahid-Mobarakeh, and F. Meibody-Tabar, "Linear stabilization of a dc bus supplying a constant power load: A general design approach," *IEEE Transactions on Power Electronics*, vol. 25, pp. 475–488, Feb. 2010.

[123] A. Emadi, A. Khaligh, C. Rivetta, and G. Williamson, "Constant power loads and negative impedance instability in automotive systems: definition, modeling, stability, and control of power electronic converters and motor drives," *IEEE Transactions on Vehicular Technology*, vol. 55, pp. 1112–1125, Jul. 2006.

[124] A. Rahimi and A. Emadi, "An analytical investigation of dc/dc power electronic converters with constant power loads in vehicular power systems," *IEEE Transactions on Vehicular Technology*, vol. 58, pp. 2689–2702, Jul. 2009.

[125] A. Rahimi and A. Emadi, "Active damping in dc/dc power electronic converters: A novel method to overcome the problems of constant power loads," *IEEE Transactions on Industrial Electronics*, vol. 56, pp. 1428–1439, May 2009.

[126] D. Cardozo, J. Balda, D. Trowler, and H. Mantooth, "Novel nonlinear control of dual active bridge using simplified converter model," in *IEEE Twenty-Fifth Annual Applied Power Electronics Conference and Exposition (APEC), 2010*, pp. 321–327, Feb. 2010.

[127] A. Alonso, J. Sebastian, D. Lamar, M. Hernando, and A. Vazquez, "An overall study of a dual active bridge for bidirectional dc/dc conversion," in *IEEE Energy Conversion Congress and Exposition (ECCE), 2010*, pp. 1129–1135, Sept. 2010.

[128] D. Segaran, B. McGrath, and D. Holmes, "Adaptive dynamic control of a bidirectional dc-dc converter," in *IEEE Energy Conversion Congress and Exposition (ECCE), 2010*, pp. 1442–1449, Sept. 2010.

[129] G. Demetriades and H.-P. Nee, "Dynamic modeling of the dual-active bridge topology for high-power applications," in *IEEE Power Electronics Specialists Conference (PESC), 2008*, pp. 457–464, Jun. 2008.

[130] H. Krishnamurthy and R. Ayyanar, "Stability analysis of cascaded converters for bidirectional power flow applications," in *IEEE International Telecommunications Energy Conference (INTELEC), 2008*, pp. 1–8, Sept. 2008.

[131] J. Shi, W. Gou, H. Yuan, T. Zhao, and A. Huang, "Research on voltage and power balance control for cascaded modular solid-state transformer," *IEEE Transactions on Power Electronics*, vol. 26, pp. 1154–1166, Apr. 2011.

[132] H. Akagi and R. Kitada, "Control and design of a modular multilevel cascade btb system using bidirectional isolated dc/dc converters," *IEEE Transactions on Power Electronics*, vol. 26, pp. 2457–2464, Sept. 2011.

[133] K. Berringer, J. Marvin, and P. Perruchoud, "Semiconductor power losses in ac inverters," in *IEEE Industry Applications Society (IAS) Annual Meeting, 1995*, vol. 1, pp. 882–888, 1995.

[134] J. A. Ferreira, "Improved analytical modeling of conductive losses in magnetic components," *IEEE Transactions on Power Electronics*, vol. 9, pp. 127–131, Jan. 1994.

[135] C. W. T. McLyman, *Transformer and Inductor Design Handbook*. CRC, 2004.

[136] C. Gaviria, E. Fossas, and R. Grino, "Robust controller for a full-bridge rectifier using the IDA approach and GSSA modeling," *IEEE Transactions on Circuits and Systems I: Regular Papers*, vol. 52, pp. 609–616, Mar. 2005.

[137] Z. Ye, P. Jain, and P. Sen, "Phasor-domain modeling of resonant inverters for high-frequency ac power distribution systems," *IEEE Transactions on Power Electronics*, vol. 24, pp. 911–923, Apr. 2009.

[138] C.-T. Chen, *Linear System Theory and Design*. Oxford University Press, 1998.

[139] T. Zhao, G. Wang, J. Zeng, D. S., B. S., and A. Q. Huang, "Voltage and power balance control for a cascaded multilevel solid state transformer," in *IEEE Applied Power Electronics Conference and Exposition (APEC), 2010*, pp. 761–767, 2010.

[140] W. Kersting, "Radial distribution test feeders," *IEEE Transactions on Power Systems*, vol. 6, pp. 975–985, Aug. 1991.

VITA

Hengsi Qin was born in Nanning, Guangxi, China. He received the B.S. and M.S. degrees in electrical engineering from Central South University, Changsha, Hunan, China, in 2005 and 2008, respectively. In May 2012, he received his Ph.D. degree in Electrical Engineering from the Department of Electrical and Computer Engineering, Missouri University of Science and Technology (Missouri S&T), Rolla, MO, USA. After completion of his Ph.D., he will be a senior engineer at Solarbridge Technologies, Austin, TX.